Master Thesis

Novel Concept of TWIP-Assisted Steel

Kang, Jee Hyun (姜知賢)

Computational Metallurgy

Graduate Institute of Ferrous Technology

Pohang University of Science and Technology

2010

C-Mn계 다상조직 TWIP-Assisted 강

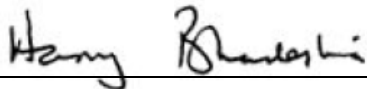# Novel Concept of TWIP-Assisted Steel

Novel Concept of TWIP-Assisted Steel

by

Kang, Jee Hyun

Computational Metallurgy

Graduate Institute of Ferrous Technology

Pohang University of Science and Technology

A thesis submitted to the faculty of Pohang University of Science and Technology in partial fulfillments of the requirements for the degree of Master of Science in the Graduate Institute of Ferrous Technology (Computational Metallurgy)

Pohang, Korea

December 21, 2009

Approved by

Professor Bhadeshia, H.K.D.H.

Novel Concept of TWIP-Assisted Steel

Kang, Jee Hyun

This dissertation is submitted for the degree of Master of Science at Graduated Institute of Ferrous Technology of Pohang University of Science and Technology. The research reported herein was approved by the committee of Thesis Appraisal.
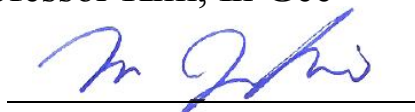
December 21, 2009

Thesis Review Committee

Chairman: Professor Lee, Hae Geon

Member: Professor Suh, Dong Woo

Member: Professor Kim, In Gee

Abstract

TWIP steels are known for their high strength with elongation but have manufacturing and cost disadvantages due to their high manganese content. The novel concept of TWIP-assisted steels has been introduced in analogy with TRIP-assisted steels. The aim was to produce local regions of austenite which contains manganese high enough to exhibit localized TWIP during the deformation.

To achieve the aim, the cementite particles in ferrite matrix were formed by tempering in the ferrite+cementite field. The cementite would enrich with Mn after appropriate time. Then, this enriched cementite was supposed to transform into austenite by isothermal heat treatment. The austenite would inherit the high manganese content and be retained on cooling. The final microstructure would contain Mn-rich austenite islands in ferrite matrix.

Three alloys were designed using thermodynamic calculation considering the volume fraction and Mn content of cementite. The appropriate time to enrich cementite was decided using thermodynamic calculation with a finite difference kinetic model.

A series of heat treatment and microstructural and microanalytical characterization were done. The most important result was that austenite which formed at ferrite/cementite interface grew by consuming both ferrite

and cementite simultaneously. Even though cementite bears high manganese, growth into ferrite resulted in dilution of Mn.

The tensile testing was attempted but the samples were so large that they showed low heating rate. They resulted in different microstructure from the ones produced by dilatometry, thus, exhibiting disappointing tensile properties.

Contents

Nomenclature

A The number of formula units per unit cell

D_{Mn} Diffusivity of Mn in ferrite

F_{kj} Structure factor

f^j Mol-fraction of the phase j which has been incorporated in austenite

i Index of data points

j Index of phases

K Partitioning coefficient

k Index of overlapping neighbouring Bragg reflections

L_{kj} Lorentz polarization factor

M Mass of the formula unit

M_{kj} Multiplicity

N Total number of pattern points being in account of refinement

n	Strain-hardening coefficient
P_{kj}	Preferred orientation function
p	The number of refined parameter
$R_{\exp}$	Expected weighted profile factor
R_{wp}	Weighted profile factor
$\bar{r}$	Mean particle radius of cementite at time t
$\bar{r}_0$	Mean particle radius of cementite at time t_0 when steady-state growth begins
S_j	Scaling factor per phase
T_{oj}	Overall temperature factor
V	Unit cell volume
V_m^{cem}	Molar volume of cementite
W_p	Weight fraction of phase

w_i	Weighting parameter
x_c^j	Mol-fraction of C in phase j
x_{Mn}^j	Mol-fraction of Mn in phase j
Y_{Mn}^j	Site fraction of Mn in phase j
y_{bi}	Background intensity at data point i
y_{ci}	Calculated intensity at data point i
y_i	Observed intensity at data point i
Z	Atomic number
α	Ferrite
α'	Martensite
γ	Austenite
θ	Cementite
σ	Ferrite/cementite interface energy

ϕ_{ikj} Profile function

χ_v Reduced chi

EDS   Energy Dispersive Spectroscopy

EELS   Electron Energy Loss Spectroscopy

Ms   Martensite-start temperature

MTDATA   Metallurgical and Thermochemical DATAbase

OM   Optical Microscopy

SEM   Scanning Electron Microscopy

TEM   Transmission Electron Microscopy

TRIP   TRansformation Induced Plasticity

TWIP   TWinning Induced Plasticity

UTS   Ultimate Tensile Strength

XRD   X-Ray Diffraction

I. Introduction

I.1. TWIP Steel

I.1.1. Strength and Limitations

A goal of research on metals has been to obtain high strength and ductility. It agrees with a recent trend pursuing lightness in order to reduce the fuel consumption, especially for automobile applications. TRansformation Induced Plasticity (TRIP), TWinning Induced Plasticity (TWIP) and complex phase steels have been developed to fulfill this need (Imlau and Heller, 2007). Among these three, TWIP steel has many attractive properties but has not found major applications.

TWIP steel is fully austenitic at room temperature, because it has approximately 20-30 wt% of manganese. The austenite remains stable during deformation and some of the plastic deformation occurs by twinning, which is said to enhance elongation. Continually forming twin boundaries can impede the dislocation movements so that the strength is improved (Raghavan *et al.*, 1969). In comparison with TRIP where martensitic transformation is induced during deformation producing higher hardening rate, the TWIP effect can result in a balance between good strength and strain with a moderate hardening rate (Fig. I.1). Therefore, its formability and specific energy

absorption are good for automotive applications (Fig. I.2). Besides, fatigue behavior is better than in some austenitic stainless steels or comparable with dual phase steel (Hamada *et al.*, 2009, Sperle, 1985). Fig. I.3 shows that high Mn steels is superior to austenitic stainless steels in fatigue performance. Table I.1 shows fatigue strength of high Mn steels in comparison with dual phase steel. All of these promising characteristics are ripe for exploitation.

100
90
80
Total Elongation / %
70
60
50
40
30
20
10
0

0   200   400   600   800   1000   1200
Ultimate Tensile Stress / MPa

33Mn 3Al3Si■ ■16Mn 2Al0.3C■ ■22Mn 0.6C
25Mn 3Al3Si■
25Mn 4Al 2Si■ ■30Mn 3Al3Si   18Mn 0.6C■
30Mn 4Al 2Si■
30Mn 2Al 4Si■
20Mn 4Al0.05C■ 25Mn 2Al 4Si■   22Mn 0.6C■
36Mn■
25Mn 1Al0.3C■

■ TWIP
▲ TWIP/TRIP
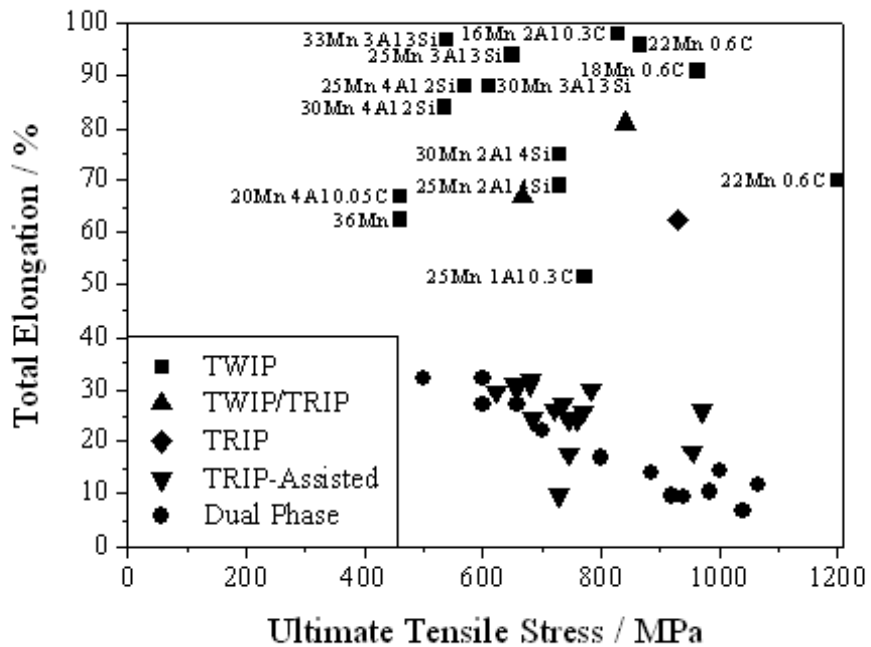◆ TRIP
▼ TRIP-Assisted
● Dual Phase

Fig. I.1   Ultimate Tensile Stress (UTS) and total elongation of Advanced High Strength Steel (AHSS). The TWIP steels occupy high UTS and high elongation region. Only major compositions of TWIP steels are indicated. The numbers in the labels are wt% of certain alloying elements and are rounded off to one significant digit (Kim and Kim, 1993, Sato *et al.*, 1989, Frommeyer *et al.*, 2003, Grassel *et al.*, 2000, Allain *et al.*, 2004, Ding *et al.*, 2006, Xu *et al.*, 2008, Movahed *et al.*, 2009, WorldAutoSteel, Srivastava *et al.*, 2006, Oliver *et al.*, 2007, Jiang *et al.*, 2008).
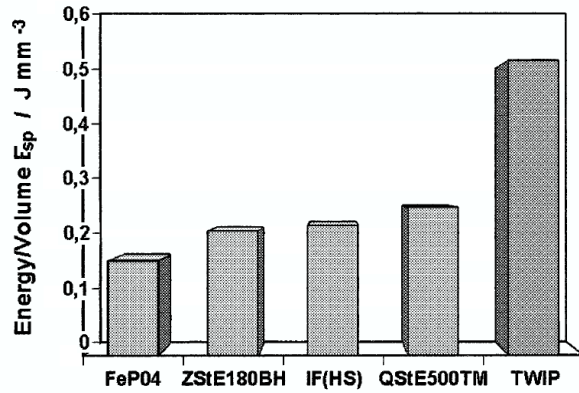
Fig. I.2　Specific energy absorption E_{spec} values of conventional deep drawing steels in comparison with the Fe-25Mn-3Al-3Si wt% TWIP steel; test temperature: 20℃, strain rate: $10^2 \, s^{-1}$ (Frommeyer *et al.*, 2003).
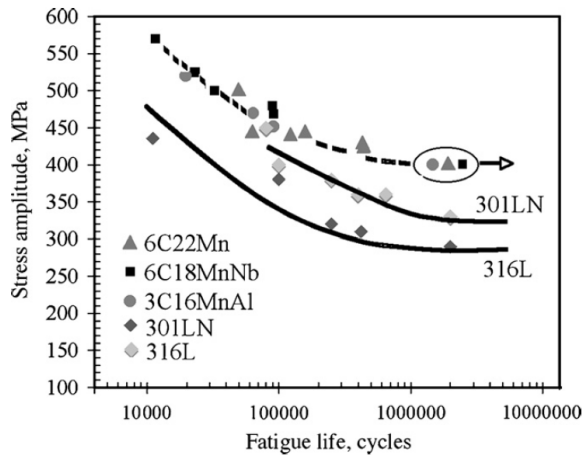

Fig. I.3　Stress amplitude-fatigue life data for the investigated steels. Data for annealed 301LN and 316L austenitic stainless steels are included for comparison (Hamada *et al.*, 2009). The compositions of the steels are shown Table I.2

Steel	UTS / MPa	Fatigue Strength at 2×10^6 cycles / MPa
6C 22Mn	866	400
6C 18Mn Nb	963	400
3C 16Mn Al	830	400
301 LN	650-850	350
316 L	530-680	300
Mild steel	292	240
DOCOL 400 BH	382/418/410/431	316/360/365/377
DOCOL 600 DL	620/635	307/393

Table I.1   Fatigue strength of various steels. UTS have been given for comparison (Hamada *et al.*, 2009, Sperle, 1985). DOCOL 400 BH and DOCOL 600 DL are dual phase steels. Strength values divided by slashes indicate different conditions. Steel composition is provided in Table I.2.

Steel	C / wt%	Mn / wt%	Si / wt%	etc. / wt%
6C 22Mn	0.60	22.3	-	-
6C 18Mn Nb	0.60	17.8	-	Nb:0.02
3C 16Mn Al	0.29	16.4	-	Al:1.54
301 LN	≤0.03	≤1.00	≤2.00	Cr:16.50-18.50, Ni:6.00-8.00, N: 0.10-0.20
316 L	≤0.03	≤1.00	≤2.00	Cr:16.50-18.50, Ni:10.00-13.00, N≤0.11, Mo:2.00-2.50
Mild steel	0.03	0.15	≤0.004	
DOCOL 400 BH	0.03	0.21	0.02	
DOCOL 600 DL	0.08	1.74	0.51	

Table I.2 The compositions of the steels investigated for fatigue strength (Sperle, 1985, Hamada *et al.*, 2009, WorldAutoSteel).

On the other hand, there are some difficulties with the TWIP concept. The alloys have poor machinability and delayed fracture is reported. Although delayed fracture can be avoided by adding Al, the prevention mechanism has not been revealed (Kim *et al.*, 2008). Besides, since the Mn vapour pressure is high during steel making, some percentage of Mn is lost to the melt which results in a low Mn yield in the final state (Kliber *et al.*, 2009). Moreover, continuous casting is impossible for high-Mn steels since grain boundary oxidation occurs and forms microscabs which may cause surface cracks

during hot rolling (Park *et al.*, 1998). Although strip casting has been introduced to resolve this problem (Liu *et al.*, 2007, Engl *et al.*, 2007, Spitzer *et al.*, 2003), there are dent defects forming during the process (Fig. I.4). TWIP steel is more expensive than others because of the rich alloying and manufacturing difficulties. After all, these difficulties have prevented TWIP steel from widely exploited.
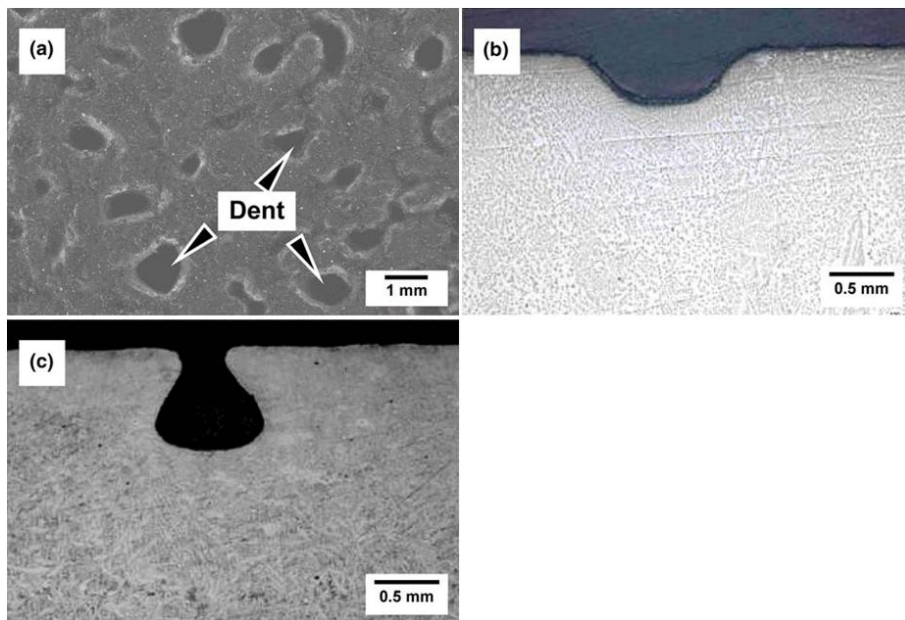

Fig. I.4   Optical micrographs of the TWIP-steel cast strip produced by a twin roll strip caster, showing (a) dent defects of the surface and (b, c) cross-sectional shapes of dent defects (Ha *et al.*, 2008).

I.1.2. Alloying Elements

The compositions of the TWIP steels introduced in Fig. I.1 are shown in Table I.3.

Steel	Mn / wt%	C / wt%	Al / wt%	Si / wt%	etc. / wt%
20Mn 4Al 0.05C	19.40	0.053	4.40	0.030	
36Mn	35.4	0.004	-	0.02	
25Mn 2Al 4Si	25.5	0.03	1.8	3.9	
25Mn 3Al 3Si	26.5	0.03	2.8	3.0	
25Mn 4Al 2Si	25.6	0.03	3.8	2.0	
30Mn 2Al 4Si	28.7	0.02	2.0	4.0	
30Mn 3Al 3Si	29.2	0.02	2.8	3.0	
30Mn 4Al 2Si	30.6	0.01	3.9	2.0	
22Mn 0.6C	22.3	0.60	-	-	
18Mn 0.6C	17.8	0.60	-	-	Nb:0.02
16Mn 2Al 0.3C	16.4	0.29	1.54		
33Mn 3Al 3Si	33.0	0.0006	2.93	3.0	

Table I.3 The composition of TWIP steels in Fig. I.1 (Grassel *et al.*, 2000, Sato *et al.*, 1989, Tomota *et al.*, 1986, Hamada *et al.*, 2009).

The typical alloying elements of TWIP steel are Mn, C, Al, Si. In order to keep austenite stable, two of the efficient austenite stabilizers (Fig. I.5), Mn and C are included. There are three mechanisms during austenite plastic deformation; dislocation movement (slip), martensitic transformation and twinning. The selection of mechanism is thought to be decided by stacking

fault energy (Fig. I.6), yet the value of the borderline is different in the published papers. Stacking fault energy depends on temperature as well as alloying elements. To obtain the stacking fault energy in the right region for twinning, Al and Si are included. Al increases stacking fault energy, so it inhibits ε martensite transformation and promotes twinning during deformation. Si decreases stacking fault energy, so it is included when stacking fault energy is too high to show a TWIP effect. Besides, Al is added in order to prevent delayed fracture as mentioned before.
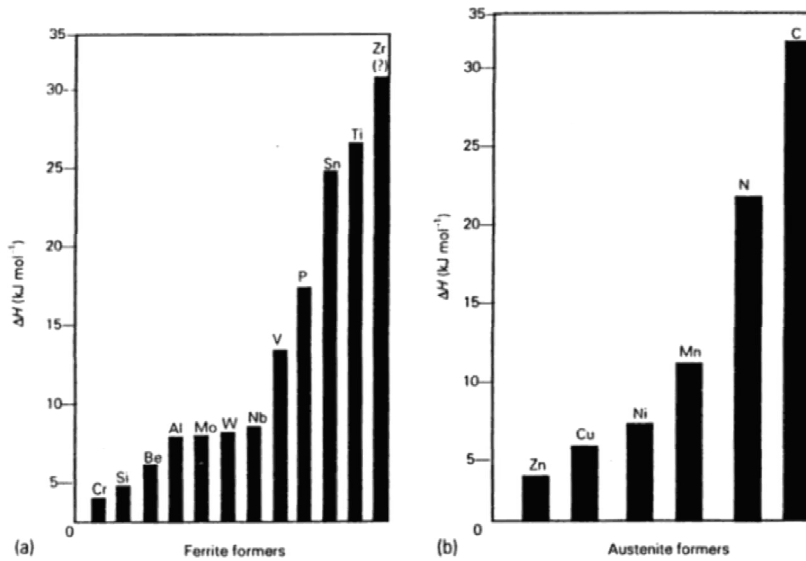

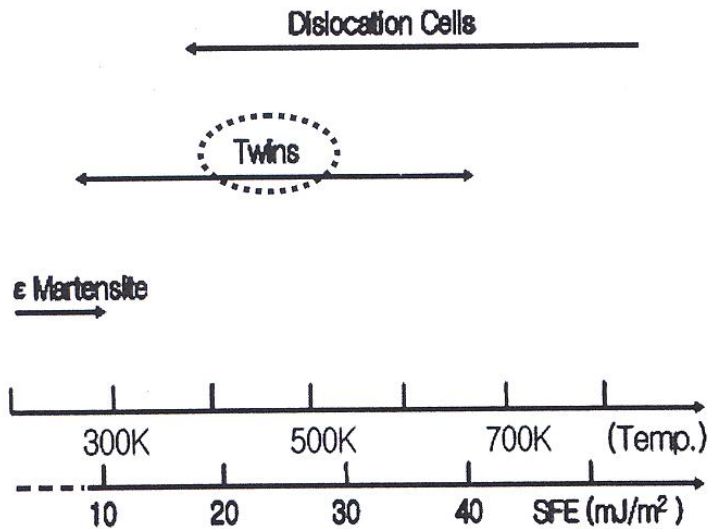Fig. I.5   Relative strength of alloying elements as: (a) ferrite formers; (b) austenite formers (Andrews, 1956)

9

Fig. I.6 Effects of temperature and stacking fault energy (SFE) on the deformation mechanism in TWIP steels (Kim *et al.*, 2008).

I.2. Austenite Stabilization

The stability of austenite is considered to be the one of the most important issues of multi-phase steels because retained austenite is believed to enhance the strain hardening behavior and this is important to prevent plastic instabilities. Among the several determining factors, the most important is to include solutes which act as austenite stabilizers (Haidemenopoulos, 1996).

An ingenious way of stabilizing austenite by heat treatment has been developed, consisting of three steps with Fe-1.5 Mn-0.38 Si-0.16 C wt% alloy (Fig. I.7). The first involves austenitization and quenching in order to obtain a

fully martensitic structure. The second tempers the martensite in a mixture of ferrite (α) and cementite (θ). This will introduce small dispersed cementite particles in the ferrite matrix. The last step is to anneal the alloy in the (α + austenite (γ)) field. During the process, the formation of austenite occurs by consuming all of the cementite particles. Finally, the structure is called ferrite-austenite dual phase instead of ferrite-martensite dual phase because the austenite is stabilized and avoids martensitic transformation during cooling. It is surprising that the austenite can be stabilized even though the overall Mn content is only 1.5 wt%. This is possible only because the Mn content of the cementite is inherited by the austenite formed during the third anneal. In addition, the tensile properties are better than conventional ferrite-martensite dual phase steel (Fig. I.8). Comparing with the tensile properties of conventional TRIP/TWIP steels given in Fig. I.1 the strength is lower than that of TRIP steel and uniform elongation is lower than that of TWIP steel. However, it is still remarkable considering the low content of Mn. The austenite presumably enhances properties via the TRIP effect.
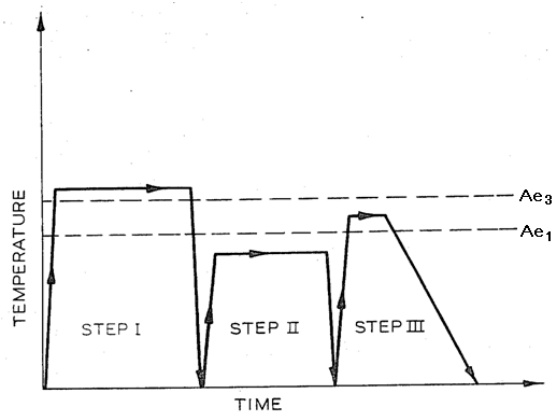
Fig. I.7   Heat treatment for ferrite-austenite dual phase steel. Ae$_1$ refers to the beginning of austenite growth and Ae$_3$ to the completion of austenitization (Rao, 1985).
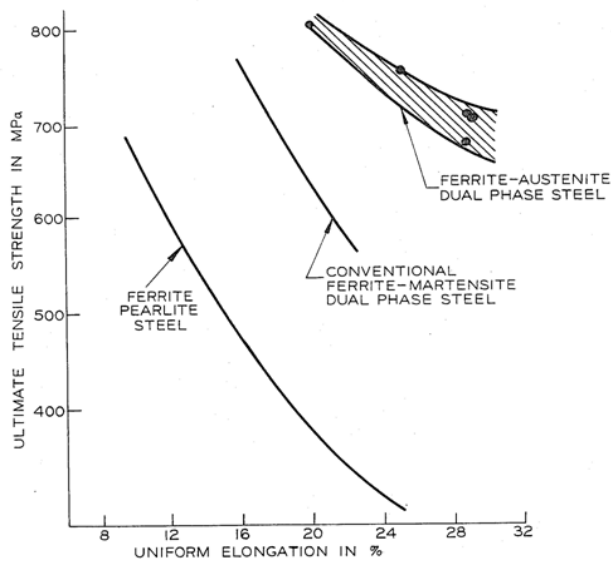

Fig. I.8   Tensile properties of ferrite-austenite dual phase steel. Five dark points correspond to experimental data (Rao, 1985).

12

Based on these experimental results, thermodynamic calculations were conducted in order to assess austenite nucleation on cementite and on ferrite (Grujicic *et al.*, 1987, Grujicic, 1990). The analysis indicated that the austenite precipitation on cementite is more likely than on ferrite. Furthermore, the austenite formed on cementite is expected to grow and consume the cementite particles. Since cementite is rich not only in Mn but also in C whereas austenite has limited C solubility, the austenite has to become diluted by growing into the ferrite matrix in order to consume cementite. Thus, the austenite growth into cementite will be hindered if the chemical potential of C in ferrite approaches the value in austenite and cementite. In that event, all of the cementite may not disappear. The experiment on two alloys whose composition is shown in Table I.4 was followed. It is found that for steel A, austenite rarely nucleated at cementite and it often formed at ferrite grain boundaries resulting in martensite during cooling. For steel B, austenite was sometimes shown to nucleate on cementite particles and its Mn content was about 10-15 wt%.

Steel	Mn / wt%	C / wt%	Si / wt%	etc. / wt%
A	1.86	0.1	0.25	Al:0.024
B	1.45	0.1	0.52	V:0.059, Cr:1.0, Ni:0.53, Mo:0.49, Ti: 0.02, Al:0.042

Table I.4 The composition of steels used for the experiment (Grujicic *et al.*, 1987).

With a thermodynamic assessment, another experiment was done on Fe - 1.8 Mn - 1.0 Si - 0.10 C wt% alloy (Haidemenopoulos, 1996). Austenite was not observed after the heat treatment illustrated in Fig. I.7 because some of it transformed into martensite during cooling, and the rest during sample preparation of transmission electron microscopy (TEM). The martensite-start temperature (Ms) obtained by dilatometry during final annealing appeared to be lower than that calculated assuming equilibrium. Moreover, the observed martensite structure contained twinning and showed enrichment of Mn by electron energy loss spectroscopy (EELS). From these facts, the stability of the austenite formed by this heat treatment was found to be higher than that of equilibrium austenite. However, there were several problems; the phase fractions were not given, the EELS result is not quantitative, and the stability of the austenite was not enough to show the desirable TRIP effect.

I.3. Idea of the Research

As mentioned in the section I.1, a major impediment to TWIP steels comes from their high levels of Mn alloying. The object of the present work was to solve this by lowering the overall concentration of Mn but locally introducing Mn-enriched austenite which exploits a TWIP effect. In order to accomplish the goal, the three step heat treatment of Rao is adopted (Fig. I.7).

After making all the samples fully or partly martensitic by quenching from the γ phase field, they would be tempered in the ($\alpha + \theta$) field to create cementite particles in the ferrite matrix (Fig. I.9). About 5-10 vol. % of cemenite is desired. If too small, the austenite that forms would be insufficient to provide a TWIP effect. If too large, it would be hard to keep high Mn concentration in cementite. Besides, the alloys are supposed to be held at the proper temperature for long enough that the cementite adequately enriches in Mn. The Mn concentration in the austenite should ideally be over about 25 wt% similar to that in the cementite.

During the third step, the alloys would be annealed in ($\alpha + \gamma$) or ($\alpha + \gamma + \theta$) field for a short time. It is important that austenite inherits the Mn in the cementite. Austenite is expected to be formed at the interface between ferrite and cementite. To meet this demand, the driving force for austenite nucleation should be small, necessitating a careful selection of the heat treatment. The

third step should be maintained only for a short time in order that the austenite will not be diluted by growth into ferrite.

Finally, the steel should contain ($\alpha + \gamma$) or ($\alpha + \gamma + \theta$) structure in which austenite is rich in Mn (Fig. I.10). Since the nucleation site for austenite is the interface between ferrite and cementite, austenite is anticipated to form into small sized particles scattered uniformly all over the ferrite matrix. The highest Mn concentration is expected to be at the α / θ interface with a steady decline towards the α / γ interface. Whether the deformation mode of the ultimate retained austenite is TWIP or TRIP depends on the levels of austenite stabilizing elements, Mn and C. The austenite near the ferrite may transform into the martensite during cooling. In conclusion, the alloy which contains ferrite, cementite and austenite or ferrite, cementite, austenite and martensite is anticipated to show a TRIP/TWIP effect during the deformation. The resulting mechanical properties are unknown with lower content of alloying elements than conventional TWIP steel. The name "TWIP-assisted steel" is adequate for the microstructure by analogy with the TRIP-assisted steel.
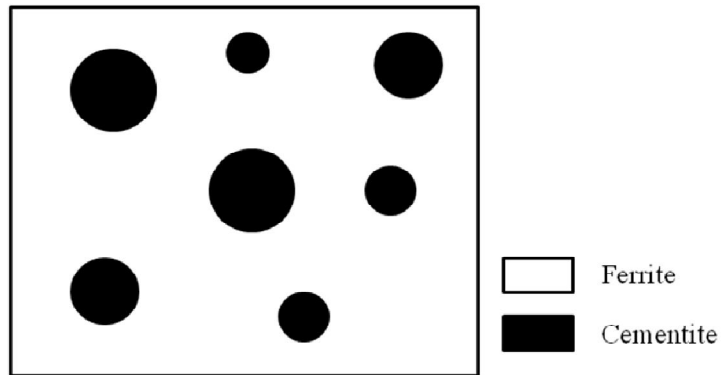
Fig. I.9   The expected structure after the second heat treatment in ($\alpha + \theta$) region. It consists of cementite particles scattered in ferrite matrix.
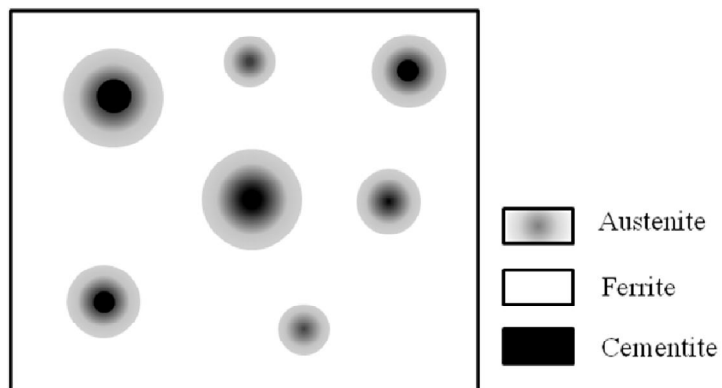

Fig. I.10 The expected structure after the final heat treatment in ($\alpha + \gamma$) or ($\alpha + \gamma + \theta$) region, consisting of austenite particles scattered in ferrite matrix. Some remaining cementite may be found adjacent to the austenite. The gradation of the gray is intended to illustrate manganese concentration gradients. The darker the color, the more manganese it contains.

II. Experimental Methods

II.1. Overall Experimental Flow Chart

The flow chart of experiments is shown in Fig. II.1. Both the alloy composition and its heat treatment were first designed by calculation. The heat treatment methods were selected considering the characteristics such as time and temperature. The main research deals with microstructure analysis using several kinds of instruments, some equipped with spectrometers. Then, the tensile properties of the final structure were investigated.
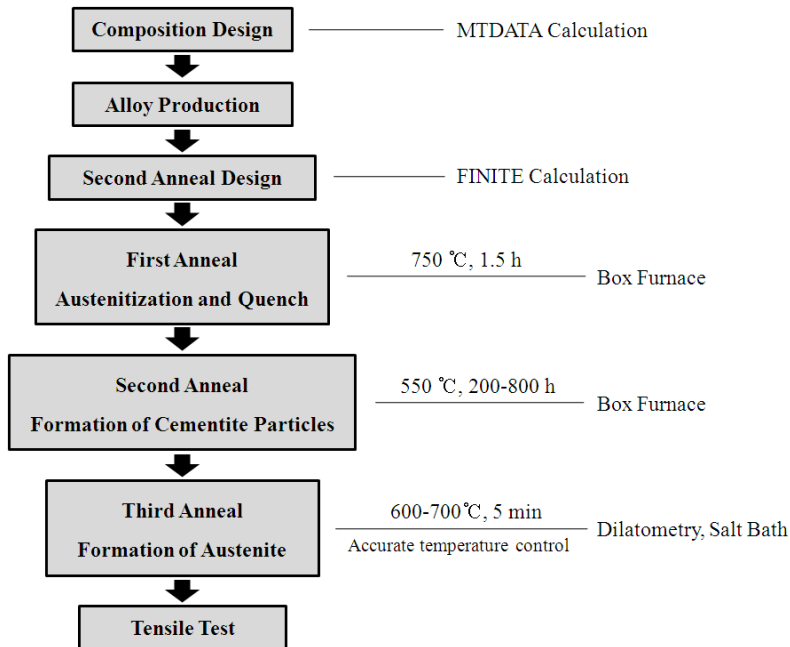

Fig. II.1   A flow chart of all experiments. Important methods are connected to the corresponding experimental steps.

II.2. Alloy Composition

Calculations using Metallurgical and Thermochemical DATAbase (MTDATA) were carried out to estimate the volume fractions of the phases and their compositions at the desired temperature. The composition and annealing temperature were decided based on these calculations.

II.2.1. Metallurgical and Thermochemical DATAbase (MTDATA)

MTDATA is a software introduced by the National Physical Laboratory for the calculation of phase equilibria and thermodynamic properties in given systems (Davies *et al.*, 2002). The calculation is carried out using a Gibbs free energy minimization algorithm. This means that the results are generally given for equilibrium condition. The multiphase module of MTDATA version 4.81 has been utilized using TCFE database (TCAB database for steels, version 1.22). The input values are the composition of the system, constant pressure or volume condition, and the temperature range. Three components, Fe, Mn and C, and four of the phases, liquid, ferrite, austenite and cementite were included in all calculations which were for 1 atm pressure.

II.2.2. Composition Design

Two alloying elements, Mn and C, were chosen for study because they are

the basic constituents in TWIP steels. Several other solutes such as Si or Al can be added afterwards if needed. However, since it was the very first time to develop a new alloy, the composition was kept simple. The calculation steps were 1 wt% from 1 to 8 wt% for Mn and 0.2 wt% from 0.2 to 1.4 wt for C.

The temperatures for calculation were chosen next. Since the equilibrium would not be reached in the short period during the third anneal, it cannot be calculated and only the second anneal case was calculated. Therefore, temperature should be in the ($\alpha + \theta$) field. In addition, a competition between Mn diffusion rate and austenite formation should be taken into account. Mn is expected to enrich in the cementite during the second anneal at a rate which is greater at high temperatures. However, too high a temperature can stimulate austenite formation. Therefore, the range 450-600 ℃ was judged to be adequate for the second anneal, specifically 450, 500, 550, 600 ℃.

Then, two most important factors are as follows:

i) The volume fraction of cementite after the second anneal in ($\alpha + \theta$) field.

ii) The equilibrium Mn concentration of cementite after the second anneal.

The volume fraction of cementite is significant because it is related directly to that of austenite. Likewise, its Mn concentration will affect that of austenite. Hence, these two values were plotted respect to Mn and C content for each temperature (Figs. II.2 and II.3) and three values of appropriate Mn and C concentration were selected.

According to Fig. II.2, the higher the C content, the higher the cementite volume percent, regardless of Mn content. It is a reasonable result since ferrite has limited C solubility and most of the C has to be held by cementite. As a result, the amount of cementite should be increased in order to take in more C in the alloy. As long as austenite is not formed, the Mn content does not have a large effect on cementite volume percent, but influences Mn concentration in cementite. In addition, the values of the cementite volume fraction hardly change by temperature. However, some of the upper left corner regions are distorted as it gradually reaches the higher temperature. These parts are where Mn amount is large comparing with C content and austenite exists due to the effective austenite stabilizer, Mn.
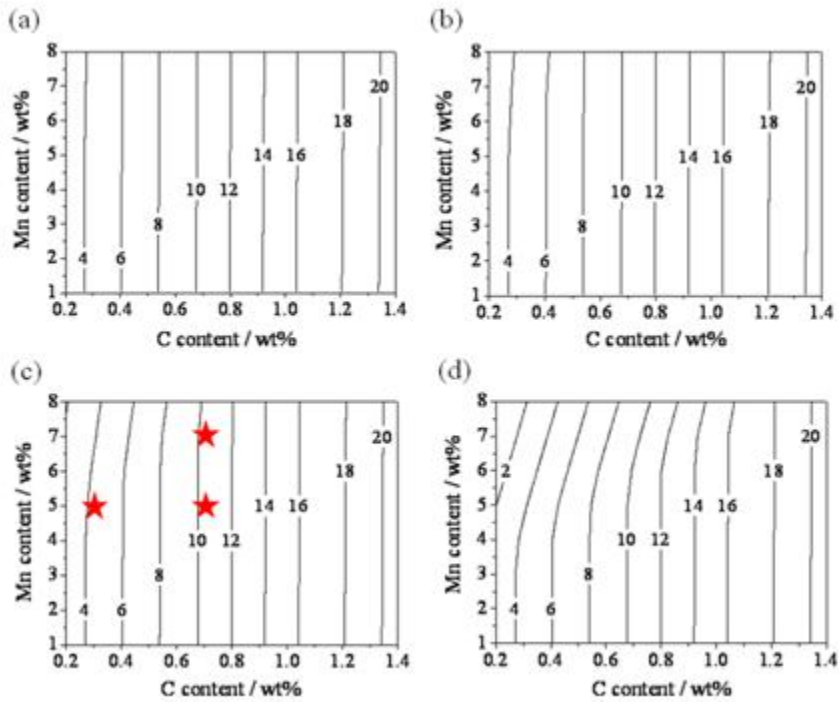
Fig. II.2 Contour maps of cementite volume percent in respect to the manganese and carbon content in the alloy during the second anneal. Each graph corresponds to a different temperature: (a) 450 ℃, (b) 500 ℃, (c) 550 ℃ and (d) 600 ℃. The upper left distorted regions in (b), (c) and (d) are where austenite would be formed. The three selected compositions are marked by stars in (c).
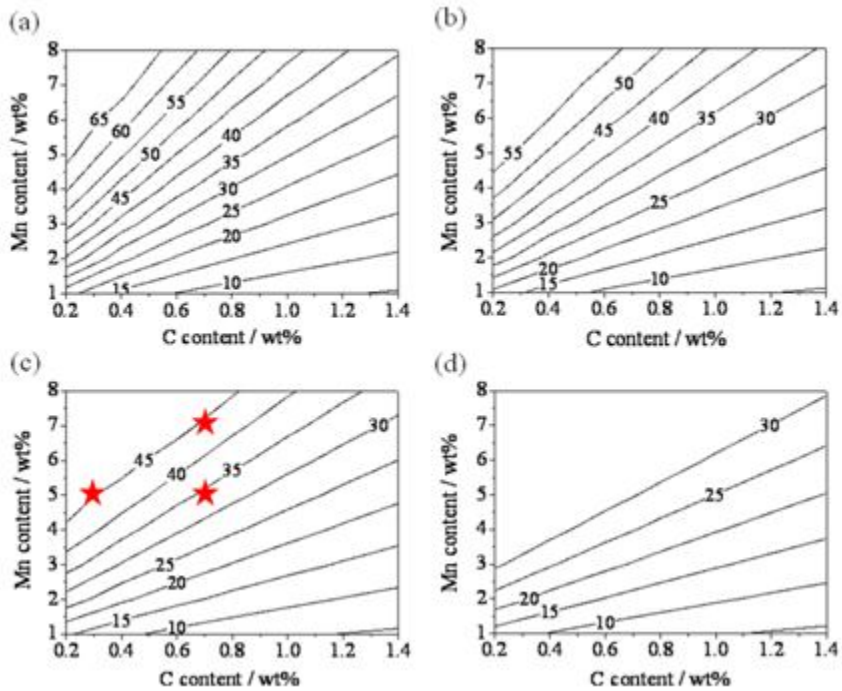
Fig. II.3 Contour maps of Mn concentration of cementite in respect to overall manganese and carbon content in the alloy during the second anneal. Each graph corresponds to a different temperature: (a) 450 ℃, (b) 500 ℃, (c) 550 ℃ and (d) 600 ℃. The three selected compositions are marked by stars in (c).

As shown in Fig. II.3, the Mn concentration in cementite increases in respect to the overall Mn content, if the C content is kept constant. The reason is that Mn should be taken in by the unchanged amount of cementite. Besides, Mn in cementite is reduced as C content increases when the overall Mn

23

content is fixed. It is because a large volume fraction of cementite results in dilution of Mn in cementite. As mentioned in Fig. II.2, the upper left regions are where austenite formed, so some of Mn is incorporated in austenite and hence, not partitioned into cementite. In addition, there is a small effect of temperature. The Mn concentration gets lower if the temperature increases. It seems to be caused by the change of Mn solubility in ferrite.

The second annealing temperature was therefore selected using the data plotted in Figs. II.2 and II.3. Since high temperature is desirable for Mn diffusion into cementite, 550 ℃ was selected. At 600 ℃, austenite is formed over a large composition region so this temperature is excluded.

As in Fig. II.2 (c), C content is decided as 0.3 and 0.7 wt% by choosing the points of approximately 5 vol. % and 10 vol. % of cementite. Also in Fig. II.3 (c), Mn content is decided as 5 and 7 wt% since these points are where the Mn content in cementite is the highest at the given temperature. The values are enough for the austenite to show TWIP effects. One more point was picked to see the effect of Mn and C separately. The overall compositions of three alloys are shown in Table II.1.

Steel	Mn / wt%	C / wt%	Fe
Alloy 1	5	0.3	balance
Alloy 2	5	0.7	balance
Alloy 3	7	0.7	balance

Table II.1 Ideal compositions of the alloys decided based on the MTDATA calculations.

II.2.3. Actual Composition

The alloys were produced by POSCO. The manufacturing steps consisted of vacuum melting and casting to produce a 15 kg ingot for each alloy. It was then heat-treated at 1200 ℃ for 1 h, hot-rolled into a 15 mm plate while austenitic and air cooled. The actual compositions are shown in Table II.2. S, Al and N contents are so small that they are impurities and ignored in further calculations. The mass percent of phases and Mn content in each phase at 450- 750 ℃ for each alloy were calculated by MTDATA (Figs. II.4-II.6)

Steel	Mn / wt%	C / wt%	S / wt%	Al / wt%	N / wt%	Fe
Alloy 1	5.02	0.250	0.0025	0.027	0.0039	balance
Alloy 2	4.92	0.650	0.0027	0.024	0.0039	balance
Alloy 3	7.58	0.621	0.0020	0.032	0.0053	balance

Table II.2 Actual compositions of the alloys. Compositions were analyzed by optical emission spectrometry.
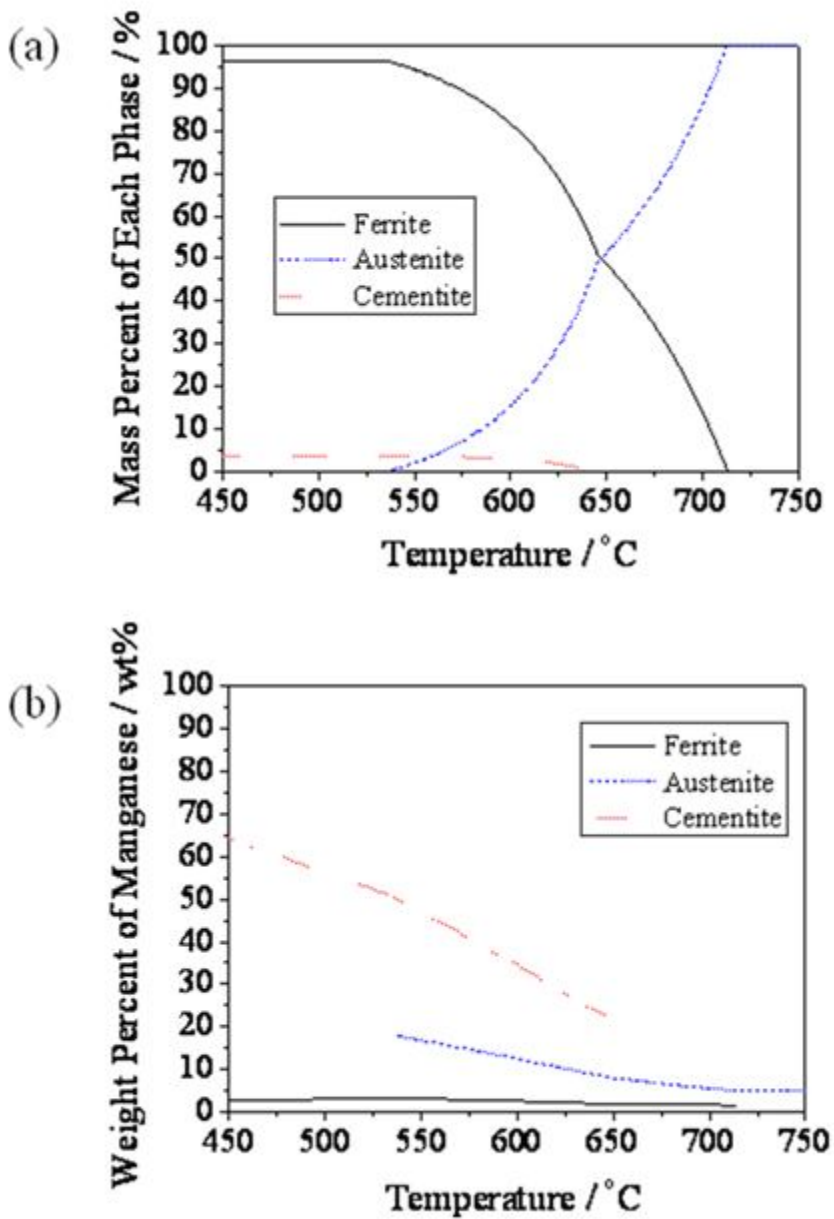
Fig. II.4 (a) Mass percent of the phases, (b) weight percent of Mn of Alloy 1 as a function of temperature.
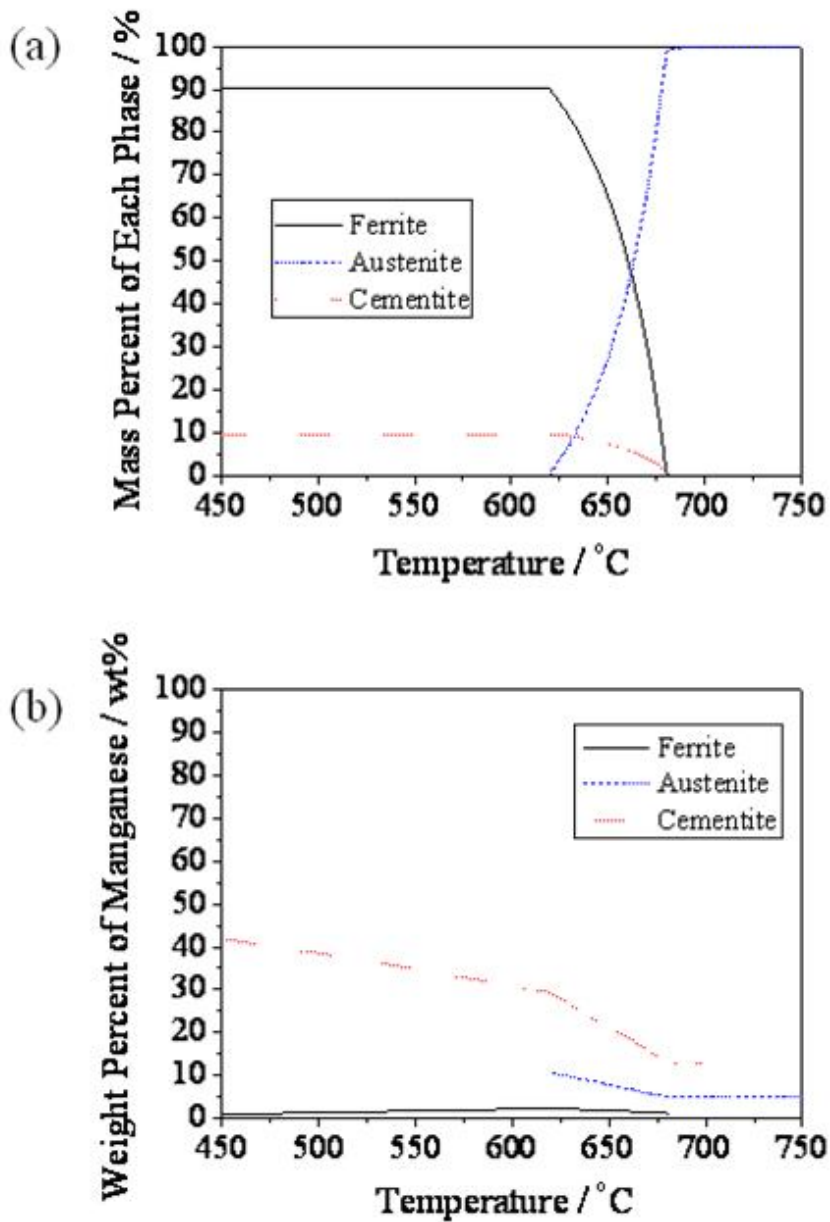
Fig. II.5   (a) Mass percent of the phases, (b) weight percent of Mn of Alloy 2 as a function of temperature.
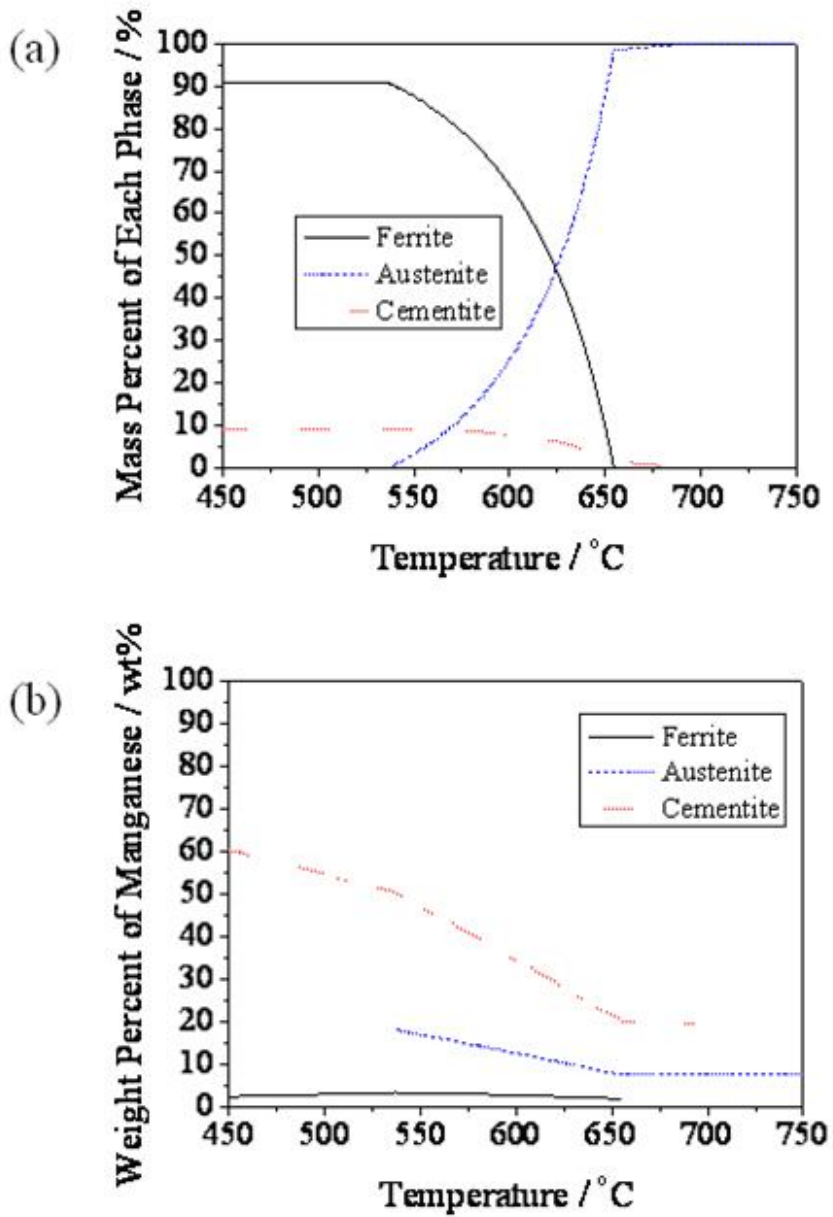
Fig. II.6   (a) Mass percent of the phases, (b) weight percent of Mn of Alloy 3

as a function of temperature.

Notice that there are three-phase ($\alpha + \theta + \gamma$) field which is not possible in plain carbon steels. Moreover, for Alloy 2 and Alloy 3, there is no two-phase ($\alpha + \gamma$) field.

Accurate values of the amount of the cementite and Mn content in cementite at 550 ℃ are given in Table II.3. Referring to the compositions of the alloys (Table II.2), it can be concluded that the amount of cementite of Alloy 1 is small, since there is smaller content of C and those of Alloys 2 and 3 are the same because of approximately the same C content. Moreover, the Mn concentration of cementite is lowest for Alloy 2 since the overall Mn content in respect to C content is the least.

Steel	Mass percent of cementite / %	Mn content in cementite / wt%
Alloy 1	3.6	47.1
Alloy 2	9.7	34.8
Alloy 3	9.1	47.1

Table II.3 Calculated equilibrium mass percent of cementite and Mn content in cementite at 550℃ in each alloy.

II.3.   Heat Treatment

II.3.1.   First Anneal: austenitization and quench

The object of the first anneal is to initialize the microstructure of all alloys. The annealing took place at 750 ℃ for 1.5 h to minimize austenite grain growth. The furnace used was Barnstead Thermolyne 1400 Digital Muffle Furnace. The specimens were wire-cut from the hot-rolled plate of 15 mm thickness, with dimensions 25 × 20 × 15 mm (Fig. II.7). All the specimens were encapsulated in vacuum quartz tubes during the heat treatment. It took approximately 50 minutes to heat the furnace up to 750 ℃. After the treatment, the tubes were broken and the specimens immediately quenched in water.
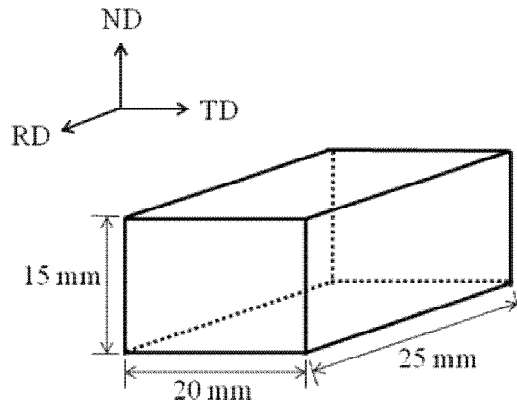
Fig. II.7 The specimen shape for the first and second annealing for microstructure analysis. RD: rolling direction, TD: transverse direction, ND: normal direction.

II.3.2. Second Anneal: formation of cementite particles

The second anneal tempers the martensite to form cementite and allows Mn to partition into cementite. Additional purpose is to coarsen cementite. The cementite size after tempering is expected to be in the micrometer range. The diffusion of Mn into cementite is expected to be slow because of low annealing temperature, 550 ℃, thus necessitating long heat treatment. This anneal is carried out in the same muffle furnace as for the first anneal, preparing the specimen in the quartz tube. The alloys were air cooled after the treatment.

II.3.3. Third Anneal: formation of austenite

The goal of the third anneal is to form austenite at the α/θ interface. To prevent austenite formation at the α grain boundaries, the temperature must be accurately controlled. Besides, in order to retain Mn in austenite, the annealing period has to be kept short. Therefore, the alloys were heat-treated using a BÄHR-Dilatometer DIL 805. The heat treatment is illustrated in Fig. II.8. The temperature for isothermal treatment was chosen by trial and error to get approximately 5 vol. % austenite and the time period was selected as 5 min. The heating and isothermal treatments were done under vacuum with cooling using helium gas injection. The shape of specimens was cylindrical,

the diameter of which was 5 mm and height was 10 mm.
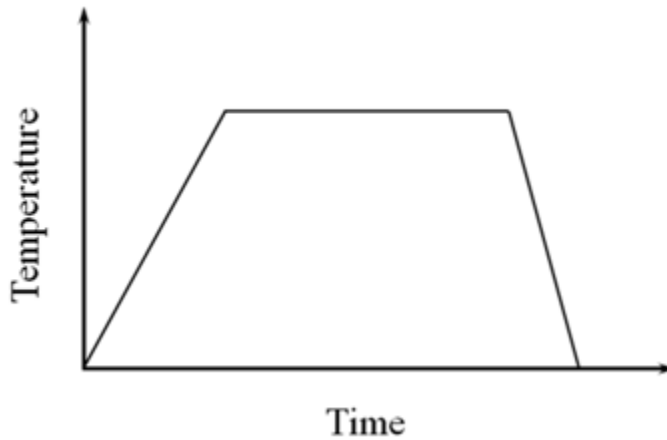
Fig. II.8 Schematic illustration of the third heat treatment used to form austenite. The isothermal temperature is within ($\alpha + \theta + \gamma$) region. Heating rate was 5 ℃·s^{-1} and cooling rate, -10 ℃·s^{-1}.

II.3.4. Heat Treatment for Tensile Specimen

Annealing method for tensile specimen was different because of the specimen dimensions. Alloys were roughly cut into parallelepipeds 15 × 15 × 130 mm. During the first and the second anneal, the samples were sealed in evacuated quartz tubes. The furnace used in the first annealing and the second annealing was a Samheung SH-MF2A furnace. It took about 1 h to reach 750 ℃ and 50 min to 550 ℃. For the third anneal, a salt bath was used to give homogeneous temperature throughout each specimen. Five minutes were

measured after reaching certain temperature and then the specimens were cooled in oil. When all the heat treatments were finished, the samples were precisely manufactured into tensile specimens.

II.4. Microstructure Analysis

II.4.1. Microscopy

Microstructures after each heat treatment were analyzed using optical microscopy (OM), scanning electron microscopy (SEM) and transmission electron microscopy (TEM).

A conventional sample preparation method was utilized for OM and SEM. Samples were cut into the proper size, ground with silicon carbide paper and polished with 6 and 1 μm diamond suspension. The samples were then etched in 1% nital. However, those samples consisting of γ, whose size is over 10 μm, were etched in both saturated aqueous picric acid solution and nital. OM instrument was Olympus BX60M and SEM instruments were JEOL JSM-5900 and Carl Zeiss ULTRA 55 FE-SEM. For EDS analysis, ZAF corrections are made automatically by the software supplied by the manufacturer.

For TEM, samples were ground to a thickness of 100 μm, punched into 3 mm diameter discs and then finally ground to 80-90 μm. Discs were

electropolished by either of the electrolytes: 7 % perchloric acid with acetic acid or 5 % perchloric acid and 20% glycerine with ethyl alcohol. For the former electrolyte, the polishing temperature was 15-20 ℃, and for the latter, -5-10 ℃. The instruments used were 200 kV FEI Tecnai G2 and 300 kV FEI Tecnai F30 for bright/dark field images, diffraction patterns and point / line energy dispersive spectroscopy (EDS).

II.4.2. Limitations of EDS Quantitative Analysis

The electron microscopes including SEM and TEM gain the signals of electrons which have interacted with the specimen to provide information for both morphology and quantitative analysis. The electrons penetrate a finite depth and this means that the signals can be generated within the sample. The different kinds of electron signals emerging from the sample are illustrated in Fig. II.9. EDS uses characteristic X-rays which come from all the interaction volume including the deepest part. The depth of penetration varies with incident beam energy (Fig. II.10). In the case of SEM, the incident electron energy is 10-20 keV, which results in electron mean free path length up to about 1 μm. Therefore, if the particle size is less than 1 μm, the surrounding material will also contribute to the measured signal (Fig. II.11(a)). Likewise, a particle submerged in the matrix will have its signal mixed with that from the

matrix (Fig. II.11(b)).

On the other hand, overlap of information can be minimized by using TEM using thin foil samples (Fig. II.11(c)), although three-dimensional effects can still lead to confusion (Fig. II.11(d)).

Another limitation of EDS in TEM and SEM is that C cannot be included in quantitative analysis because of C contamination on the specimen. Hydrocarbon from the vacuum pump is decomposed into H and C by high energy electrons and C is accumulated on the specimen.

In conclusion, it should be noticed that the quantitative data using electron microscopy should be interpreted with care.
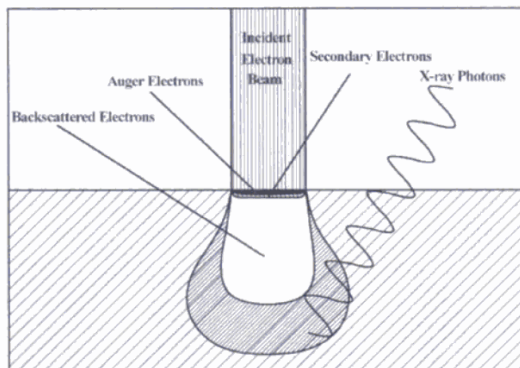
Fig. II.9 Schematic illustration of the volume of material that is probed by an incident electron beam together with the volumes from which X-rays and backscattered Auger and secondary electrons emanate (Flewitt and Wild, 1994).
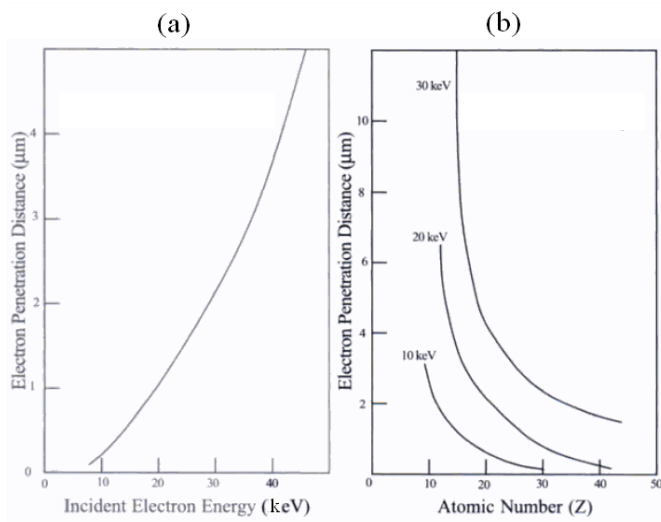
Fig. II.10 The mean free path length of electrons (a) in stainless steel as a function of electron energy and (b) as a function of atomic number of the material being probed for 10 keV, 20 keV and 30 keV electrons (Flewitt and Wild, 1994).
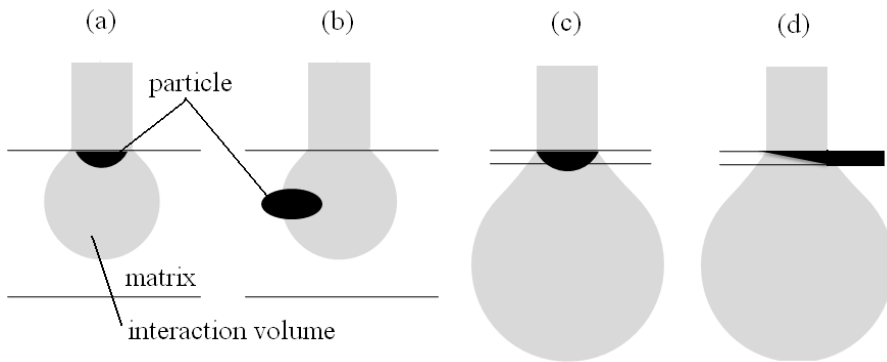
Fig. II.11 Illustrations of the limitations of electron microscopy: (a) the particle measurement using SEM, (b) the matrix measurement using SEM, (c) the particle measurement using TEM, (d) the big particle measurement using TEM.

II.4.3. X-Ray Diffraction (XRD) Analysis

XRD analysis was done in order to figure out phase fractions after each heat treatment step. First, the samples for microstructure analysis were polished using conventional method as in OM and SEM. However, the samples were not etched. In the case of samples for tensile testing, they were polished using LectroPol with 6 % perchloric acid and ethanol. Approximately top 100 µm was removed by electropolishing in order to remove part which could have been deformed during polishing. The diffraction patterns were obtained by Bruker AXS D8 ADVANCE with Sol-X detector using Cu Kα radiation of 0.1542 nm with an operation voltage of 40 kV and current of 40 mA. The pattern range was from 2 θ of 35˚ to 105˚, in the step size of 0.02˚ and 7 s dwell time for each step for microstructure analysis samples and in the step size of 0.03˚ and 4.5 s dwell time for each step for tensile test samples. The phase fractions were then calculated by Rietveld refinement method (Rodriguez-Carvajal, 2001).

The principle of the refinement method involves the calculation using a number of experimental parameters to acquire the best fit of the data. To get the best fit, χ^2 (Eq. II.1) is minimized.

$$\chi^2 = \sum_i w_i \left\{ y_i - y_{ci} \right\}^2 \qquad \text{(Eq. II.1)}$$

where y_i is the observed intensity at data point i, y_{ci} is the calculated intensity at i and w_i is a weighting parameter which is given as the inverse of the variance of y_i. y_{ci} is shown in Eq. II.2 in detail.

$$y_{ci} = \sum \left\{ S_j |F_{kj}|^2 \phi_{ikj} (2\theta_i - 2\theta_k) L_{kj} M_{kj} T_{oj} P_{kj} \right\} + y_{bi} \quad \text{(Eq. II.2)}$$

where k is the index of overlapping neighboring Bragg reflections, j is the index of phases, S_j is the scaling factor per phase, F_{kj} is the structure factor, ϕ_{ikj} is the profile function, L_{kj} is the Lorentz polarization factor, M_{kj} is the multiplicity, T_{oj} is the overall temperature factor, P_{kj} is the preferred orientation function, y_{bi} is the background intensity at data point i. After refinement, S_j can be included in the calculation for quantitative analysis, F_{kj} is for atomic parameters such as lattice parameters and atomic positions. Moreover, ϕ_{ikj} is used in particle size and strain analysis.

In quantitative analysis, the weight fractions of phases (W_p) are obtained from S_j as in Eq. II.3.

$$W_p = \frac{S_p(AMV)}{\sum_j S_j(AMV)_j} \qquad \text{(Eq. II.3)}$$

where A is the number of formula units per unit cell, M, the mass of the formula unit, V, the unit cell volume.

The result of Rietveld method is usually assessed by three agreement factors; weighted profile factor (R_{wp}, Eq. II.4), expected weighted profile factor (R_{exp}, Eq. II.5) and reduced chi (χ_v, Eq. II.6).

$$R_{wp} = 100 \left(\frac{\sum_{i=1}^{N} w_i |y_i - y_{ci}|^2}{\sum_{i=1}^{N} w_i y_i^2} \right)^{\frac{1}{2}} \qquad \text{(Eq. II.4)}$$

$$R_{exp} = 100 \left(\frac{N-p}{\sum_{i=1}^{N} w_i y_i^2} \right)^{\frac{1}{2}} \qquad \text{(Eq. II.5)}$$

$$\chi_v = \frac{R_{wp}}{R_{exp}} = \left(\frac{\chi^2}{n-p} \right)^{\frac{1}{2}} \qquad \text{(Eq. II.6)}$$

where N is the total number of pattern points being in an account of refinement and p is the number of refined parameter. Therefore, $N-p$ is the number of degrees of freedom. Even though these agreement factors are

reasonable to assess the goodness of fit and will be provided with the results, the results should not be assessed only with these factors.

Rietveld refinements were carried out using the software Fullprof version 4.60. Phases that were considered were ferrite, austenite and cementite. The lattice parameters and atom positions including thermal factors of each phase were given as cell information. During refinement, lattice parameters and thermal factors of atoms in ferrite and austenite are refined. Even though all the general atomic positions and thermal factors have to be refined, those of cementite were not refined because it had resulted in divergence. Initial cell information is given in Table II.4. Notice that martensite cell information is given as the same as ferrite.

Phase	Lattice parameter / Å	Atomic position				Thermal factor
		Atom	x	y	Z	
Ferrite/ Martensite	2.8670	Fe	0	0	0	0
Austenite	3.3569	Fe	0	0	0	0
Cementite	a = 4.4623	Fe	0.3330	0.1752	0.0662	0
	b = 5.1281	Fe	- 0.1602	0.0358	0.2500	0
	c = 6.6512	C	- 0.4379	0.1236	- 0.2500	0

Table II.4 Initial cell information for Rietveld refinement (Jang *et al.*, 2009, Onink *et al.*, 1993).

II.4.4. Limitations of XRD Analysis

After the second anneal, all samples contain cementite. Therefore, cementite mass percent were to be obtained by the refinement. However, it is found that there is possibility to be underestimated. It is because of the combination of following reasons: small mass percent, a number of cementite peaks (Fig. II.12 and, the particle size of cementite. Since the cementite size is within 2 micrometer range, the XRD peaks would be broadened and for small mass percent peaks would be low intensity. A number of broadened small peaks may be seen as background. Thus, smaller percent would be obtained.

The texture effect was also ignored even though texture is expected during hot rolling process. Sometimes, this gives the result of high χ^2.

In order to compensate the errors, the value of cementite volume fraction is obtained by counting the pixels which is occupied by cementite particles. For this analysis, at least seven 10×10 μm areas were investigated.
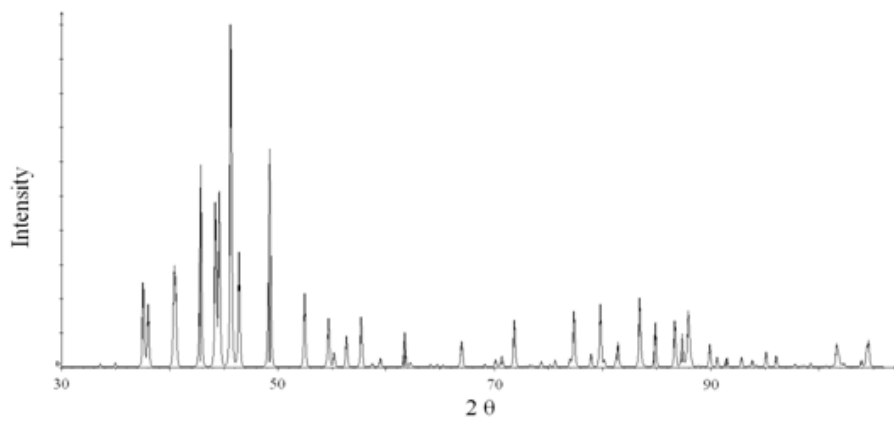
Fig. II.12 Simulated XRD peaks of cementite by CaRine Crystallography software version 3.1.

II.4.5. Carbon Concentration of Austenite

As mentioned in section II.4.2, C content cannot be obtained by direct analysis using EDS. Therefore, an indirect method was adopted in order to calculate carbon content in austenite. As lattice parameter of austenite is related to the C and Mn content (Eq. II.7), the C content can be calculated if lattice parameter and Mn content is known (Dyson and Holms, 1970). The lattice parameter was acquired from XRD results and Mn content from EDS results. Notice that the value abtained from EDS analysis cannot be substituted to $(wt\%Mn)$ term because the carbon content has to be considered. The relation between $(wt\%Mn)$ and the value of Mn content obtained from EDS, $(wt\%Mn^{eds})$ is given in Eq. II.8.

$$a_{\gamma} = 3.578 + 0.033 \cdot (wt\%C) + 9.5 \times 10^{-3} \cdot (wt\%Mn) \qquad \text{(Eq. II.7)}$$

$$(wt\%Mn) = (wt\%Mn^{eds}) \cdot \left(1 - \frac{(wt\%C)}{100}\right) \qquad \text{(Eq. II.8)}$$

II.5. Mechanical Testing

II.5.1. Hardness Testing

Both bulk and micro hardness test were done. For bulk hardness test, load was 2 kg and dwell time was 10 s using a Wolpert Vickers hardness tester 452SVD. For microhardness test, load was 100 or 300 g and the dwell time

was 10 s using Future-tech FM700. At least 10 tests were carried out in each case and averaged.

II.5.2. Tensile Testing

Tensile tests were done after heat treatment. There were two kinds of specimens, longitudinal and transversal, that experienced the same heat treatment. Tensile specimens were manufactured as small-size specimens proportional to ASTM A-370 (Fig. II.14). All the experiments were carried out with the strain rate of 0.001 s^{-1} at room temperature using a Zwick / Roell Universal tensile testing machine.
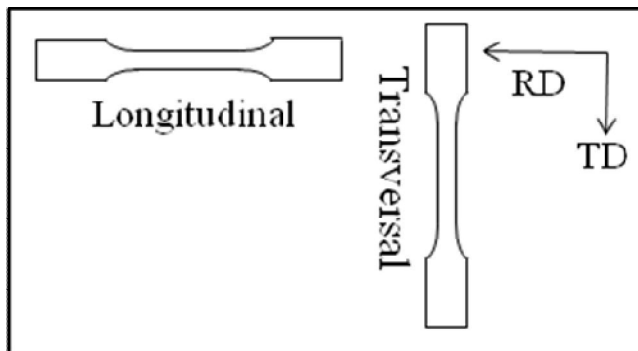
Fig. II.13A schematic of two kinds of specimens, longitudinal and transversal, of the same heat treatment. Longitudinal one is parallel to the rolling direction (RD) and transversal one to the transversal direction (TD).
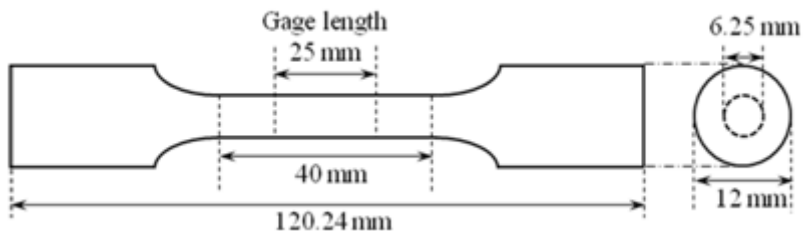
Fig. II.14 A schematic of tensile specimens which are small-size specimens proportional standard sample following ASTM A-370.

III. First Anneal – Austenitization and Quench

III.1. Alloy 1

An optical micrograph is shown in Fig. III.1 and quantitative XRD analysis results are given in Table III.1. Since all the regions of the sample were observed to be martensitic, the 8 wt% of austenite existed in retained form. There were dark contrast bands along the rolling direction. These bands are usual phenomena in Mn containing steels. Since Mn has low diffusivity, Mn segregation bands are removed only after prolonged annealing at temperatures as high as 1200 ℃. Both light and dark-contrast regions were observed (Fig. III.2) and the EDS results are shown in Table III.2 and Table III.3, respectively.
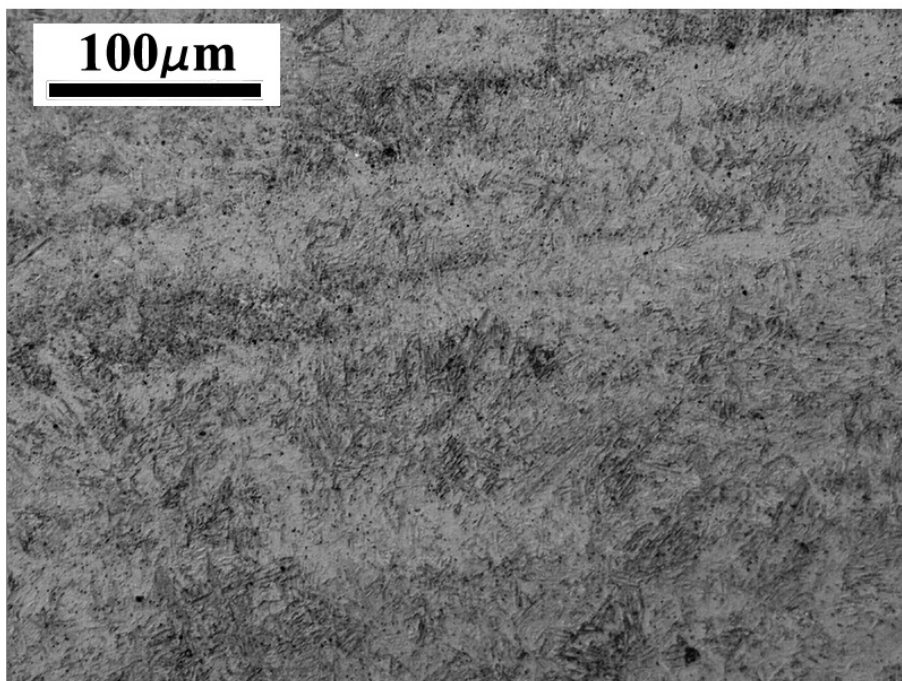
Fig. III.1 An optical micrograph of Alloy 1 after the first anneal (austenitization and quench). The sample is etched with 1 % nital. Notice the bands of dark contrast that are parallel to the rolling direction.

Martensite / wt%	Austenite / wt%	Cementite / wt%	R_{wp}	R_{exp}	χ^2
92 ± 1	8 ± 1	0 ± 1	18.4	13.97	1.73

Table III.1 Quantitative XRD analysis results of Alloy 1 after the first anneal, using Rietveld refinement method.

Region index	Mn / wt%	Fe / wt%
Light 1	4.21 ± 0.34	95.79 ± 0.81
Light 2	3.86 ± 0.34	96.14 ± 0.81
Light 3	4.96 ± 0.35	95.04 ± 0.81
Average	4.34 ± 0.66	95.66 ± 0.99

Table III.2 EDS overall spectrum results of three light-contrast regions with FE-SEM. Note that the C content is not included in the analysis.

Region index	Mn / wt%	Fe / wt%
Dark 1	6.46 ± 0.37	93.54 ± 0.80
Dark 2	5.97 ± 0.36	94.03 ± 0.81
Dark 3	5.55 ± 0.36	94.45 ± 0.81
Average	5.99 ± 0.58	94.01 ± 0.93

Table III.3 EDS overall spectrum results of three dark-contrast regions with FE-SEM. Note that the C content is not included in the analysis.
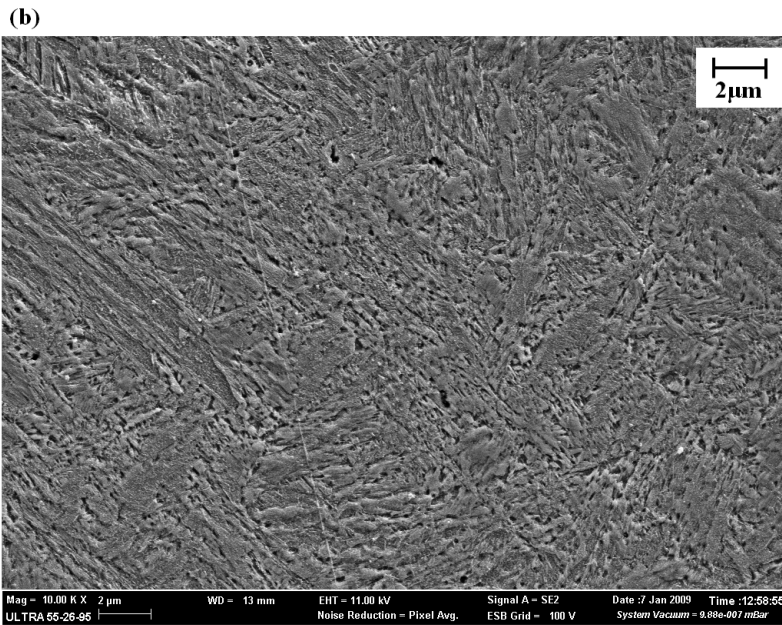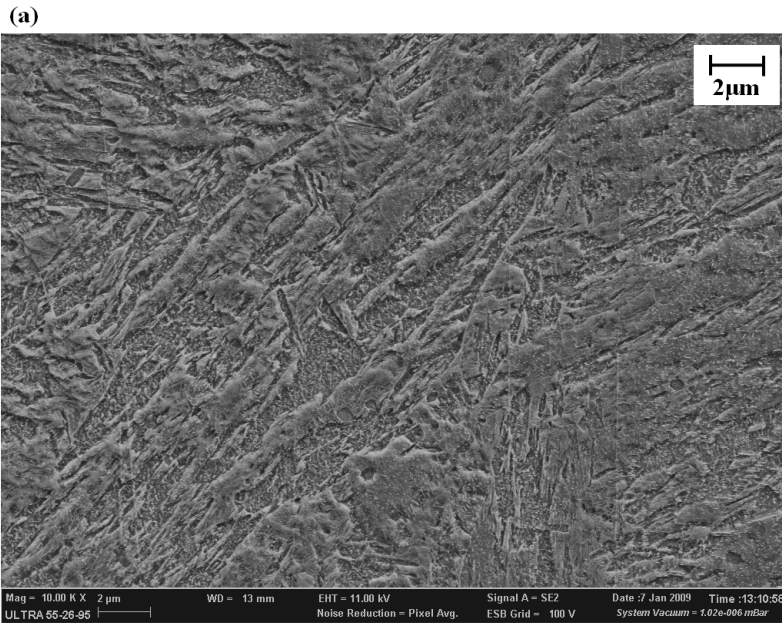
Fig. III.2 SEM images of different Mn regions in Alloy 1 which is etched

with 1 % nital. (a) The light-contrast region. (b) The dark contrast region.

From the results shown in Tables III.2 and III.3, more probable values can be obtained by assuming that C is uniformly distributed given its greater mobility. By this procedure, the average values are Fe-4.33 ± 0.66 Mn-0.25 C (wt %) for the light region and Fe-5.98 ± 0.58 Mn-0.25 C (wt %) for the dark region. Hence, it is concluded that the dark region is rich in Mn and that the segregation is retained after the anneal.

In Fig. III.2, even though two regions share a martensitic structure, the morphologies of dents and ledges are different. In light-contrast regions, the area of dents and ledges are similar (Fig. III.2 (a)). On the other hand, in dark-contrast regions, the area of dents is smaller than that of ledges and deeper than in light-contrast regions. It seems that the Mn concentrations are different for martensite in each region and this results in different etching abilities.

However, the values of micro-hardness were similar: the light-contrast region, HV 570 ± 30 and the dark-contrast region, HV 584 ± 18. It seems that the hardness is more influenced by the phase than the composition.

III.2. Alloy 2

Quantitative XRD results and an optical micrograph are given in Table III.4 and Fig. III.3, respectively. As can be seen in Fig. III.3, 17 wt% of austenite was retained and could be observed as the separate phase, the

morphology of which was parallel to the rolling direction. These austenite bands were surrounded by martensite. A high magnification image of martensite is shown in Fig. III.4. The EDS results of martensite and austenite are shown in Tables III.5 and III.6, respectively.

Martensite / wt%	Austenite / wt%	Cementite / wt%	R_{wp}	$R_{\exp}$	χ^2
83 ± 1	17 ± 1	0 ± 1	21.7	14.59	2.21

Table III.4 Quantitative XRD analysis results of Alloy 2 after the first anneal by Rietveld refinement method.

Region index	Mn / wt%	Fe / wt%
Martensite 1	4.97 ± 0.28	95.03 ± 0.63
Martensite 2	4.29 ± 0.28	95.71 ± 0.64
Martensite 3	5.02 ± 0.28	94.98 ± 0.64
Average	4.76 ± 0.49	95.24 ± 0.76

Table III.5 EDS overall spectrum results of three martensite regions with FE-SEM. Note that the C content is not included in the analysis.

Region index	Mn / wt%	Fe / wt%
Austenite 1	7.10 ± 0.29	92.90 ± 0.63
Austenite 2	6.61 ± 0.30	93.39 ± 0.64
Austenite 3	6.94 ± 0.29	93.06 ± 0.63
Average	6.88 ± 0.39	93.12 ± 0.68

Table III.6 EDS overall spectrum results of three austenite islands with FE-SEM. Note that the C content is not included in the analysis.
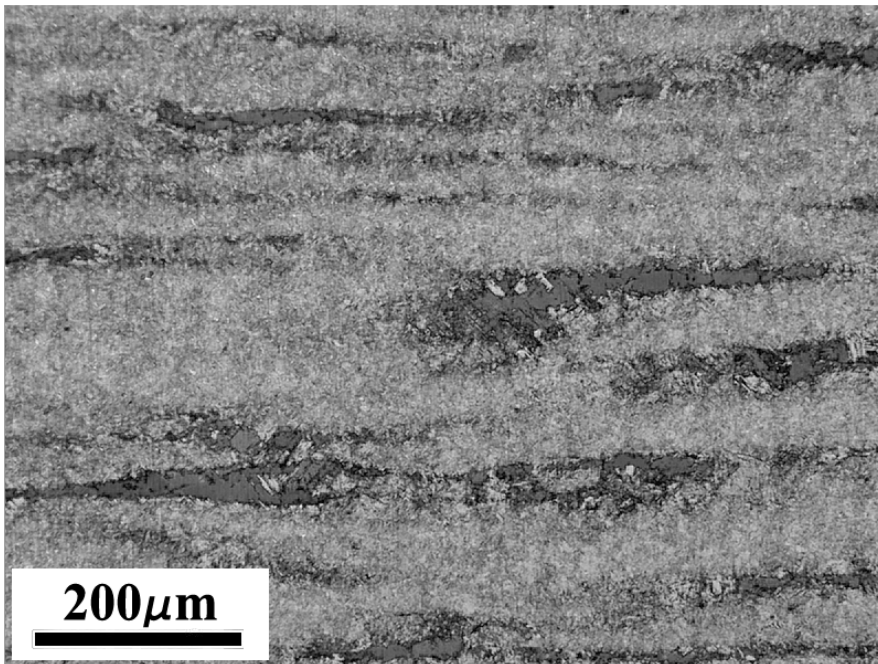
Fig. III.3 An optical micrograph of Alloy 2 after first anneal (austenitization and quench). The sample is etched with 1% nital. The subjected area consists of austenite bands in martensite matrix. The austenite bands are parallel to rolling direction.
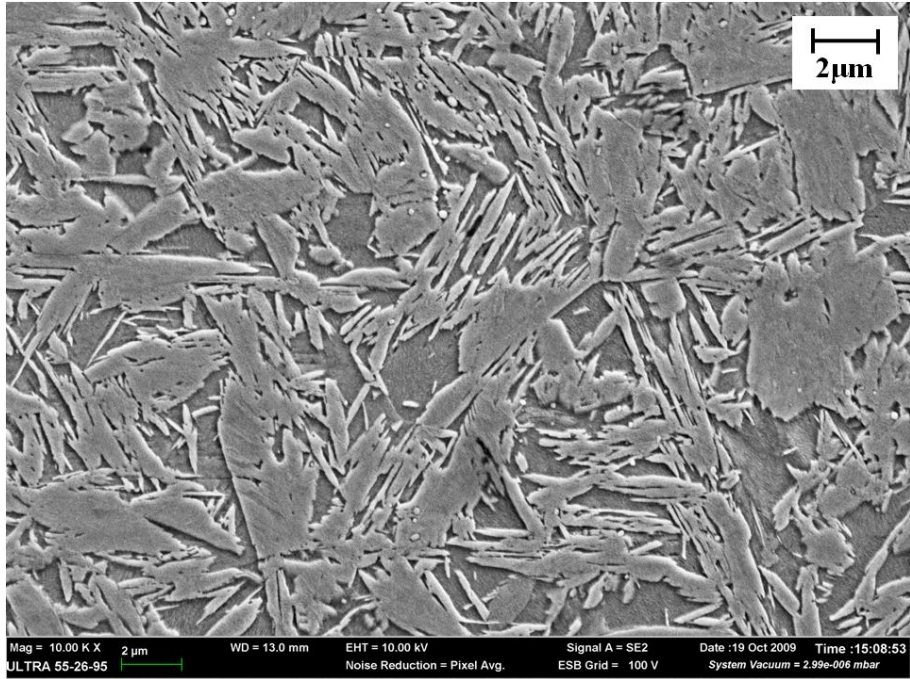
Fig. III.4 An SEM image of martensite region.

Unlike section III.1, the C content of austenite could be calculated from XRD and EDS data and the composition was Fe-6.86 ± 0.39 Mn-0.250 ± 0.031 C (wt%). Considering that C can diffuse easily and distribute almost homogeneously throughout the alloy, the resulted C seems to have been underestimated but no reason was found. Even though the C content is unreasonable, composition results imply that Mn segregation is retained even after austenitization and that the high Mn regions remain as austenite, while low Mn regions transform into martensite. Given its composition, the morphology of martensite was platelike. However, austenite could contribute

to the EDS results of martensite since the plates were surrounded by austenite (Fig. III.4).

The hardness of martensite was HV 637 ± 36 and of austenite, HV 293 ± 63. It could be argued that the martensite contributes to the hardness of austenite, given that the latter is surrounded by martensite. The large standard deviation in the measured hardness of austenite implies this effect.

III.3. Alloy 3

Quantitative XRD results and optical micrographs are given in Table III.7 and Fig. III.5, respectively. As can be seen in Fig. III.5 (a), 23 wt% of the structure is in the form of martensite bands and austenite accounts for 77 wt%. Like all the bands in Alloys 1 and 2, the martensite bands are parallel to the rolling direction. The martensite has the plate morphology (Fig. III.6) and thinner plates formed inside all of the austenite grains (Fig. III.5 (b)). Moreover, some annealing twins are observed within austenite grains (Fig. III.5 (c)). Since unstable austenite transforms into martensite when cooled, it is expected that the martensite regions are low in Mn and the related EDS results are given in Table III.8 and Table III.9.

Martensite / wt%	Austenite / wt%	Cementite / wt%	R_{wp}	R_{exp}	χ^2
23 ± 1	77 ± 1	0 ± 1	32.4	12.24	7.03

Table III.7 Quantitative XRD analysis result of Alloy 3 after the first anneal by Rietveld refinement method.

Region index	Mn / wt%	Fe / wt%
Martensite 1	7.47 ± 0.27	92.53 ± 0.57
Martensite 2	7.21 ± 0.27	92.79 ± 0.58
Martensite 3	7.77 ± 0.27	92.23 ± 0.58
Average	7.48 ± 0.39	92.52 ± 0.64

Table III.8 EDS overall spectrum results of three martensite regions in Alloy 3 with FE-SEM. Note that the C content is not included in the analysis.

Region index	Mn / wt%	Fe / wt%
Austenite 1	8.60 ± 0.28	91.40 ± 0.58
Austenite 2	8.89 ± 0.28	91.11 ± 0.58
Austenite 3	9.12 ± 0.29	90.88 ± 0.58
Average	8.87 ± 0.38	91.13 ± 0.64

Table III.9 EDS overall spectrum results of three martensite regions in Alloy 3 with FE-SEM. Note that the C content is not included in the analysis. Note that all the austenite regions contain thin plates of martensite.

(a)

(b)

(c)
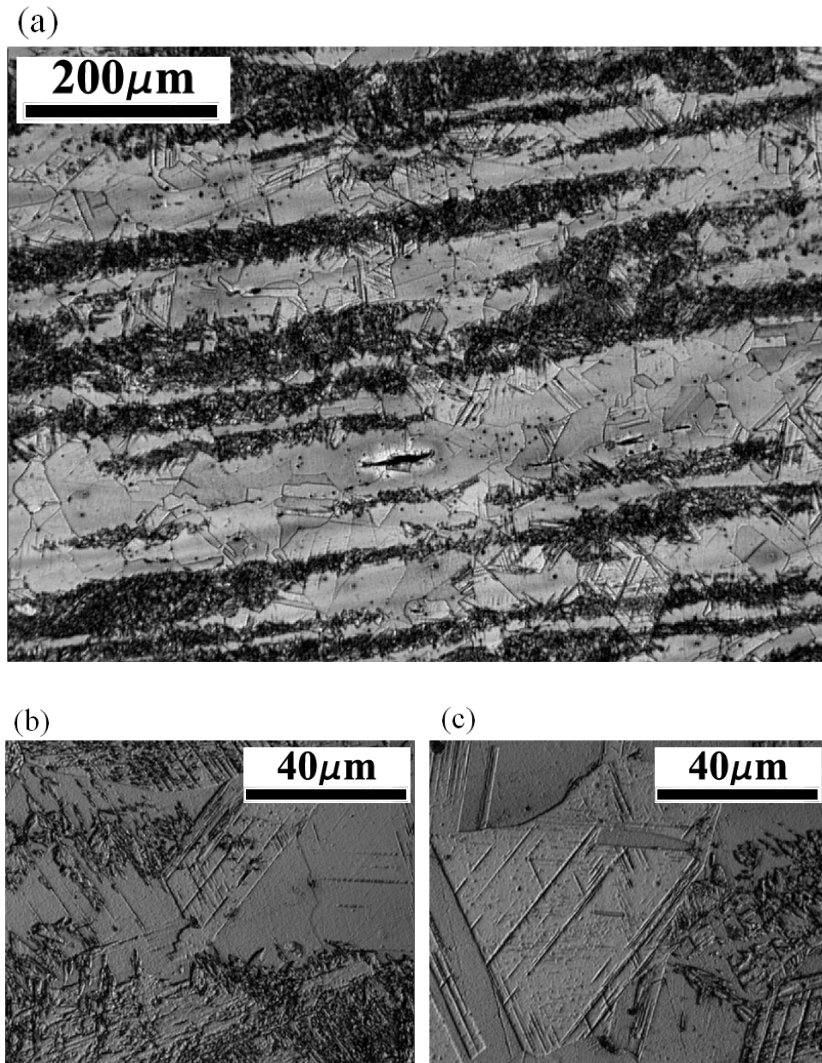
Fig. III.5 Optical micrographs of Alloy 3 after the first anneal (austenitization and quench). The sample is etched with saturated aqueous picric acid and then 1 % nital. (a) The subjected area consists of martensite bands in austenite matrix. Notice that martensite bands are parallel to rolling direction. (b) and (c) Higher magnification images.
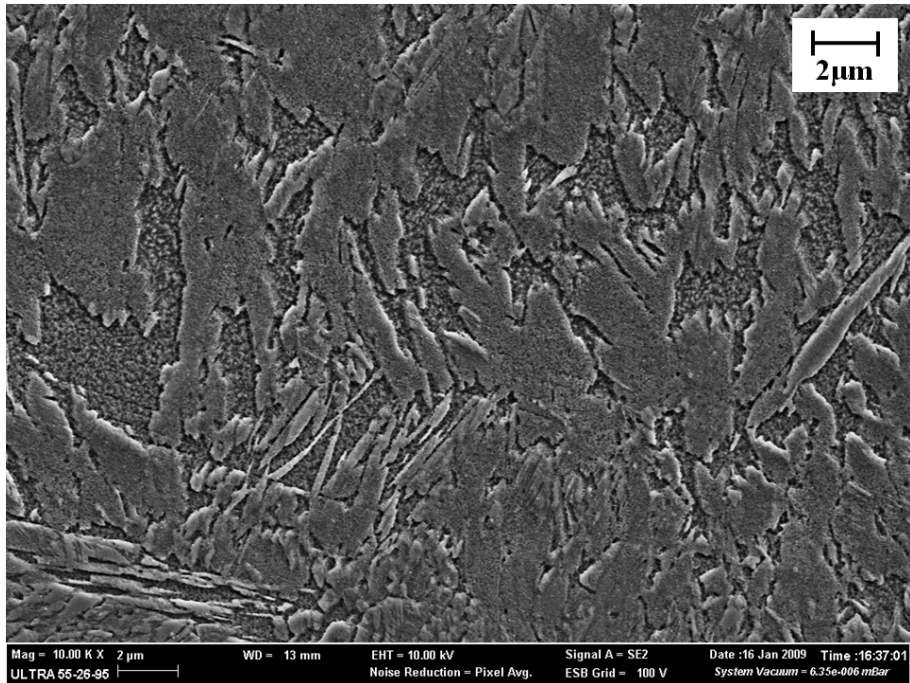
Fig. III.6 An SEM image of plate martensite. The sample is etched with 1 % nital.

As in section III.2, the C content was obtained from XRD and EDS result and the composition of austenite region turned out to be Fe-8.82 ± 0.38 Mn-0.559 ± 0.021 C (wt%). Unlike in the case of Alloy 2, this time, C content was reasonable. The phases of Alloy 3 are the same as alloy 2 and it can be explained in the same way. The high Mn region is retained as austenite and low Mn region transformed into austenite.

The hardness of martensite was HV 354 ± 48 and of austenite, HV 201 ±

15. As in Alloy 2, it should be considered that austenite can contribute to the hardness of martensite since martensite plates are always embedded in austenite. This effect explains the large standard deviation in the hardness of martensite.

III.4. Discussion

To compare the phase fractions in the alloys, the data (Tables III.1, III.4 and III.7) are compared in Fig. III.7. Comparing Alloy 1 and 2, the difference in overall C content is 0.400 wt% and this resulted in 9 wt% increase of austenite. This change caused microstructure of Alloy 2 to have separate austenite phase which can be formed in high Mn region due to slow Mn diffusion and Alloy 1 to have retained austenite in martensite. In addition, comparing Alloy 2 and 3, 2.66 wt% of Mn difference brought 60 wt% increase in austenite.
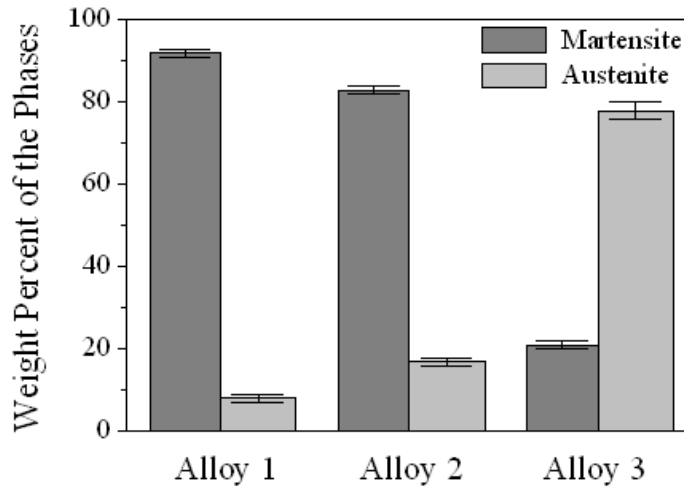
Fig. III.7 The weight percent of phases in the three alloys. The values are from Tables III.1, III.4 and III.7. Cementite is ignored because its values are 0 wt%.

The average composition data are given in Table III.10. Note that C content was not considered for martensite in Alloy 2 and 3. If the region bears low Mn and C, then martensite appears and vice versa. However, it should be mentioned that there was an assumption of constant C content over the alloy for Alloy 1. Actually, the C content depends on Mn content because high Mn content gives rise to low C activity coefficient (Fig. III.8). This implies that high Mn region would result in low C activity, thus gathering more C. It is true for Alloy 1 that the practical values of C content may be different from those shown in Table III.10.

However, austenite in alloy 2 and 3 showed lower C content than overall value. These do not go with high C content in high Mn region and more study is necessary.

Alloy	Mn / wt%	C / wt%	Phase
1	4.33 ± 0.66	0.25	Martensite
1	5.98 ± 0.58	0.25	Martensite
2	4.76 ± 0.49	-	Martensite
2	6.86 ± 0.39	0.250 ± 0.030	Austenite
3	7.48 ± 0.39	-	Martensite
3	8.82 ± 0.38	0.559 ± 0.021	Austenite

Table III.10 EDS results and phase information for the regions of all alloys.
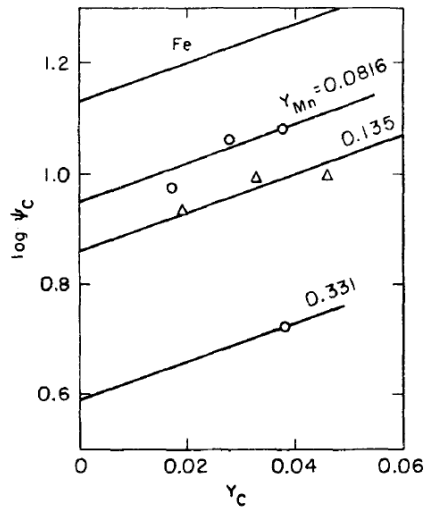
Fig. III.8 Activity coefficient of carbon (ψ_c) in Fe-Mn-C alloys at 850 ℃.

Y_{Mn} and Y_C refers to site fraction of Mn and C (Wada *et al.*, 1972).

IV. Second Anneal – Formation of Cementite Particles

IV.1. FINITE-VOL Calculation

When a cementite particle forms during the second anneal, initial precipitation and growth take place. Since the alloys have Mn, its enrichment occurs simultaneously with the particle coarsening. The driving force of coarsening is α / θ interfacial energy and of enrichment is the free energy difference between paraequilibrium and equilibrium cementite. Here, we assume that driving force of the former is much smaller than that of the latter, and only consider the partitioning of alloying elements. The fact that Mn partitioning slows down cementite coarsening in Fe-Mn-C system also supports the assumption (Björklund *et al.*, 1972, Miyamoto *et al.*, 2007). In this respect, the cementite size is kept constant and the period for the second anneal is decided from the calculation using FINITE-VOL program modified from the original FINITE program (Bhadeshia, 1989).

FINITE deals with partitioning of a given alloying element into cementite. The program is based on a finite difference method. The method for FINITE-VOL program is the same as FINITE program but some of the input variables are different. The parameters for both programs are shown in Table IV.1. In FINITE-VOL, the volume fraction of cementite (V_θ) is obtained to calculate

the half thickness of ferrite (x_α) from the thickness of cementite (x_θ) instead

of getting directly the value of ferrite thickness (Eq. IV.1).

$$2 \cdot x_\alpha : (1 - V_\theta) = x_\theta : V_\theta \qquad \text{(Eq. IV.1)}$$

Moreover, the initial alloying element content in the first ferrite slice in the

finite difference method is given as equilibrium concentration in ferrite. The

initial content in the first cementite slice is given by the mass balance of the

alloying element.

The chosen annealing temperature was 550 ℃ and the equilibrium

concentrations were estimated using MTDATA (Table II.3). The Mn content

in the alloy is from Table II.2. Diffusion coefficient of Mn is in Eq. IV.2

(Weast, 1976).

$$D_{Mn} = D_0 \exp(-\frac{Q}{RT}), \qquad \text{(Eq. IV.2.a)}$$

$$D_0 = 3.5 \times 10^{-5} \ \text{m}^2\text{s}^{-1}, \ Q = 219660 \quad \text{J mol}^{-1} \qquad \text{(Eq. IV.2.b)}$$

where R is universal gas constant, the value of which is 8.3143 J mol^{-1} K^{-1}

and T is temperature in Kelvin. The thickness of cementite was varied from

100 nm to 1000 nm with a 100 nm step. The numbers of cementite slices,

each 10 nm thick, is therefore different for each case.

FINITE	FINITE-VOL
Annealing temperature	Annealing temperature
Equilibrium alloying element content in ferrite	Equilibrium alloying element content in ferrite
Equilibrium alloying element content in cemenite	Equilibrium alloying element content in cemenite
Alloying element content in the alloy	Alloying element content in the alloy
Thickness of cementite	Thickness of cementite
Thickness of ferrite	Volume fraction of cementite
The number of cementite slices	The number of cementite slices
Parameters for diffusion coefficient	Parameters for diffusion coefficient
Initial alloying element content in the first ferrite slice	
Initial alloying element content in the first cementite slice	

Table IV.1 Input parameters of FINITE and FINITE-VOL program. The difference between the two programs are shown in the shaded boxes.

With the FINITE-VOL program, the time for cementite to reach a certain Mn concentration of each phase as well as that of each slice can be obtained. First, the time for the first slice of cementite to reach 30 wt% Mn was calculated (Fig. IV.1). The reason for choosing 30 wt% Mn was that it is enough for austenite to exhibit a TWIP effect if austenite inherits the Mn content directly from cementite.
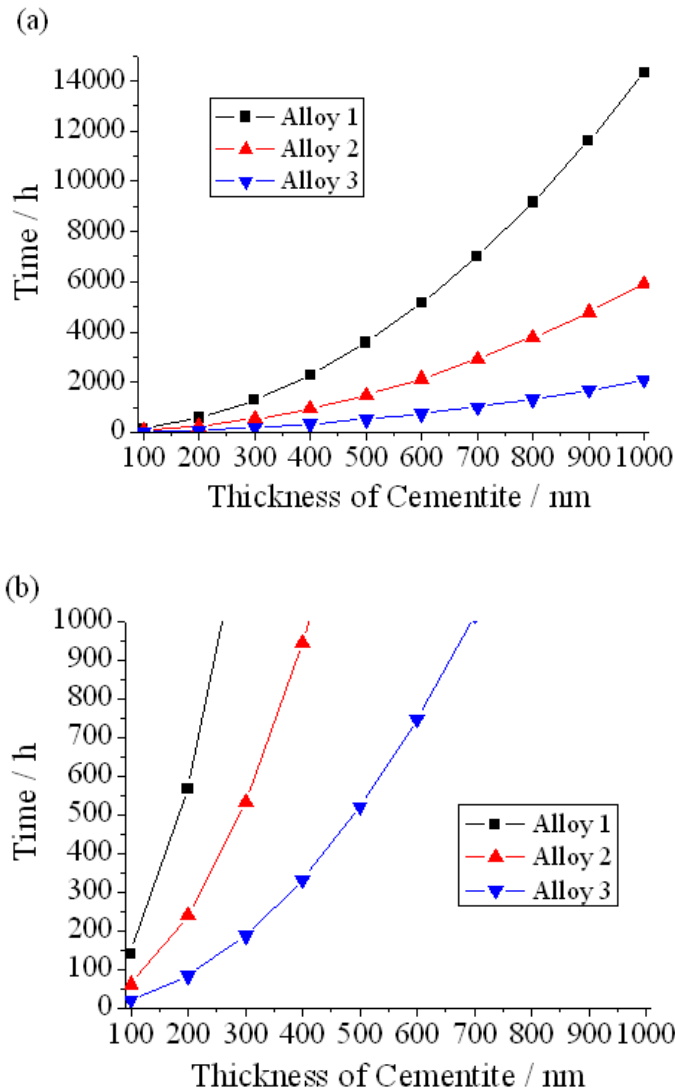
Fig. IV.1 Time for the first slice of cementite to reach 30 wt% as a function of the thickness of cementite. (b) Magnified version of (a) during the first 1000 h.

In Fig. IV.1, the time to reach 30 wt% Mn increases by the power of 2 according to the cementite thickness. For Fe-1.02 Mn-0.61 C-0.016 Si and Fe-

1.96 Mn-0.61 C-0.039 Si (wt %) at 650 ℃, the cementite particle reaches approximately 100-200 nm in 10^4-10^6 s (Miyamoto *et al.*, 2007). Therefore, the thickness of 100-500 nm has been taken into account and three annealing times were decided: 200, 400 and 800 h. Then, the average concentrations were calculated for the selected time in respect to the thickness of cementite (Figs. IV.2-IV.4).

For the Alloy 1, it seems unnecessary to anneal for 200 h because it would not reach more than 30 wt% Mn for cementite larger than 150 nm. For the Alloy 3, 800 h is unnecessary since partitioning may occur rapidly in a shorter time. Therefore, the annealing times were chosen as 400 and 800 h for Alloy 1, 200, 400 and 800 h for Alloy 2, and 200 h and 400h for Alloy 3.
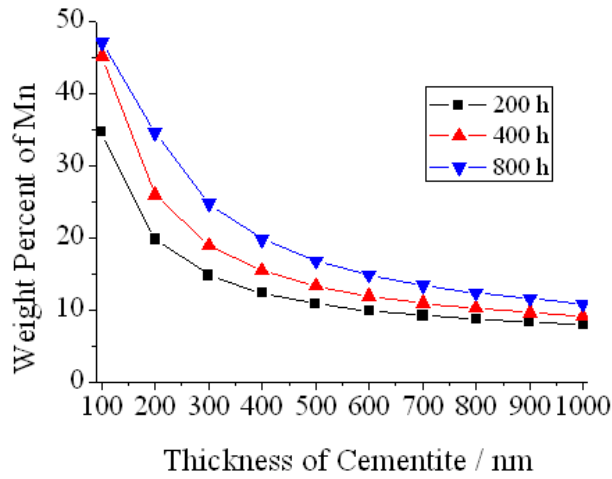
Fig. IV.2 Average Mn concentration of cementite in Alloy 1 as a function of cementite thickness.
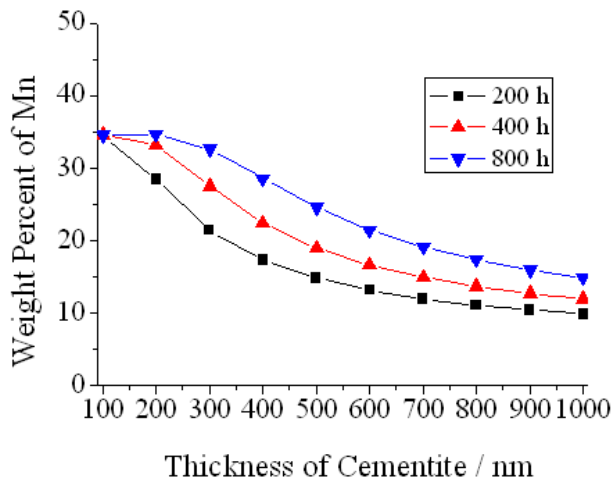
Fig. IV.3 Average Mn concentration of cementite in Alloy 2 as a function of cementite thickness.
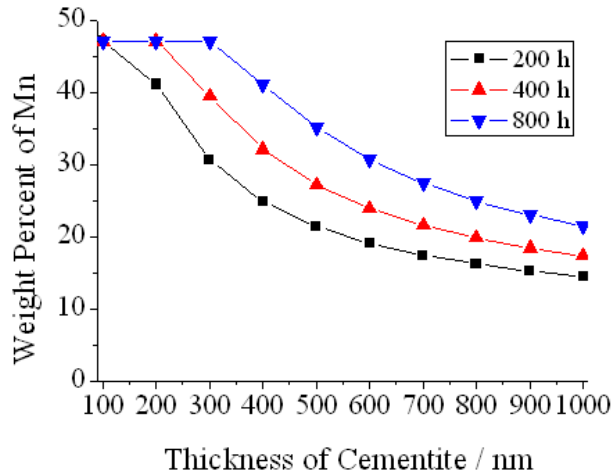
Fig. IV.4 Average Mn concentration of cementite in Alloy 3 as a function of cementite thickness.

IV.2. Alloy 1

Samples of Alloy 1 were annealed for 400 and 800 h and designated 1-400h and 1-800h respectively. The morphologies of 1-400h and 1-800h were similar when observed using OM and SEM. Both showed dark-contrast bands (Fig. IV.5). All regions contained spherical cementite particles (Fig. IV.6). The particles sizes varied from tens of nanometers to 1 μm. Those at grain boundaries were coarser. Ferrite matrix was different for different contrast region. Ferrite in light-contrast region showed normal morphologies with

grain boundaries while in dark-contrast region, dents were seen instead of grain boundaries.
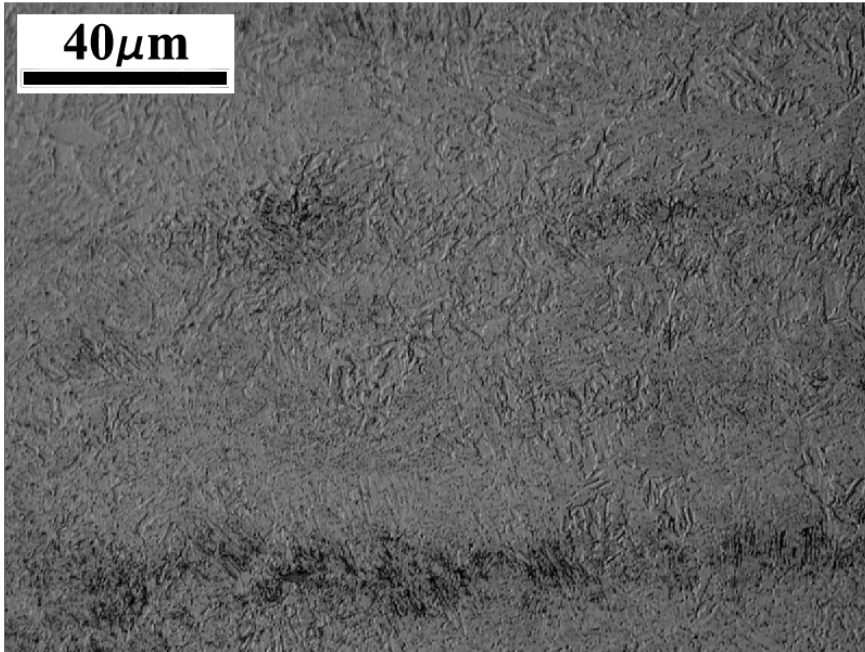
Fig. IV.5 An optical micrograph of 1-400h after the second anneal (at 550 ℃ for 200 h and air cooled). The sample is etched with 1 % nital. Notice the bands of dark contrast parallel to the rolling direction.

(a)

(b)
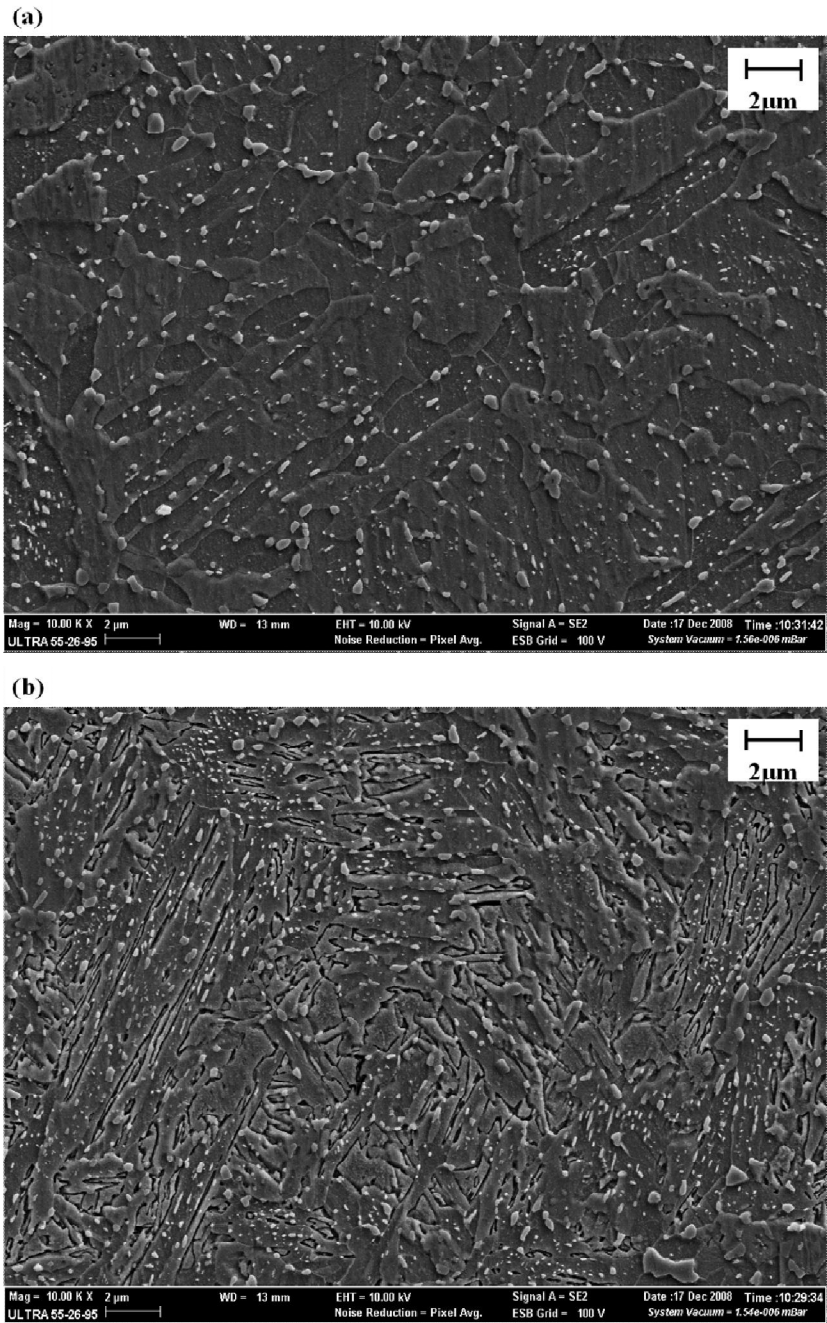
Fig. IV.6 FE-SEM images of 1-400h. (a) The light-contrast region and (b) the dark-contrast region in Fig. IV.5.

The phase fractions obtained by XRD analysis are shown in Table IV.2. The result of 1 wt% of cementite is unreasonable according to the micrographs. Hence, the pixels which are occupied by cementite are counted, and the results are shown in Table IV.3. The obtained value is larger than the calculated equilibrium value, 3.6 vol.%. The cementite vol. % of light and dark-contrast regions were similar. However, the hardness was somewhat different between those regions (Table IV.4). This can be from the matrix morphology difference or cementite size difference. In addition, there was a softening effect: samples tempered for longer periods showed lower hardness values in all regions, probably due to microstructural coarsening as seen in Fig. IV.7. Austenite-start and finish temperatures acquired from Fig. IV.7 were listed in Table IV.5. The austenite transformation is delayed for 1-800h because it is expected to have smaller number of nucleation sites than 1-400h due to coarsening.

Alloy	Ferrite / wt%	Austenite / wt%	Cementite / wt%	R_{wp}	R_{exp}	χ^2
1-400h	99 ± 1	0 ± 1	1 ± 1	22.5	13.98	2.6
1-800h	99 ± 1	0 ± 1	1 ± 1	24.8	14.33	2.99

Table IV.2 Quantitative XRD analysis results for Alloy 1 after the second anneal, using the Rietveld refinement method.

Alloy	Light-contrast region / vol. %	Dark-contrast region / vol. %
1-400h	7 ± 1	6 ± 1
1-800h	6 ± 1	5 ± 1

Table IV.3 The cementite vol. % of Alloy 1 after the second anneal obtained by pixel counting method.

Alloy	Light-contrast region / HV	Dark-contrast region / HV
1-400h	206 ± 5	266 ± 15
1-800h	196 ± 4	258 ± 18

Table IV.4 The Vickers hardness of different contrast regions of Alloy 1 after the second anneal. The load was 300 g and dwell time, 10 s.
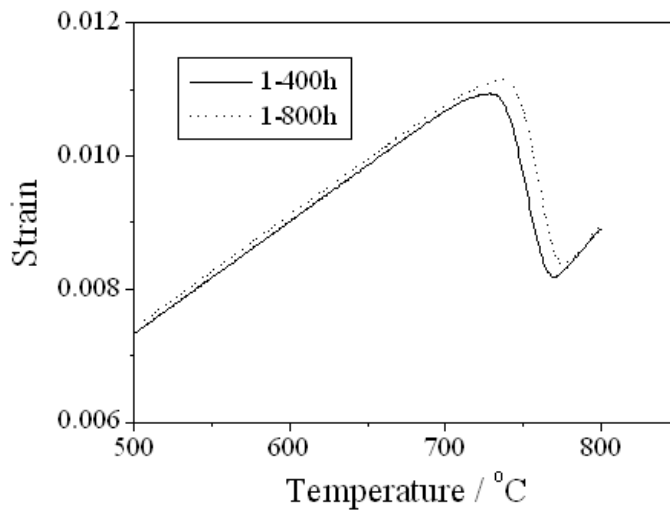
Fig. IV.7 Dilatation curve during heating of Alloy 1. The decrease of strain between 700-800℃ is due to austenitization. The heating rate was 5 ℃ s^{-1}.

Alloy	Austenite-start temperature / ℃	Austenite-finish temperature / ℃
1-400h	715	770
1-800h	719	775

Table IV.5 Austenite-start and finish temperatures of Alloy 1 obtained from the data in Fig. IV.7. The temperatures were acquired by offset method (Yang and Bhadeshia, 2007).

The Mn concentration of cementite is given in Table IV.6 and the TEM images where the EDS data were obtained are shown in Figs. IV.8 and IV.9. The increase of Mn concentration of 1-800h shows that partitioning was incomplete after 400 h of tempering. However, there were particles in 1-400h that reach as high as 47 wt% Mn and those in 1-800h, as low as 29 wt%. The large standard deviation implies that the Mn content is somewhat different for each cementite particle and some of them could already reach near the equilibrium value in short time. Given the equilibrium concentration, 47.1 wt%, the majority of the cementite in 1-800h had reached the equilibrium.

Alloy	Mn content of θ/ wt%	Mn content of θ considering C / wt%	Mn content of α / wt%
1-400h	33.9 ± 9.8	31.6 ± 9.1	3.8 ± 0.5
1-800h	45.8 ± 7.7	42.7 ± 7.2	3.0 ± 0.2

Table IV.6 Mn content of cementite (θ) and ferrite (α) in Alloy 1 after the second anneal. The values in the third column were calculated by assuming 25 at% C in cementite. Mn content of ferrite was obtained assuming zero carbon. The calculated equilibrium concentration of Mn in ferrite is 3.1 wt%.

Fig. IV.8 Bright field image of 1-400h indicating positions where the Mn content was determined using EDS. Ferrite is indicated as α and cemenite, θ.
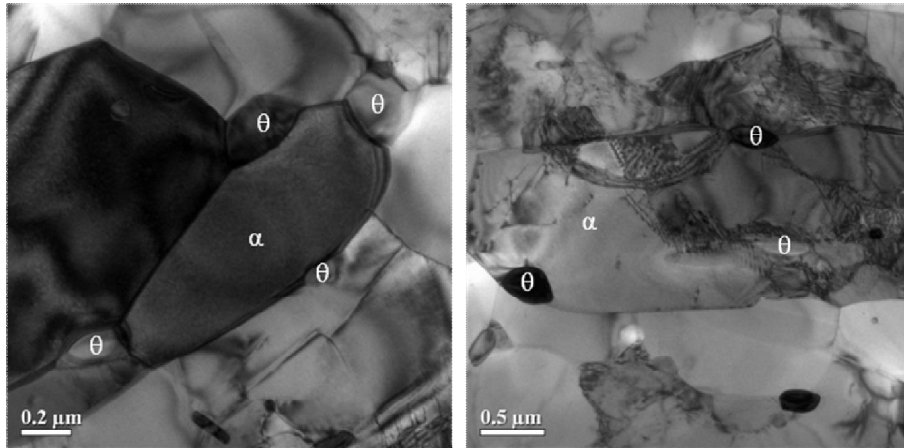
Fig. IV.9 Bright field image of 1-800h indicating positions where the Mn content was determined using EDS. Ferrite is indicated as α and cemenite, θ.

Some of α/θ interfaces in the regions in Figs. IV.8 and IV.9 were under the orientation relationship analysis (Figs. IV.10 and IV.11). Among six interfaces, four showed a known orientation relationship such as Bagaryatski with the adjacent ferrite. When cementite is surrounded by more than one ferrite grain, it may be that it relates to only one of the ferrite grains. Besides, one ferrite grain can have orientation relationship with more than one cementite particles (Fig. IV.11 (b)).

(a)

0.2 μm

0.2 μm

$(12\bar{1})_{\alpha}$

$(020)_{\theta}$

$(\bar{1}10)_{\alpha}$
$(10\bar{3})_{\theta}$

$\langle 113 \rangle_{\alpha} \ // \ \langle 301 \rangle_{\theta}$

Ferrite
Cementite
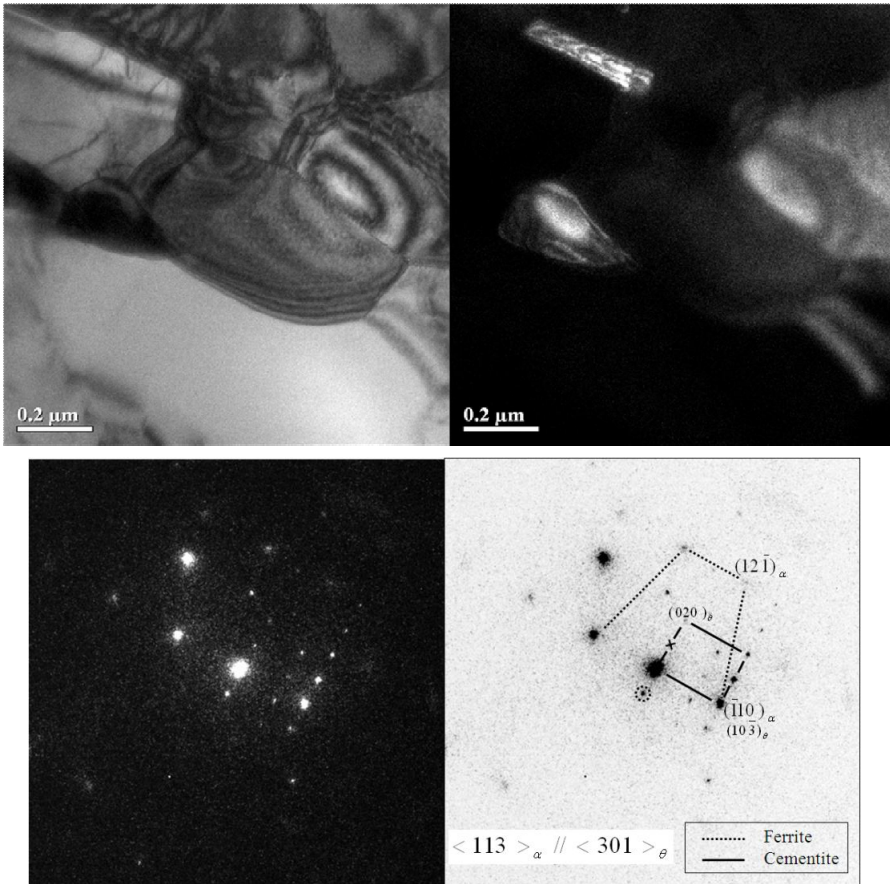
(b)
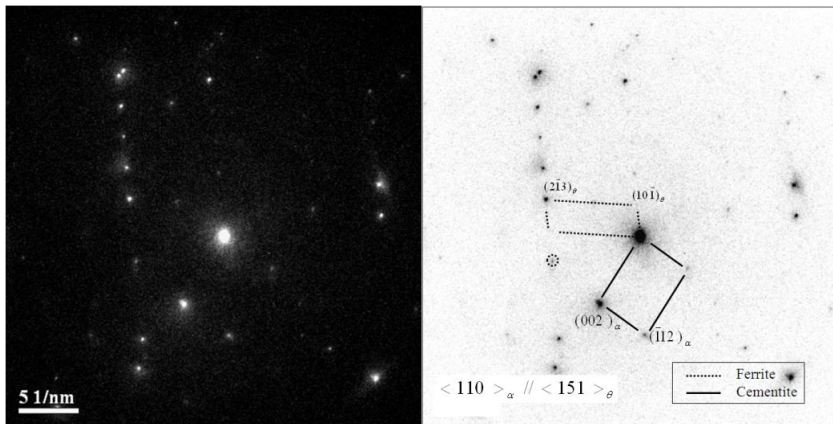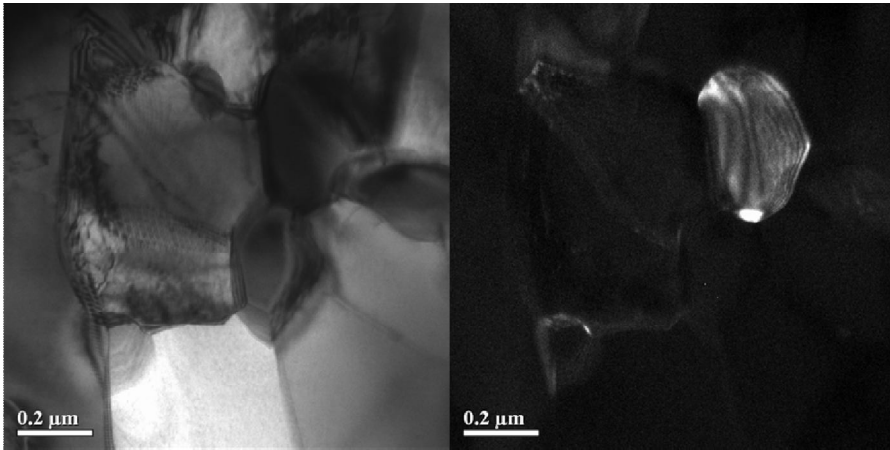
Fig. IV.10   Bright field, dark field images and diffraction pattern of the two regions of 1-400h in Fig. IV.8. Neither (a) nor (b) shows known orientation relationships. The selected reflections for the dark field image are given as circle in the diffraction pattern.

(a)

$[011]_\alpha // [0\bar{2}1]_\theta$

Ferrite
Cementite

$(200)_\alpha$
$(112)_\theta$
$(0\bar{1}1)_\alpha$
$(100)_\theta$

(b)

(i)

0.5 μm

(i)

(ii)

0.5 μm

0.5 μm

(i)

$(211)_\alpha$

$(00\bar{2})_\theta$

$(011)_\alpha$

$(0\bar{2}\bar{2})_\theta$

$[0\bar{1}1]_\alpha \, // [100]_\theta$

······· Ferrite
—— Cementite
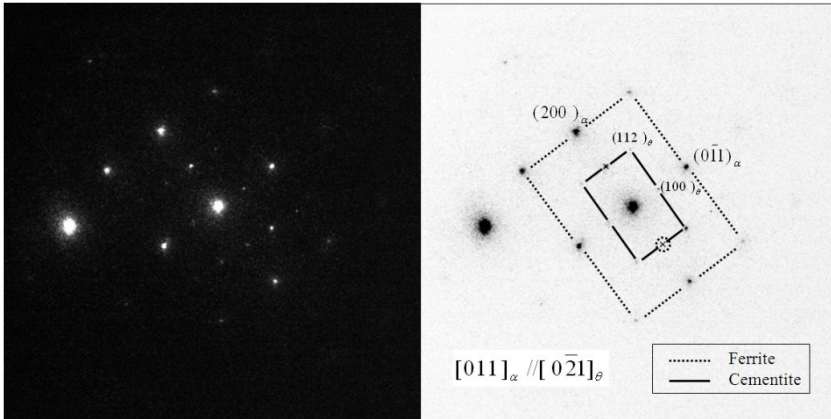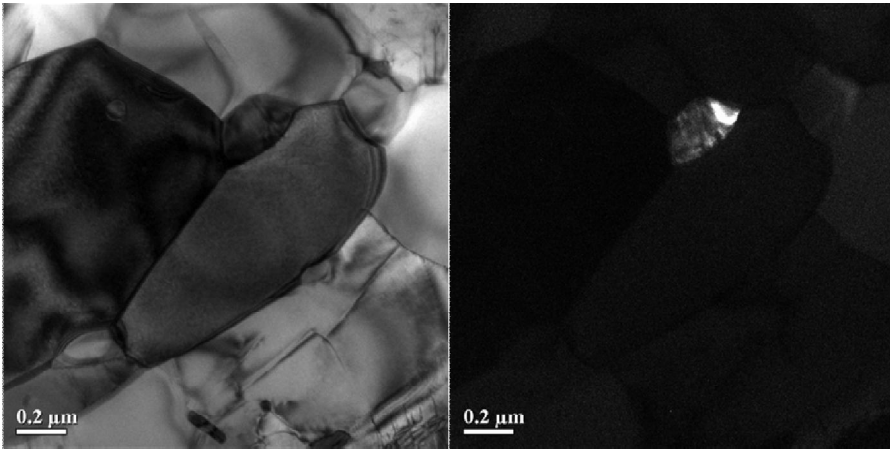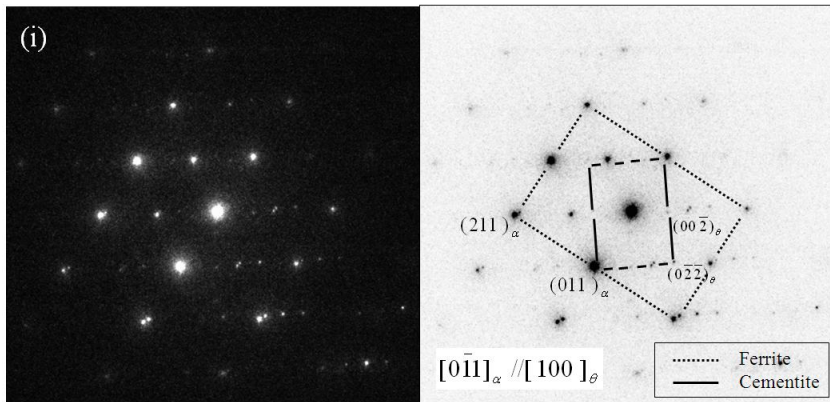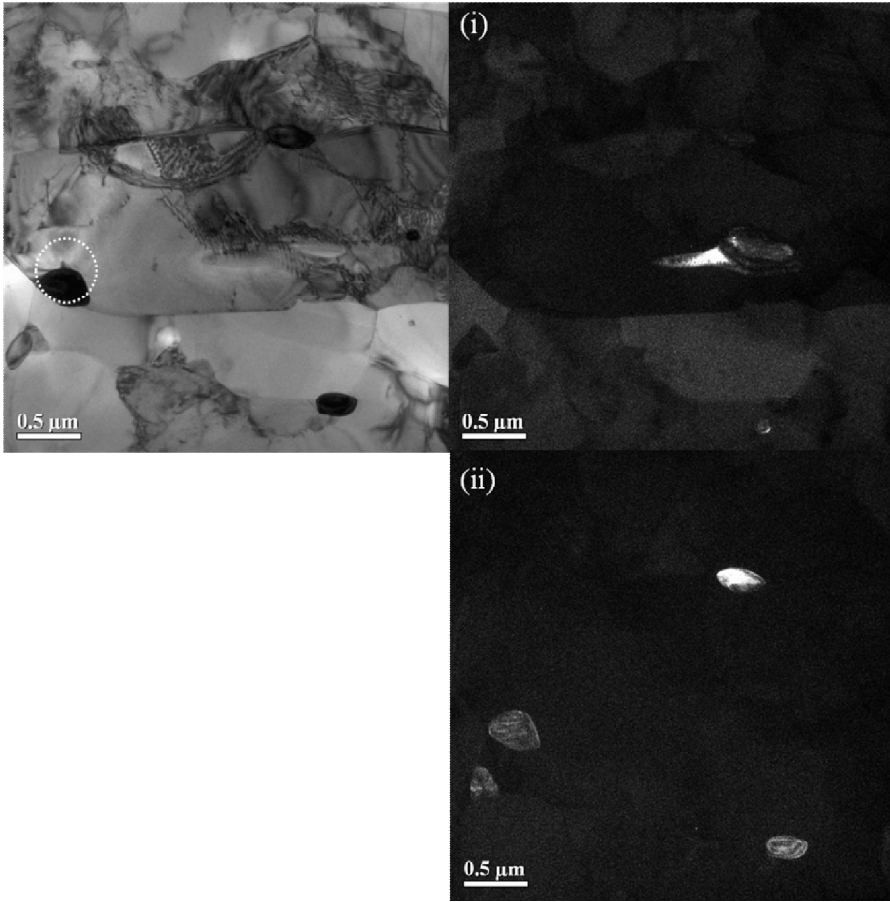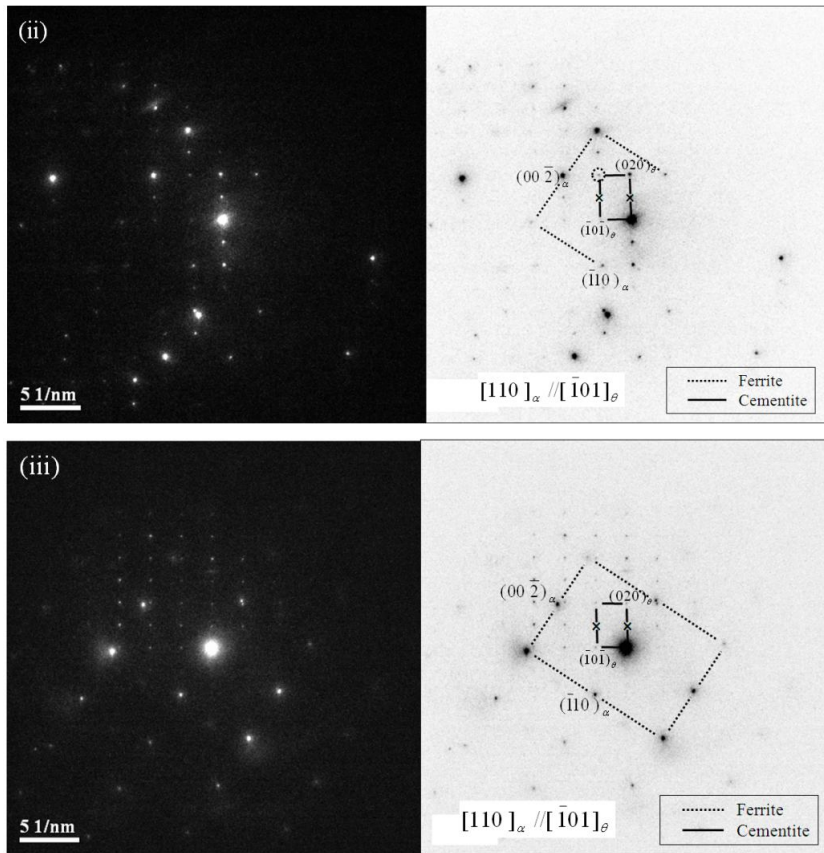
Fig. IV.11 Bright field, dark field images and diffraction patterns of the two regions of 1-800h in Fig. IV.9. All the diffraction patterns are showing Bagaryatski orientation relationship. In (b), the diffraction pattern and dark field image pairs have the same denotation, (i) and (iii). For (b, iii), the selected area aperture was placed on the circled interface shown in the bright field image. The reflections for the dark field image are given as circle in the diffraction pattern.

IV.3. Alloy 2

Samples of Alloy 2 heat-treated for 200 h, 400 h and 800 h are designated as 2-200h, 2-400h and 2-800h, respectively. Their morphologies of all the samples were similar and representative micrographs are shown in Fig. IV.12-IV.13.
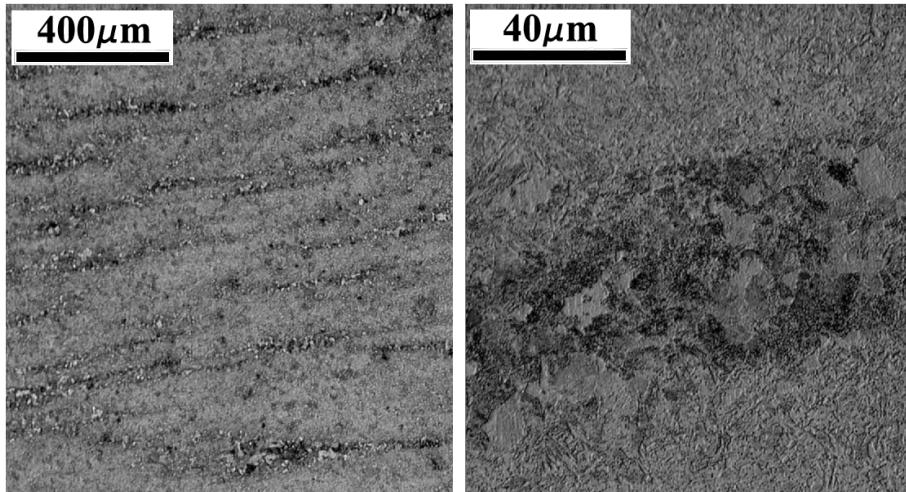
Fig. IV.12 Optical micrographs of 2-400h. There are spherical cementite particles in ferrite. The banded regions consist of pearlite and ferrite.

(a)

(b)
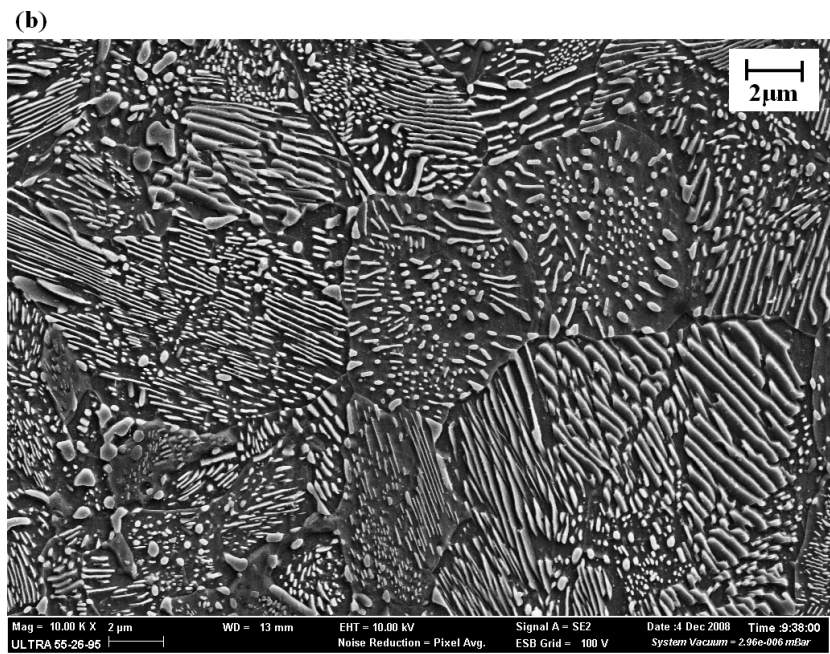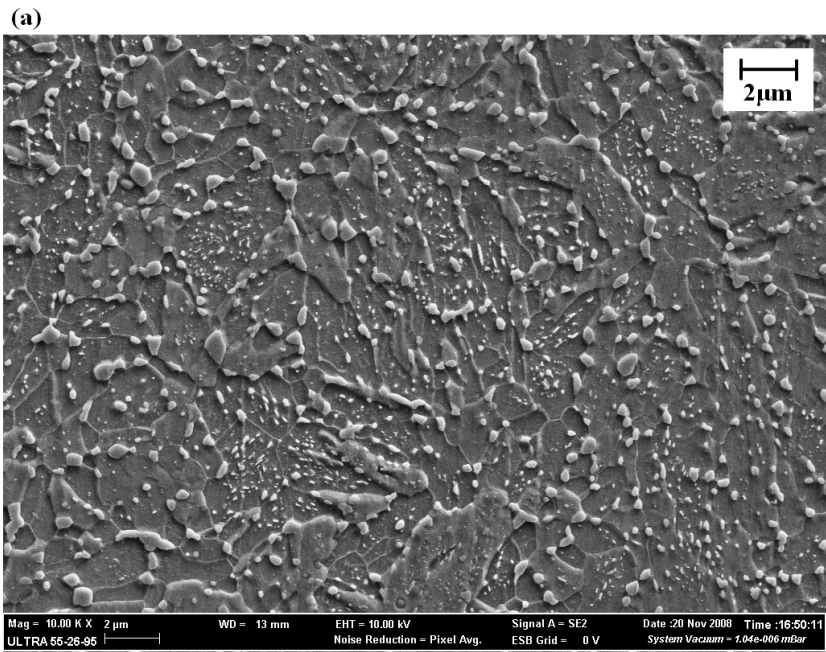
Fig. IV.13 FE-SEM images of 2-400h. (a) The matrix region and (b) the banded region in Fig. IV.12.

Alloy 2 consists of two kinds of areas identified by contrast difference (Fig. IV.12). The first has spherical cementite particles in a ferrite matrix (Fig. IV.13(a)), originated from the tempering of martensite (Fig. III.4). Like Alloy 1, particles located at grain boundaries are coarser. The other distinct region has a pearlitic structure, caused by transformation of austenite region obtained after the first anneal. This austenite was stable enough to be retained after the first heat treatment but the second anneal is for a long period and have the austenite is able to decompose into pearlite. Some of the pearlite colonies are divergent and spherodized.

The XRD refinement and pixel counting method shows that the amount of cementite for each alloy is approximately the same (Tables IV.7 and IV.8). Comparing with the equilibrium value, 9.7 vol. %, XRD results are much lower and pixel counting results are higher.

Alloy	Ferrite / wt%	Austenite / wt%	Cementite / wt%	R_{wp}	R_{exp}	χ^2
2-200h	98 ± 2	0 ± 0	2 ± 1	26.9	13.74	3.83
2-400h	98 ± 2	0 ± 0	2 ± 1	26.4	14.20	3.45
2-800h	98 ± 2	0 ± 0	2 ± 1	27.4	14.38	3.65

Table IV.7 Quantitative XRD analysis results of Alloy 2 after the second anneal, using the Rietveld refinement method.

Alloy	Spherical cementite region / vol. %	Pearlitic cementite region / vol. %
2-200h	13 ± 1	30 ± 6
2-400h	12 ± 2	33 ± 6
2-800h	15 ± 2	26 ± 2

Table IV.8 Cementite vol. % of Alloy 2 after the second anneal obtained by pixel counting method.

Shown in Table IV.9, pearlitic regions show a little higher hardness than spherical cementite regions. It is thought that since pearlitic regions have larger fraction of cementite and the α/θ interface area would be also greater in pearlite regions. Besides, the spherical cementite regions went through softening and that of the pearlitic regions show almost no differences. Still, there was the delay of austenitization for longer annealed alloys (Fig. IV.14, Table IV.10) and the cementite particles seem to have experienced a small degree of coarsening and spherodizing.

Alloy	Spherical cementite region / HV	Pearlitic cementite region / HV
2-200h	235 ± 3	247 ± 10
2-400h	228 ± 4	254 ± 15
2-800h	221 ± 3	247 ± 10

Table IV.9 Vickers hardness of different contrast regions of Alloy 2 after the second anneal. The load was 300 g and dwell time, 10 s.
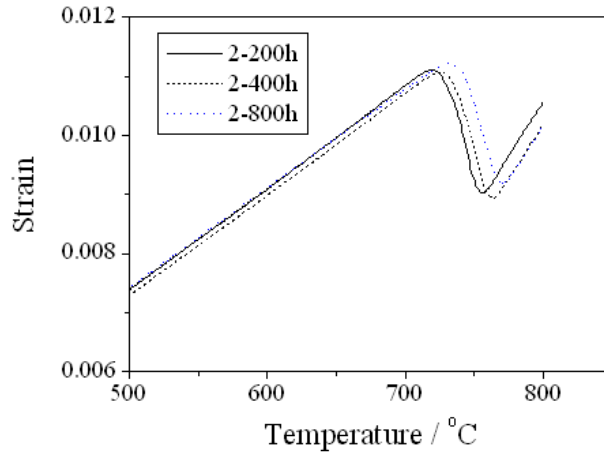
Fig. IV.14 Dilatation curve during heating of Alloy 2. The decrease of strain between 700-800°C is due to the austenitization. The heating rate was 5 °C s^{-1}.

Alloy	Austenite-start temperature / °C	Austenite-finish temperature / °C
2-200h	722	755
2-400h	727	764
2-800h	730	770

Table IV.10 Austenite-start and finish temperatures of Alloy 2 obtained from the data in Fig. IV.14. The temperatures are acquired by offset method (Yang and Bhadeshia, 2007).

The Mn concentrations of cementite in "spherodite" and in pearlite are shown in Tables IV.11 and IV.12, respectively and the regions analyzed are given in Figs. IV.15 and IV.17. The concentrations measured are still less than expected from equilibrium, 34.8 wt%. However, the spherical cementite

particles appear to have reached a steady concentration at 200 h. On the other hand, the pearlitic cementite particles continued to enrich even up to 800 h of annealing.

Alloy	Mn content of θ/ wt%	Mn content of θ considering C / wt%	Mn content of α / wt%
2-200h	30.2 ± 8.6	28.1 ± 8.1	2.4 ± 0.6
2-400h	32.4 ± 8.1	29.1 ± 7.6	2.4 ± 0.5
2-800h	29.0 ± 8.2	27.1 ± 7.7	2.1 ± 0.3

Table IV.11 Mn content of cementite (θ) and ferrite (α) in spherodite regions of Alloy 2 after the second anneal. The values in the third column were calculated by assuming 25 at% C in cementite. The Mn content of ferrite is obtained assuming zero carbon. The calculated equilibrium concentration of Mn in ferrite is 1.7 wt%.

Alloy	Mn content of θ / wt%	Mn content of θ considering C / wt%	Mn content of α / wt%
2-200h	25.1 ± 8.0	23.4 ± 7.4	2.8 ± 1.0
2-400h	28.8 ± 9.2	26.9 ± 8.6	1.7 ± 0.5
2-800h	31.4 ± 4.2	29.3 ± 3.9	1.9 ± 0.3

Table IV.12 Mn content of cementite (θ) and ferrite (α) in pearlitic regions of Alloy 2 after the second anneal. The values in the third column are calculated by assuming 25 at% C in cementite. The Mn content of ferrite is obtained assuming zero carbon. The calculated equilibrium concentration of Mn in ferrite is 1.7 wt%.
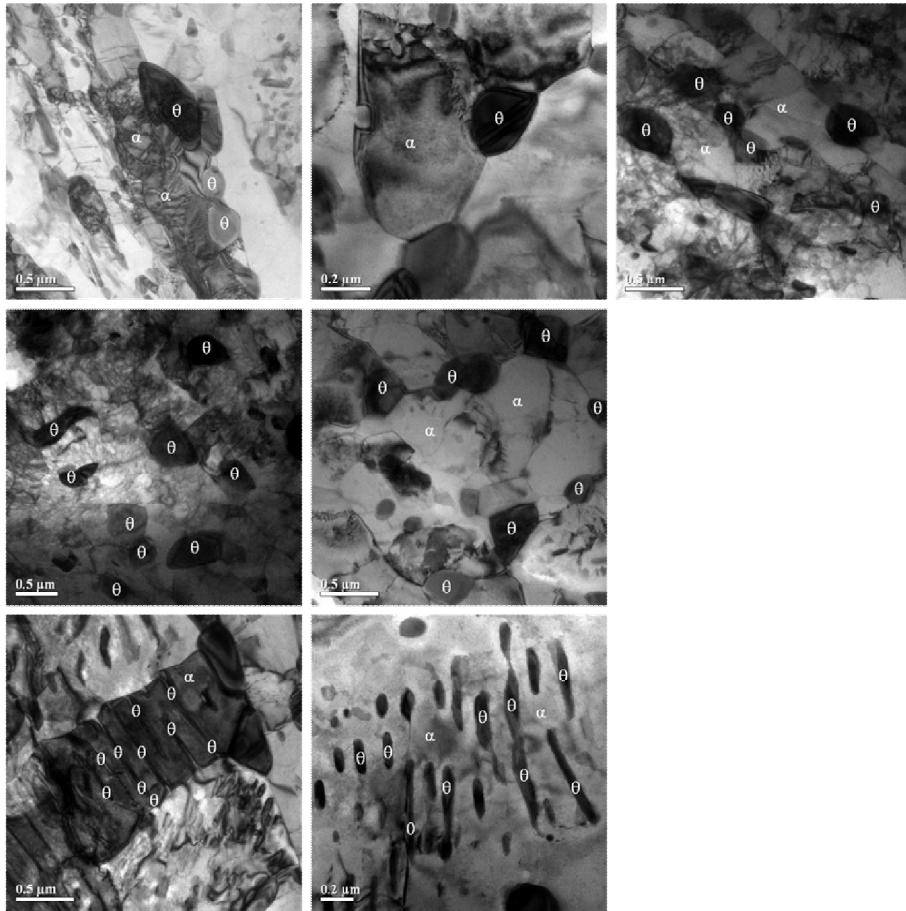
Fig. IV.15 Bright field image of 2-200h indicating positions where the Mn content was determined using EDS. Ferrite is indicated as α and cemenite, θ.
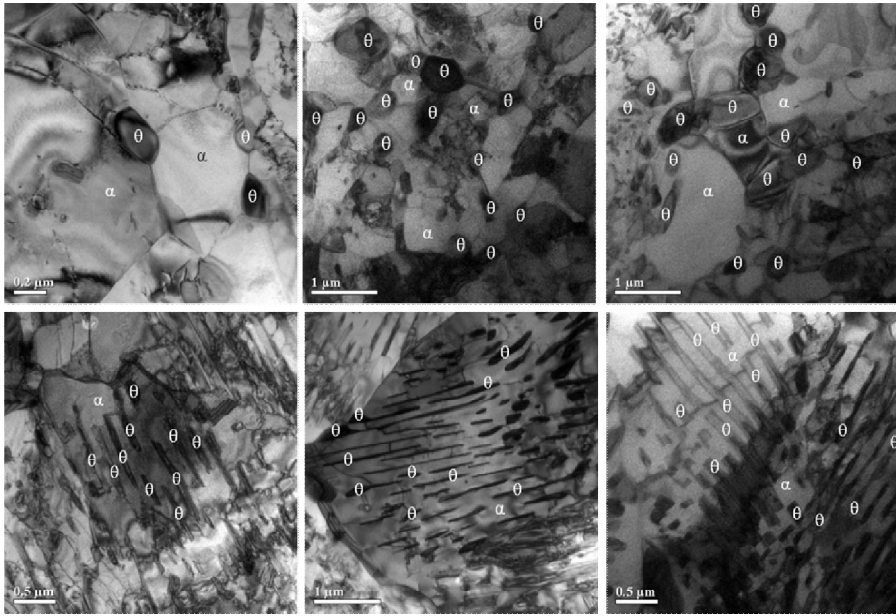
Fig. IV.16 Bright field images of 2-400h indicating positions where the Mn content was determined using EDS. Ferrite is indicated as α and cemenite, θ.
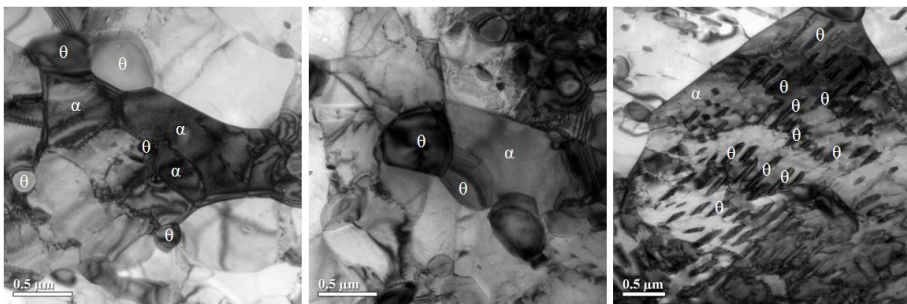
Fig. IV.17 Bright field images of 2-800h indicating positions where the Mn content was determined using EDS. Ferrite is indicated as α and cemenite, θ.

Results of orientation analysis are given in Figs. IV.18 - IV.20. While it is likely that pearlitic cementite which is in contact with ferrite may exhibit a rational orientation relationship, it was hard to find a ferrite grain similarly related to a spherical cementite particle because the structure evolves from the tempering of martensite. For Alloy 2, both spherical cementite particles and pearlitic ones sometimes showed Bagaryatski or Isaichev orientation relationship with the ferrite. It should be noted that Isaichev is close to Bagaryatski. Still, there was certain interface (Fig. IV.20 (c)) which is better corresponds to Isaichev. Although there was no orientation relationship in some structures, it is shown that some reciprocal lattice vectors of the cementite are parallel to those of the ferrite (Figs. IV.18(a) and IV.19(b)).

(a)
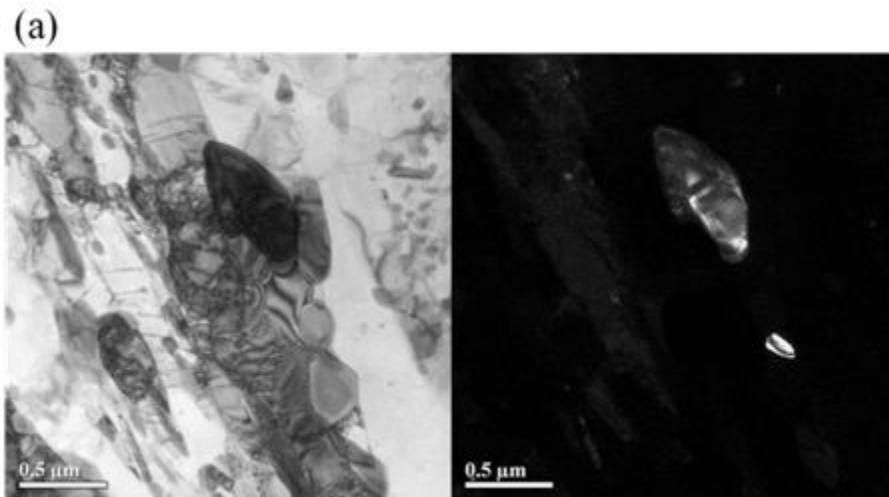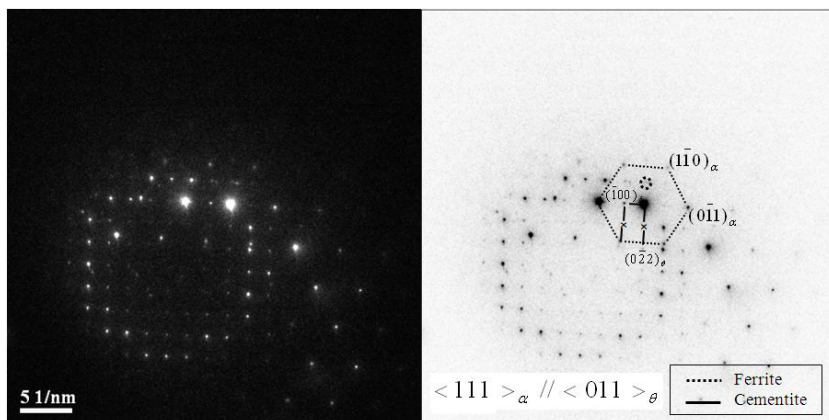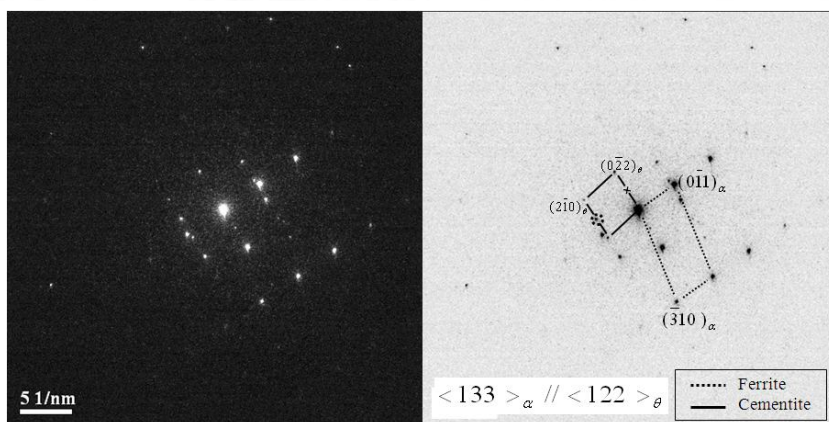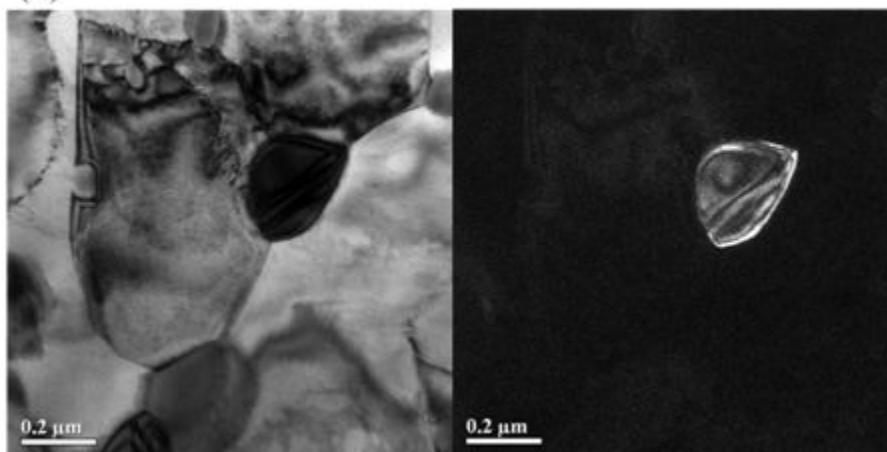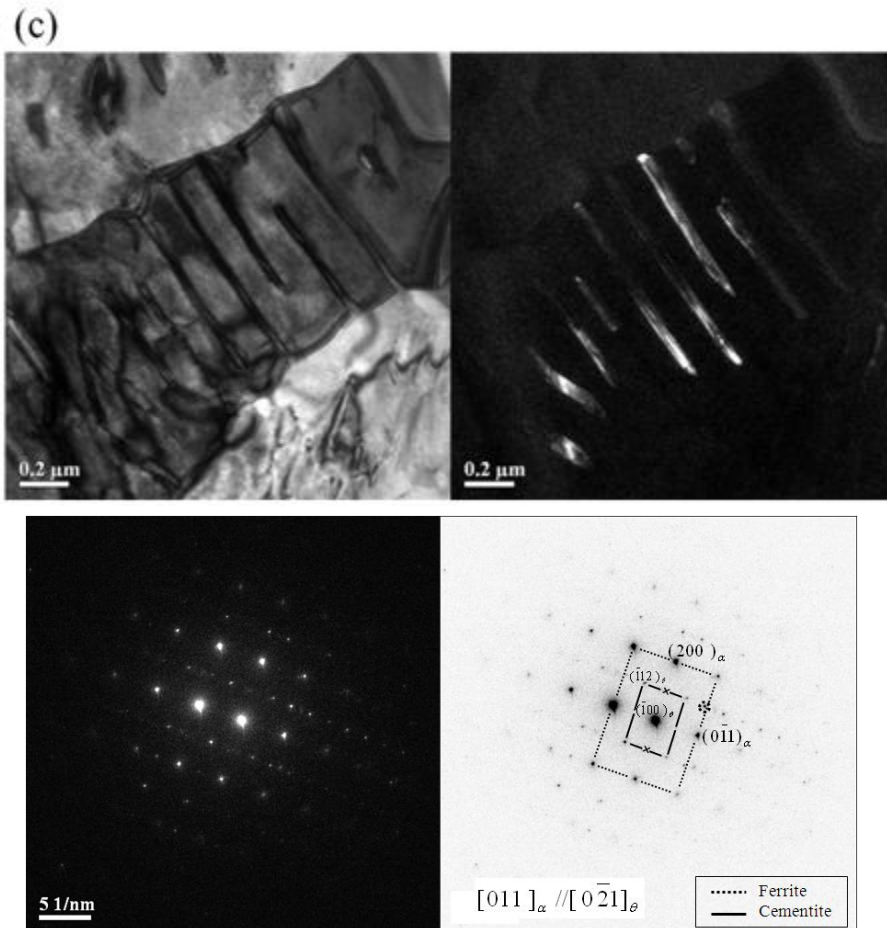
Fig. IV.18 Bright field, dark field images and diffraction patterns of the three regions of 2-200h in Fig. IV.15. Neither (a) nor (b) exhibits known orientation relationships. Only (c) shows Bagaryatski orientation relationship. The reflections for dark field images are given as circles in the diffraction patterns.

(a)

Ferrite 2

Ferrite 1

0.2 μm

0.2 μm

Cementite

$(1\bar{1}\bar{2})_\theta$

$(01\bar{2})_\theta$

5 1/nm

Ferrite ....
Cementite ——•

$< 310 >_{\alpha 1} \; // \; < 311 >_{\alpha 2} \; // \; < \overline{4}\overline{2}\overline{1} >_\theta$

Ferrite 1

$(002)_\alpha$

$(130)_\alpha$

5 1/nm

Ferrite 2

$(\bar{1}21)_\alpha$

$(01\bar{1})_\alpha$

5 1/nm
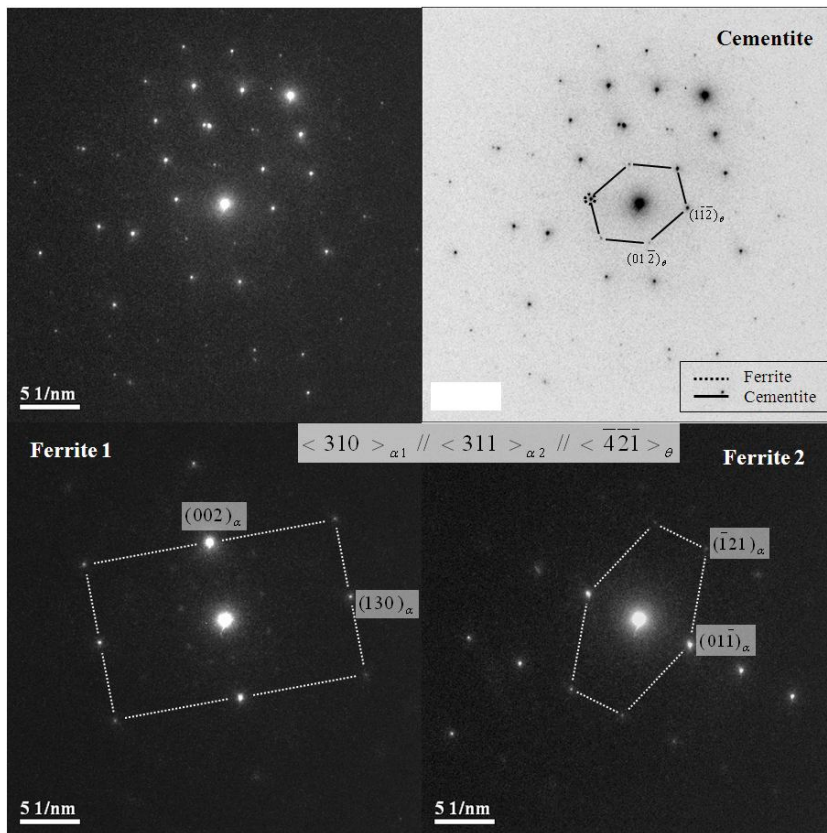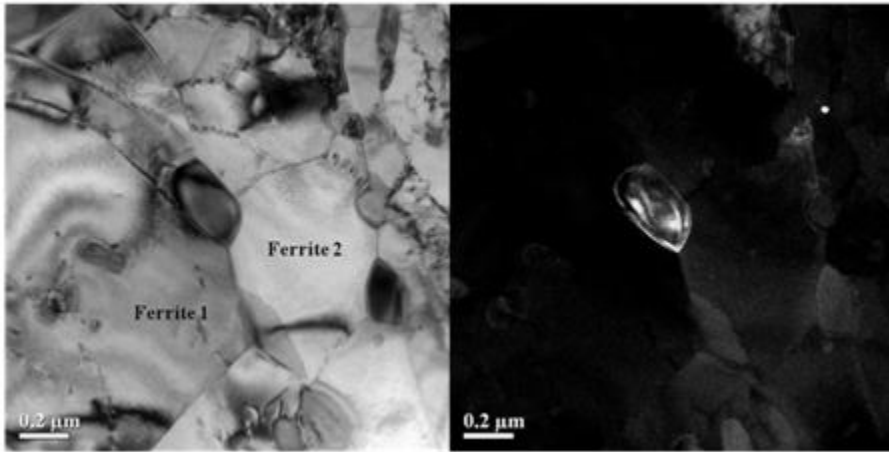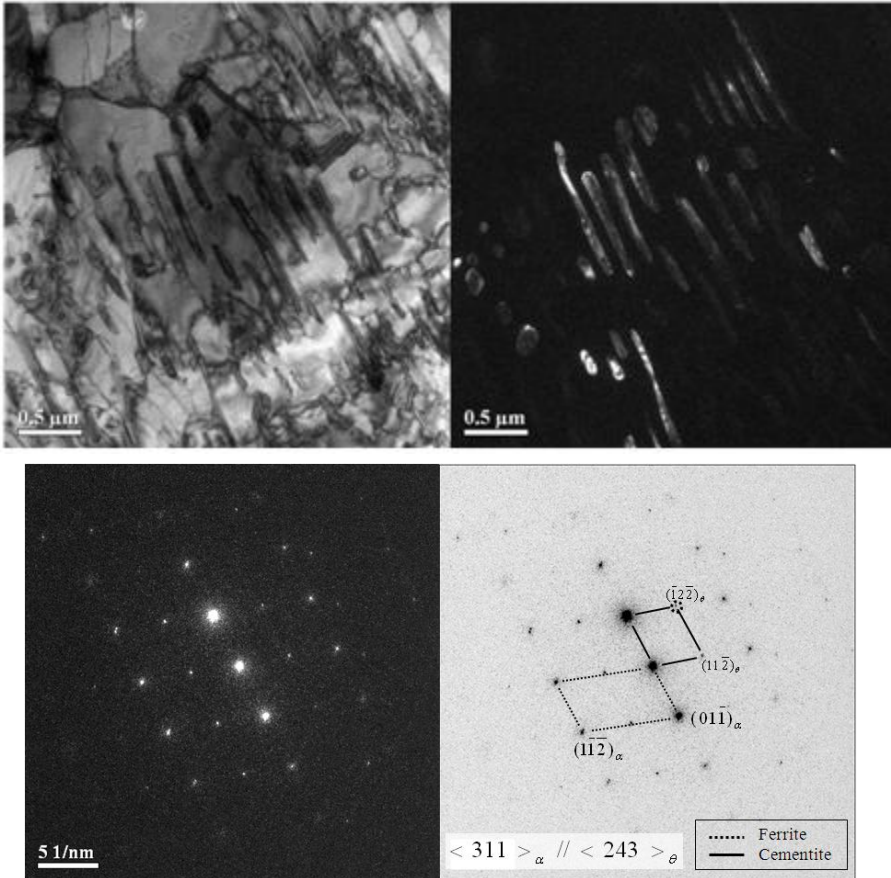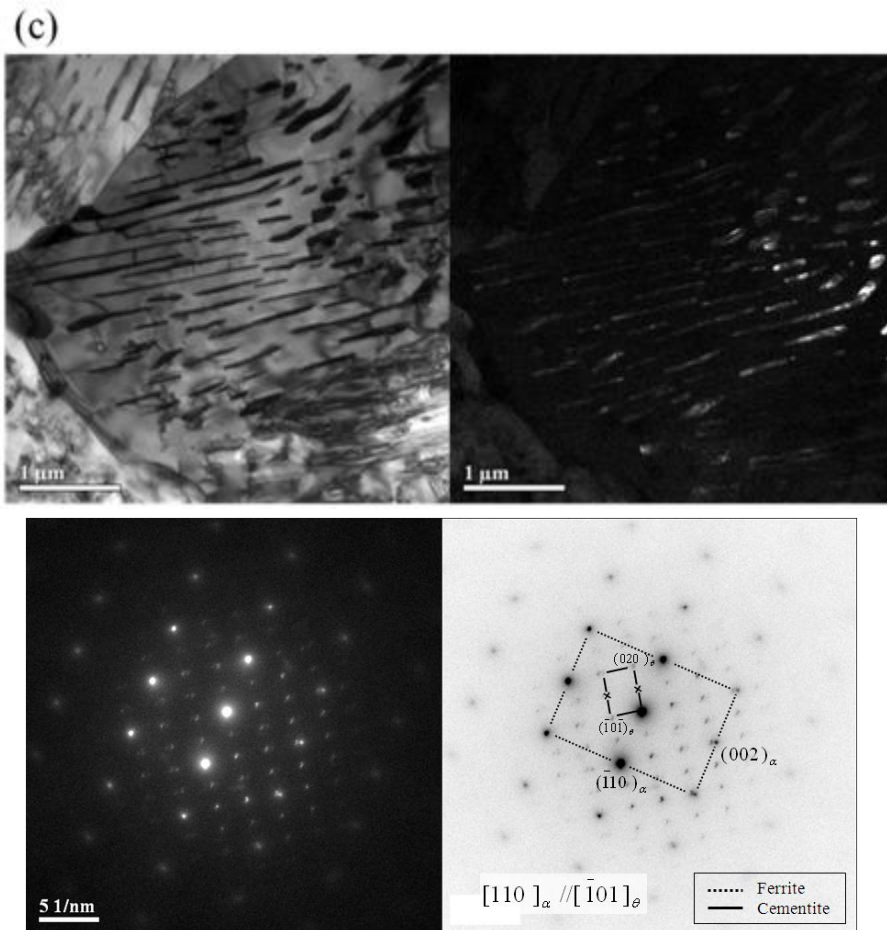
Fig. IV.19 Bright field, dark field images and diffraction patterns of the three regions of 2-400h in Fig. IV.16. (a) and (b) do not show any known orientation relationship. Only (c) shows Bagaryatski orientation relationship. In (a), the diffraction pattern of a cementite and two ferrite grains which are in contact with the cementite were taken separately without tilting. The two grains are marked in the bright field image. The reflections for the dark field images are given as circle in the diffraction patterns.

(a)

$[111]_\alpha // [0\bar{1}2]_\theta$

$(\bar{1}10)_\alpha$

$(01\bar{1})_\alpha$

$(100)_\theta$

$(121)_\theta$

Ferrite
Cementite
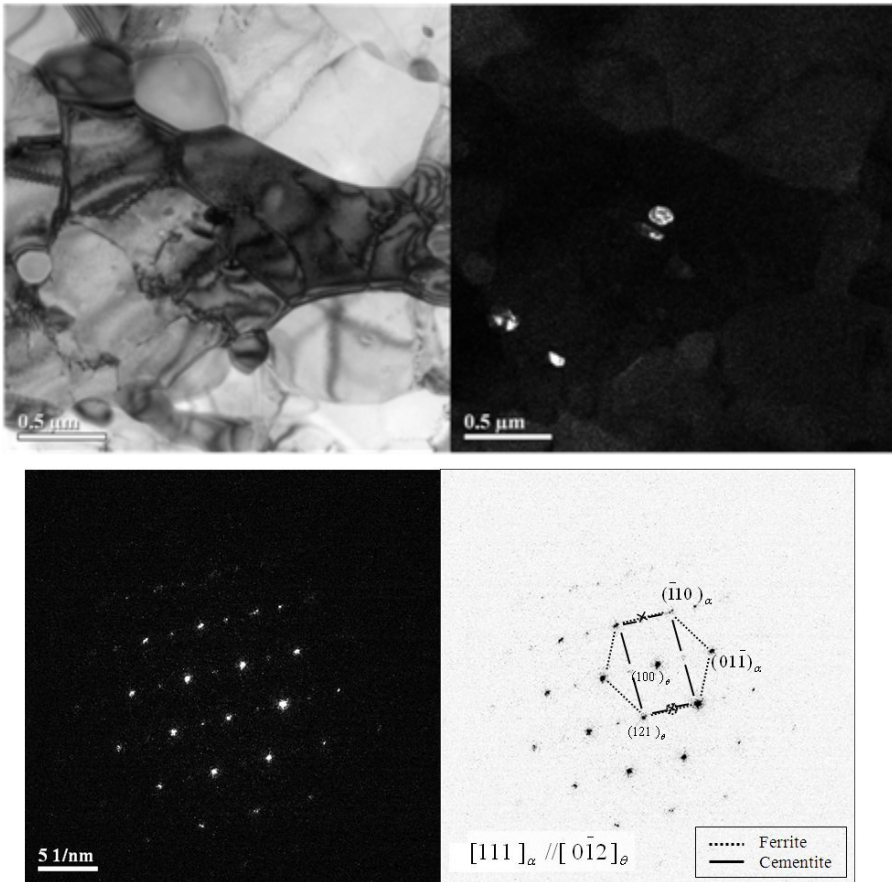
(b)
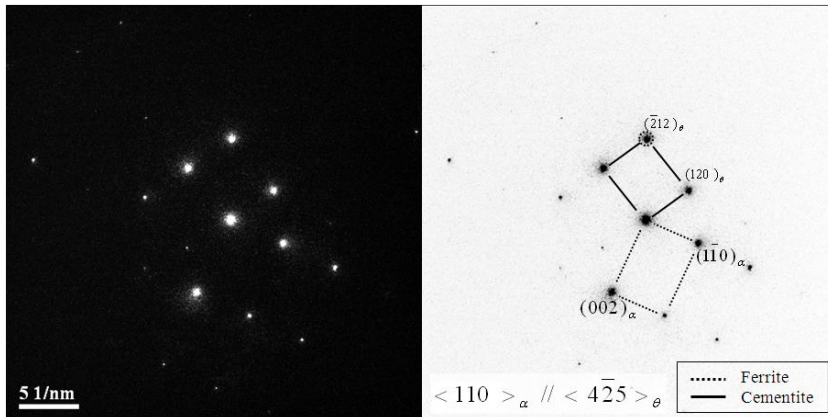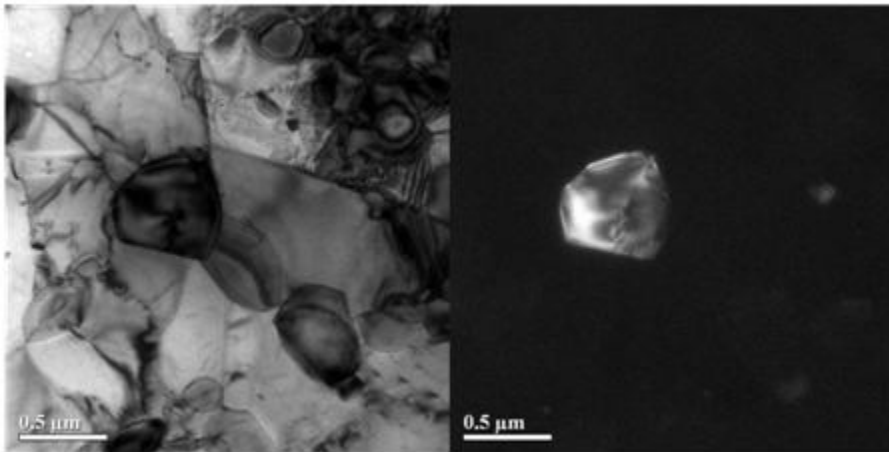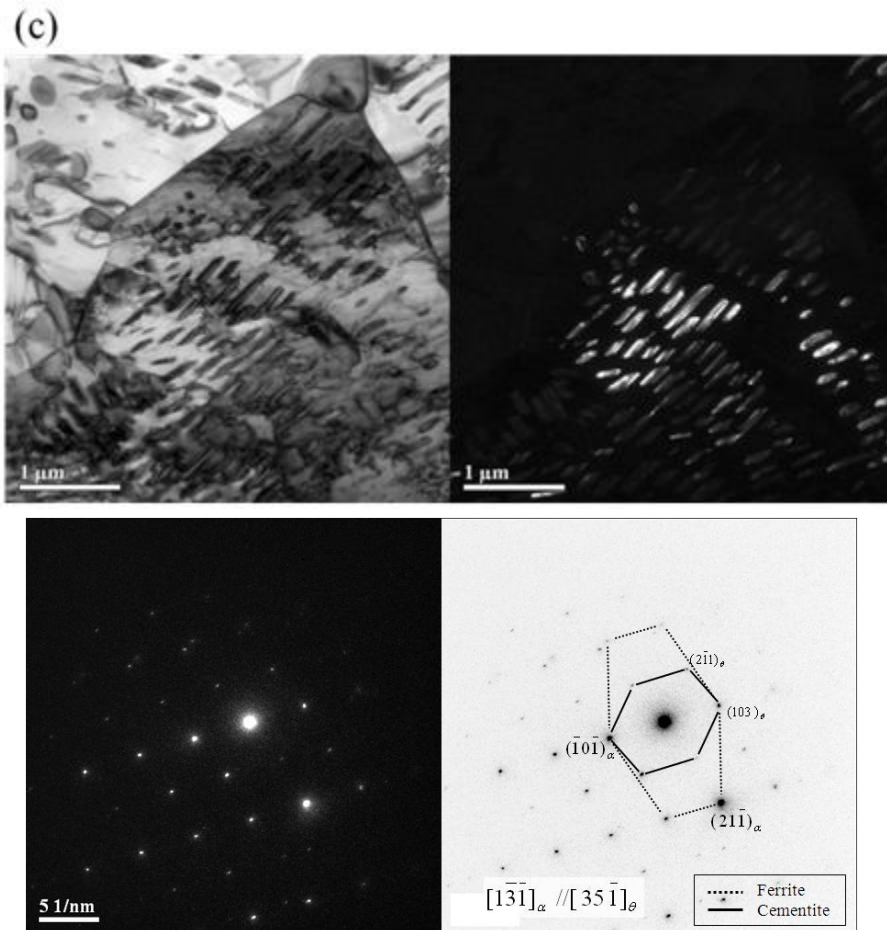
Fig. IV.20 Bright field, dark field images and diffraction patterns of the three regions of 2-800h in Fig. IV.17. (a) shows a Bagaryatski orientation relationship, (b) is inconsistent with any known orientation relationships. (c) matches with Isaichev orientation relationship better than Bagaryatski's

IV.4. Alloy 3

Samples of Alloy 3 heat-treated for 200 h and 400 h are designated as 3-200h and 3-400h. Both had the similar morphology (Fig. IV.21), with pearlite and separated ferrite. Banding was unnoticeable. However, some areas contain small amounts of ferrite with grey contrast under low magnification in comparison with regions having discrete features of ferrite and pearlite. Hence, it seems that the bands still exist although these regions also contain pearlite. There are infrequent regions where it contains spherical cementite (Fig. IV.22(a)). The rarity may be due to the fact that the martensitic bands had been incorporated into austenite matrix after the first anneal (Fig. III.6). As seen in Fig. IV.22(b), the pearlite colony boundaries contain coarse spherical cementite particles. Sometimes, they are connected to the pearlitic cementite and the other times, they exist independently. The pearlite often shows divergence and spheroidization, probably when it originates from large austenitic regions as in Alloy 2.

97
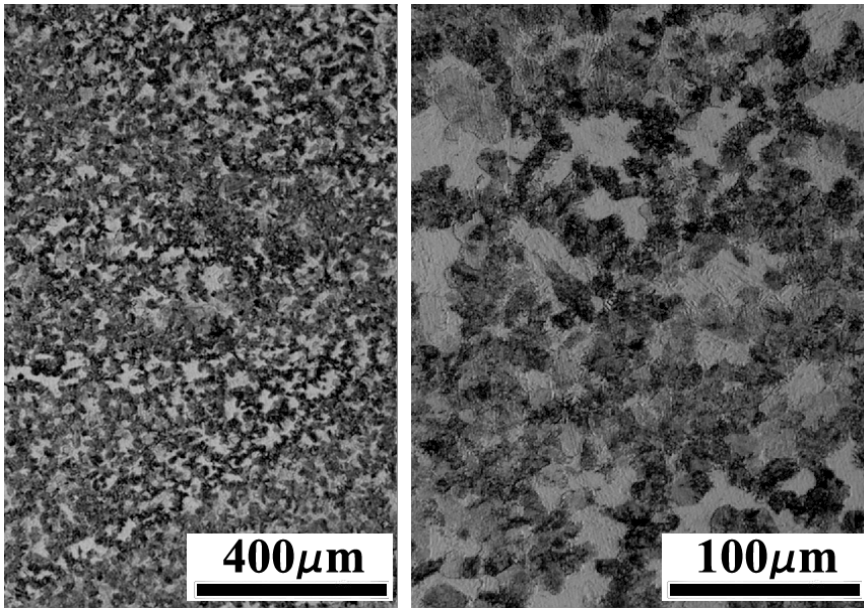
Fig. IV.21 Optical micrographs of 3-400h. The dark region corresponds to pearlite and the light phase to ferrite.

(a)
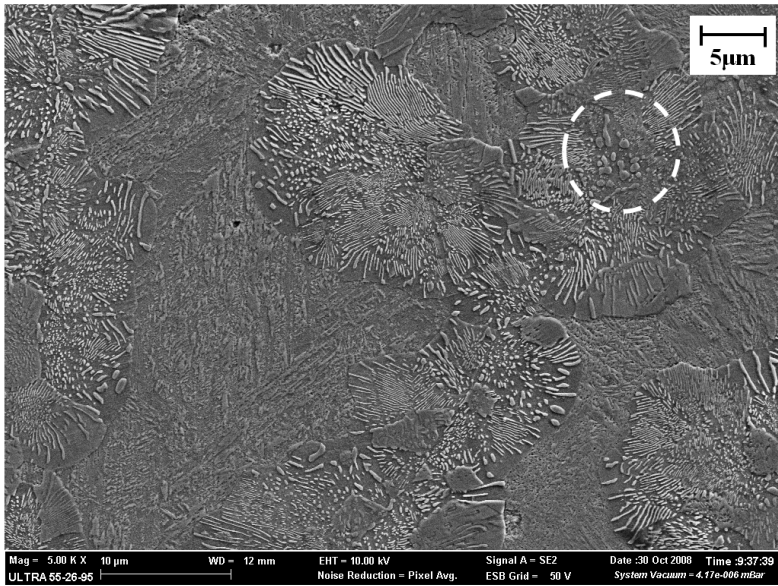
(b)
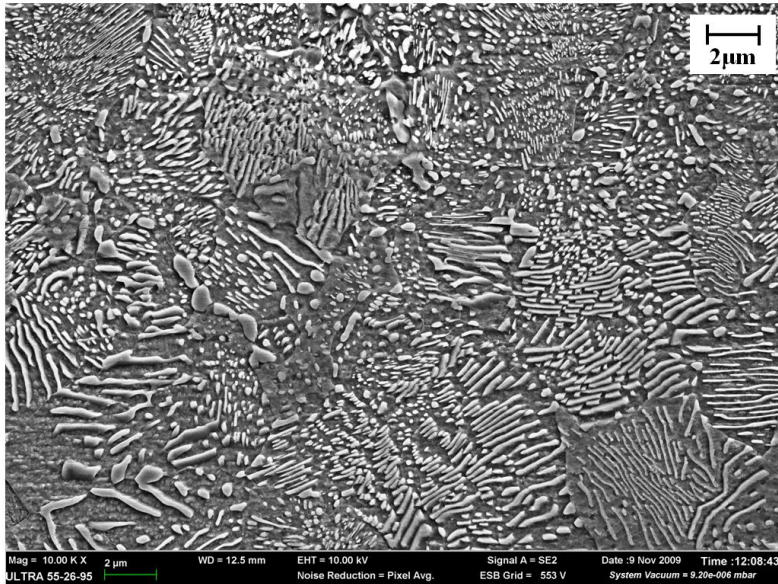
Fig. IV.22 FE-SEM images of 3-200h. The circled region in (a) shows spherical cementite particles.

The amount of phases obtained by XRD and pixel-counting method are shown in Tables IV.13 and IV.14, respectively. As observed in Alloys 1 and 2, the XRD results are unreasonably low. The calculated equilibrium cementite content of 9.1 vol.% is about half that obtained using pixel counting. All the samples show similar phase fractions.

Alloy	Ferrite / wt%	Austenite / wt%	Cementite / wt%	R_{wp}	R_{exp}	χ^2
3-200h	98 ± 2	0 ± 0	2 ± 1	24.5	14.38	2.9
3-400h	98 ± 2	0 ± 0	2 ± 1	22.8	13.96	2.66

Table IV.13 Quantitative XRD analysis of alloy 3 after the second anneal, using the Rietveld refinement method.

Alloy	Pearlitic region / vol. %	Cementite / vol. %
3-200h	79 ± 1	25 ± 5
3-400h	78 ± 3	20 ± 3

Table IV.14 Vol. % of pearlitic region and cementite in Alloy 3 after the second anneal obtained by pixel counting method. Note that the pearlitic regions consist of two phases: ferrite and cementite.

The bulk hardness tests showed HV 302 ± 9 for 3-200h and HV 278 ± 3 for 3-400h and the softening seems to be generated from the coarsening of cementite. In the case of Alloy 3, only small degree of delay of austenitization

was detected (Fig. IV.23, Table IV.15) comparing with other alloys.
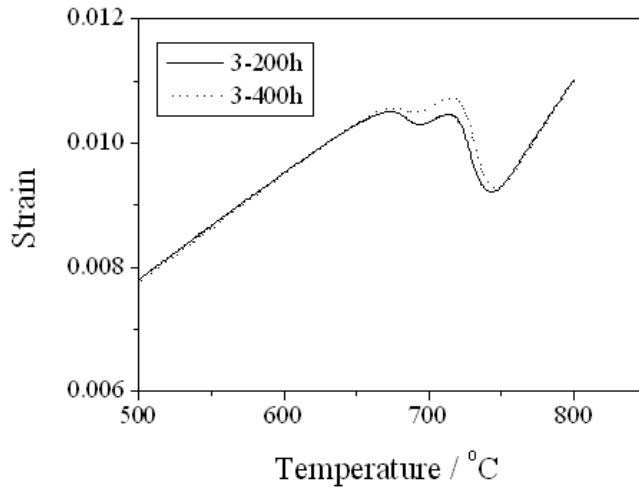
Fig. IV.23 Dilatation curve during heating of Alloy 3. The decrease of strain between 650-750 ℃ is due to the austenitization. The heating rate was 5 ℃ s^{-1}.

Alloy	Austenite-start temperature / ℃	Austenite-finish temperature / ℃
3-200h	658	747
3-400h	660	749

Table IV.15 Austenite-start and finish temperature of Alloy 3 obtained from the data in Fig. IV.23. The temperatures are acquired by offset method (Yang and Bhadeshia, 2007).

The Mn concentration of cementite is shown in Table IV.16 and the regions analyzed are given in Figs. IV.24 and IV.25. While some of the cementite in 3-200h did not achieve equilibrium where the Mn concentration would be 47.1 wt %, the process was completed after 400 h of tempering.

Alloy	Mn content of θ / wt%	Mn content of θ considering C / wt%	Mn content of α / wt%
3-200h	37.4 ± 7.3	34.8 ± 6.8	3.0 ± 0.5
3-400h	43.9 ± 2.2	41.0 ± 2.0	4.1 ± 0.1

Table IV.16 Mn content of cementite (θ) and ferrite (α) in pearlitic region of Alloy 3 after the second anneal. The values in the third column were calculated by assuming 25 at% C in cementite. Mn content of ferrite is obtained assuming zero carbon. The calculated equilibrium concentration of Mn in ferrite is 3.0 wt%
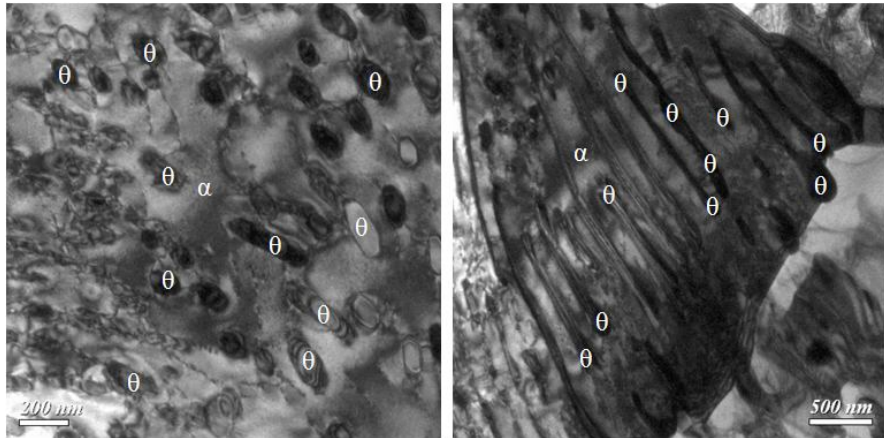
Fig. IV.24 Bright field images of 3-200h where the Mn content is obtained. The particles analyzed are annotated. Even though the left image shows spherical cementite particles, it is pearlitic region because the particle size is small and the precipitates are mostly located inside the grains. Ferrite is indicated as α and cemenite, θ.
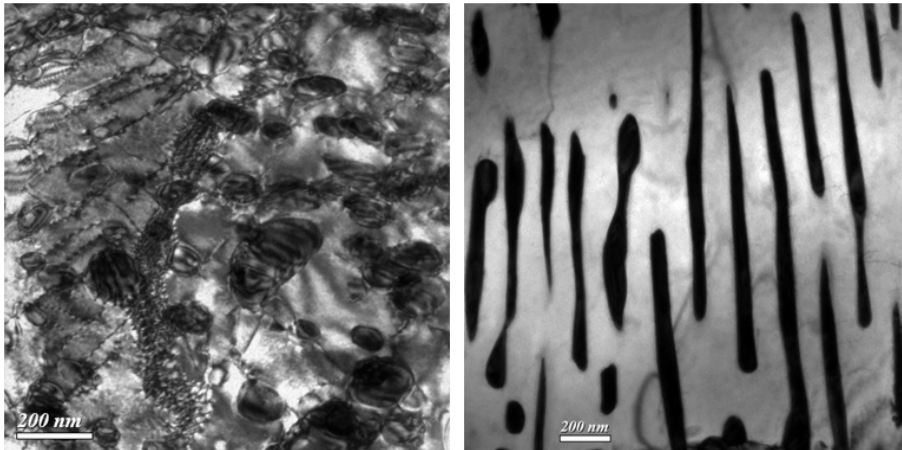
Fig. IV.25 Bright field images of 3-400h where the Mn content is obtained. Even though the left image shows spherical cementite particles, it is pearlitic region because the particle size is small and the precipitates are mostly located inside the grains. The phases were not designated, but the five cementite points and one ferrite points were obtained from each region.

All regions shown in Figs. IV.24 and IV.25 were subjected to orientation relationship analysis. The studied diffraction patterns, bright and dark field images are given in Figs. IV.26 and IV.27. Pearlitic cementite in Alloy 3 was found to have Bagaryatski, Pitsch-Petch or sometimes, no recognizable orientation relationship with the ferrite matrix.

(a)

$<100>_{\alpha}$ // $<111>_{\theta}$

$(002)_{\alpha}$
$(10\bar{1})_{\theta}$
$(01\bar{1})_{\theta}$
$(011)_{\alpha}$

······· Ferrite
——— Cementite
—·—· Double Diffraction
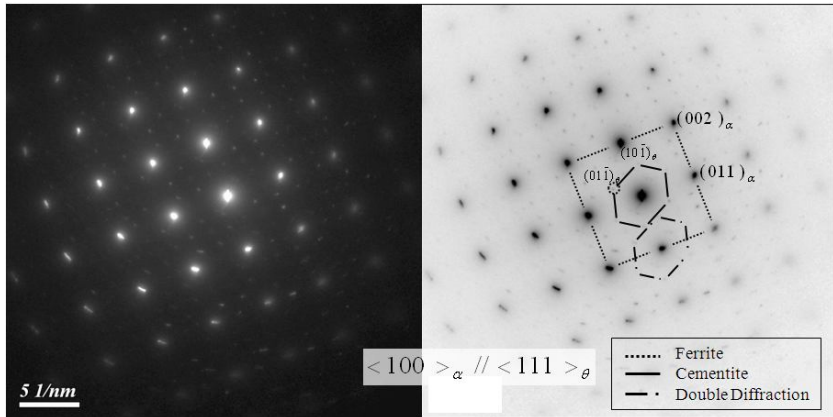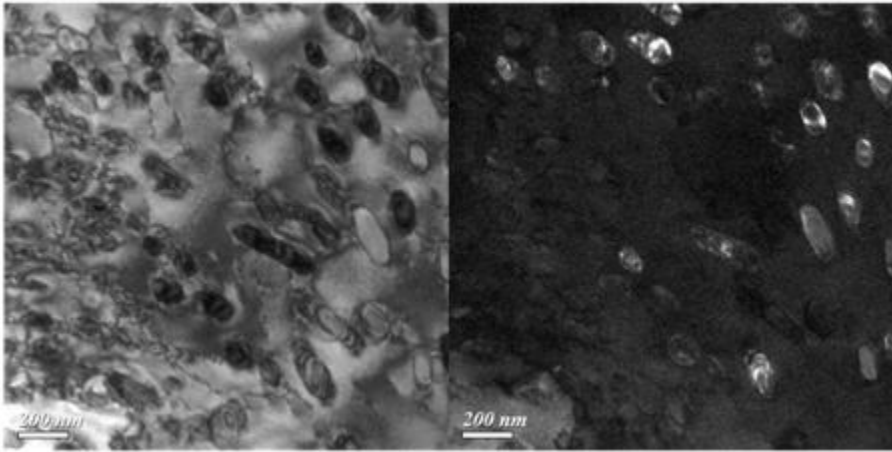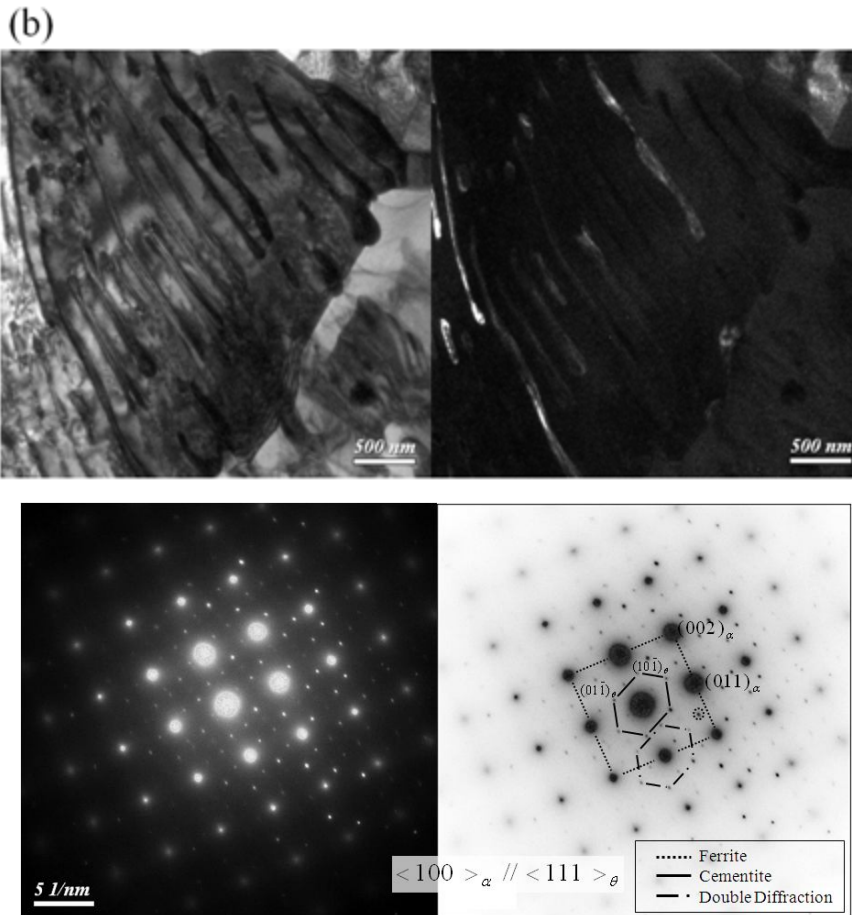
Fig. IV.26 Bright field, dark field images and diffraction patterns of the two regions of 3-200h in Fig. IV.24. None of them show known orientation relationship but have the same orientation relationships. The reflections for the dark field images are given as circle in the diffraction patterns.

(a)

(b)

200 nm

200 nm

5 1/nm

$(112)_\alpha$

$(\bar{1}01)_\alpha$

$(330)_\theta$

$(10\bar{3})_\theta$

$[1\bar{3}1]_\alpha // [3\bar{3}1]_\theta$

.... Ferrite
——— Cementite
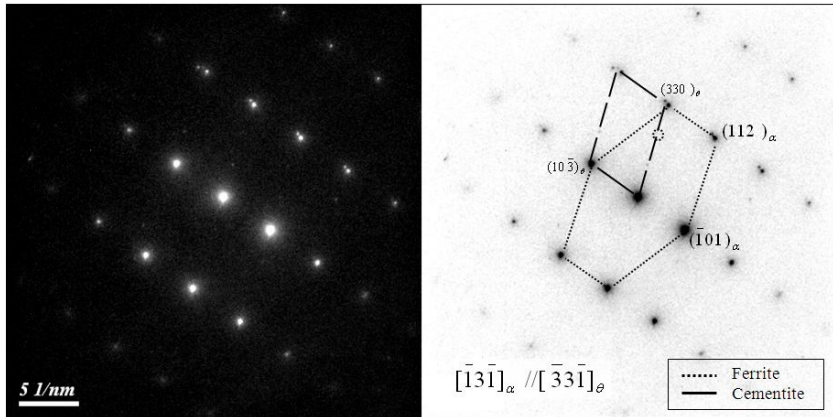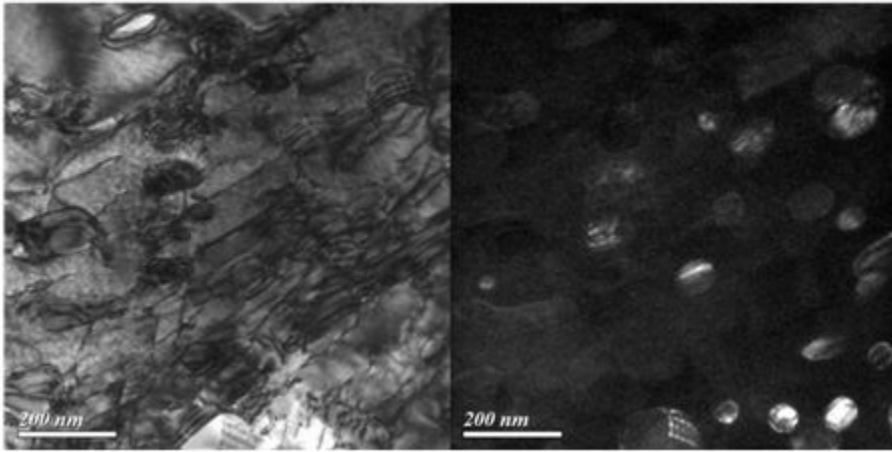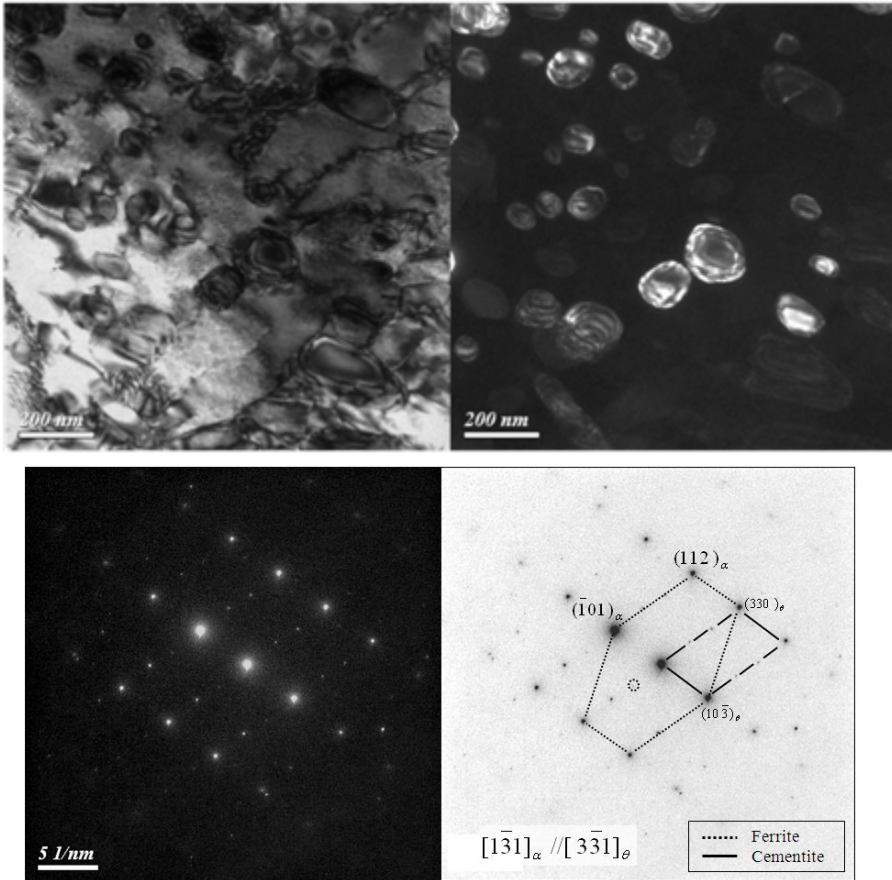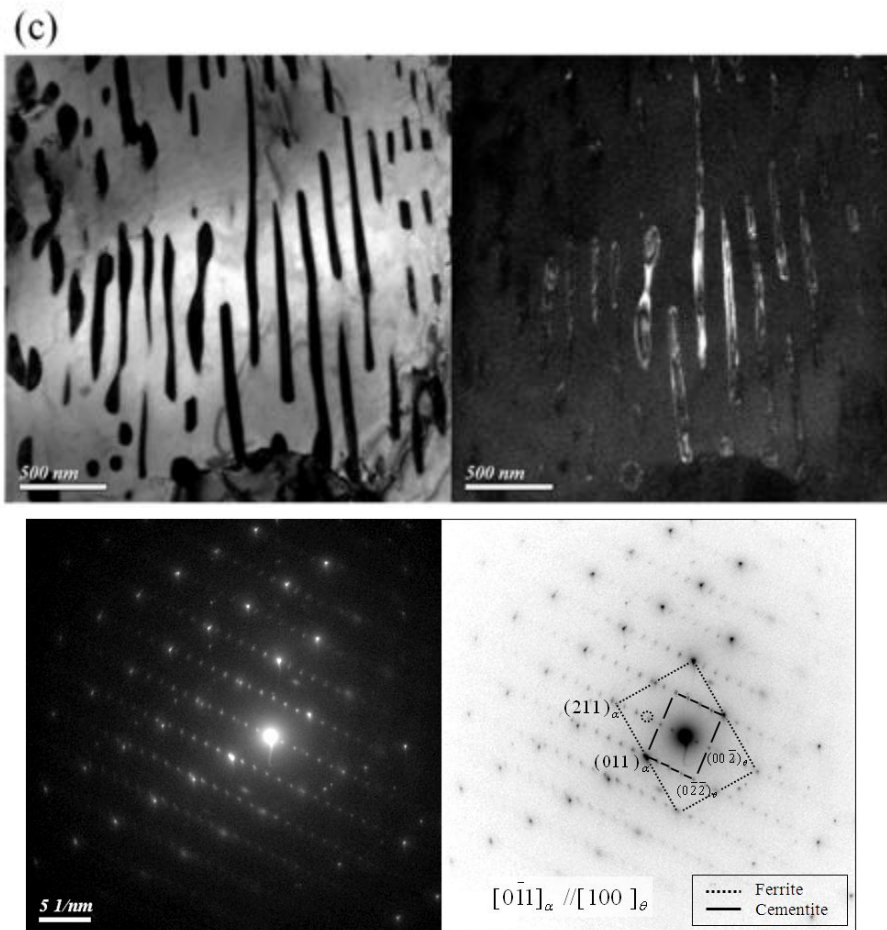
Fig. IV.27 Bright field, dark field images and diffraction patterns of the three regions of 3-400h in Fig. IV.25. (a) and (b) show Pitsch-Petch and (c) shows Bagaryatski orientation relationship. The reflections for the dark field images are given as circle in the diffraction patterns.

IV.5. Discussion

IV.5.1. Volume Fractions and Mn contents in Cementite

The volume percent of cementite after the second anneal, obtained by pixel counting, is shown Fig. IV.28. The XRD results for each alloy were 1 ± 1 wt% for Alloy 1, 2 ± 1 for Alloys 2 and 3 which were underestimated and unreasonable. With the results by pixel counting, Alloy 1 had the lowest cementite volume fraction, with about double the quantity in Alloys 2 and 3. The trend corresponds to that expected from Table II.3 and with the concentration of C. The Mn contents of cementite in all alloys are shown in Fig. IV.29. Even though the tempering time was as long as 400 or 800 h, the average value did not reach equilibrium because the cementite particle size and nucleation instants vary. However, there were always some particles which achieved equilibrium in all alloys.
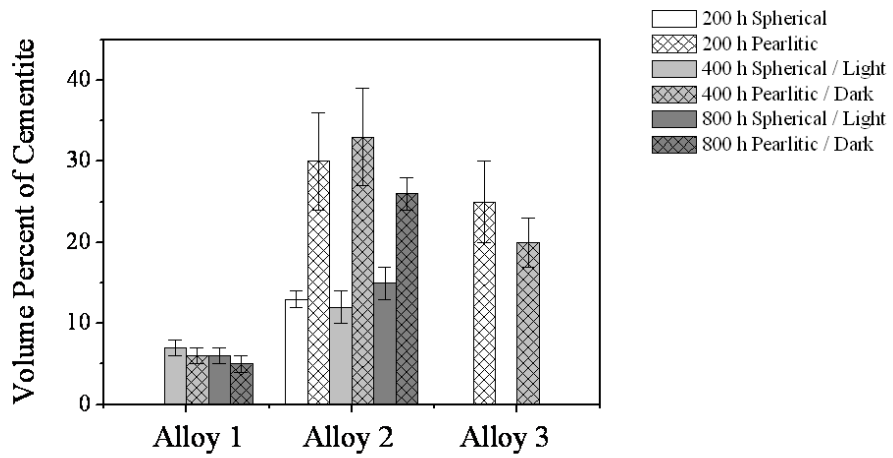
Fig. IV.28 Volume percent of cementite in each alloy obtained by the pixel counting method. The numbers in the legend indicate the second anneal time. Since the values in spheroidite and pearlite vary for Alloys 2 and 3, they are plotted separately. For Alloy 1, the light and dark-contrast regions were plotted separately.
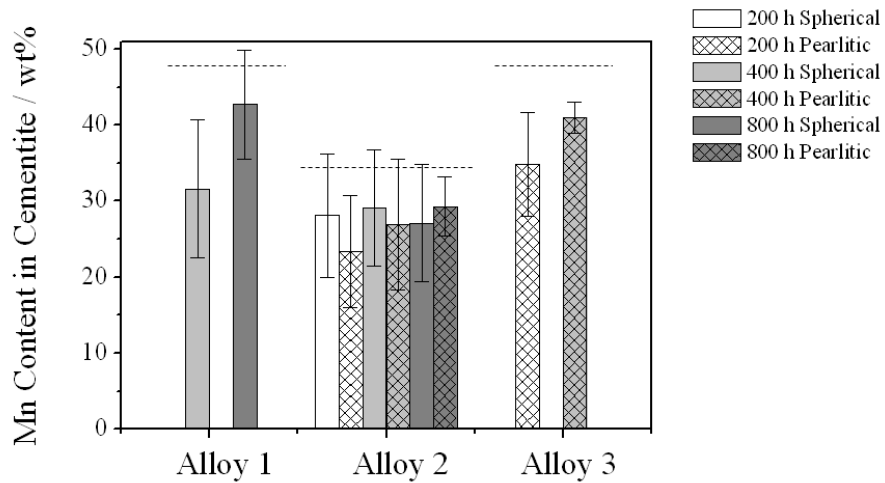
Fig. IV.29 Mn contents of cementite in all alloys. The numbers in the legend indicate the second anneal time. For Alloy 1, only spherical cementite results were shown because of the absence of pearlite, and for Alloy 3, only pearlitic cementite results were shown since the spherical cementite were rarely observed and no data were obtained for that case. The dotted lines indicate equilibrium Mn contents.

IV.5.2. Pearlite Formation and its Morphology

In alloy 2 and 3, the pearlite microstructure was observed, originating from the austenite which present after the first anneal. Since the compositions of the austenitic regions were known (Table III.10), the ternary equilibrium

phase diagram of Fe-Mn-C system was calculated by MTDATA and corresponding compositions were marked in Fig. IV.30. It should be noticed that the marked austenite composition can be changed since the austenite system is not closed one, so the Mn and C diffusion can occur during the tempering. Since the Mn content is high in austenite than martensite, Mn might diffuse from austenite to martensite and the Mn content of austenite would be lower than that in Table III.10. On the other hand, C can be varied in both directions, higher and lower. Thus, the austenite in Alloys 2 and 3 can be in ($\alpha + \gamma + \theta$) or ($\alpha + \theta$) phase field. Considering the initial and final microstructures of Alloys 2 and 3, the schematics of phase formation during tempering and air cooling are shown in Fig. IV.31. Since the final structure of Alloy 2 did not consist of the ferrite existing as a separate phase, the austenite in Alloy 2 seems to have been in ($\alpha + \theta$) region and since the Alloy 3 had the ferrite, the austenite is expected to have been in ($\alpha + \gamma + \theta$) region and during air cooling, the remained austenite decomposed into proeutectoid ferrite and pearlite.
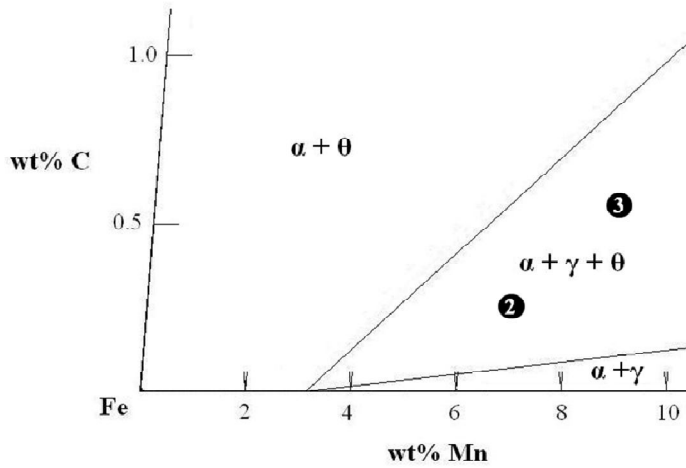
Fig. IV.30 Enlarged ternary phase diagram for Fe-rich corner at 550 ℃. The dark circle indicates the austenite compositions and the number in the circle represents the kind of the alloy.
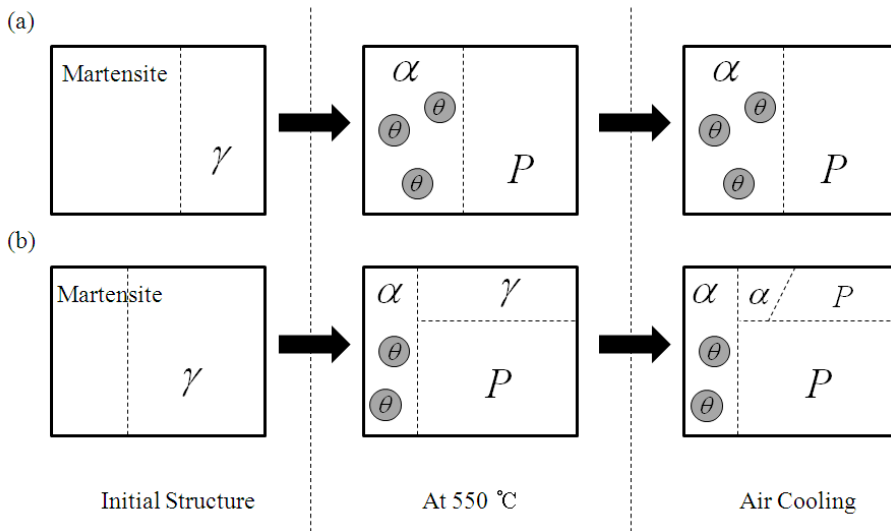
Fig. IV.31 Illustration of microstructure evolution for (a) Alloy 2 and (b) Alloy 3 during the second anneal and cooling.

114

An interesting morphology in pearlite was observed: divergent pearlite, which has been often reported previously (Cahn and Hagel, 1963, Hutchinson *et al.*, 2004). There are two major reasons for this phenomenon. The first is when the austenite composition lies in the ($\alpha + \gamma + \theta$) phase field, the austenite composition continually changes during pearlite formation and this slows down the lateral pearlite growth resulting in divergent lamellar structure. Second one is that the soft impingement of pearlite colonies results in lack of C resulting in divergency.

IV.5.3. An Assumption of Negligible Coarsening

In the section IV.1, it was assumed that the driving force of cementite coarsening was much smaller than that of alloying element partitioning for the FINITE calculation. As mentioned before, it is known that the cementite coarsening rate decreases during martensite tempering if any substitutional alloying element is introduced in the alloy. For Fe-Mn-C system which contains 1 or 2 Mn and 0.6 C (wt%), it has been shown that the cementite size reaches the value calculated by the equation introduced by Björklund after time greater than about 10^5 s (Fig. IV.32).
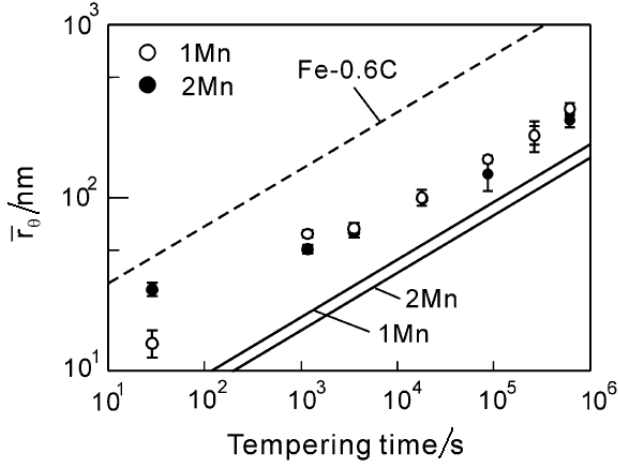
Fig. IV.32 Comparison of the coarsening kinetics of cementite between experiments and calculations in tempering at 923K for Fe-0.6C-Mn alloys. The error bars represent ±1 standard deviation of $\bar{r}_\theta$, the mean particle radius of cementite. The dotted line is the fitting curve for experimental results of Fe-0.6 C. and the solid line represents the calculated values by Björklund (Miyamoto et al., 2007).

The equation introduced by Björklund for a Fe-Mn-C system is as follows (Björklund *et al.*, 1972).

$$\bar{r}^3 - \bar{r}_0^3 = \frac{8\sigma V_m^{cem} D_{Mn}}{27RT(1-K)^2 Y_{Mn}^\alpha}(t-t_0) \qquad \text{(Eq. IV.1)}$$

where $\bar{r}$ is the mean particle radius of cementite at time t, $\bar{r}_0$ is that at time t_0 when steady-state growth begins, σ is the α/θ interface energy,

V_m^{cem} is the molar volume of cementite, D_{Mn} is the diffusivity of Mn in ferrite, K is a partitioning coefficient equal to $Y_{Mn}^{\theta} / Y_{Mn}^{\alpha}$. Here, Y_{Mn}^{θ} is the site fraction of Mn in cementite, Y_{Mn}^{α} is that in ferrite. It should be noticed that the particle size is inversely proportional to $(1-K)^2$. It implies that the larger the partitioning, the smaller the particle size at given time since K is larger than unity. The particle sizes for Alloys 1, 2 and 3 were calculated using Eq. IV.1 for the given second annealing time at 550 ℃ (Table IV.17). $\bar{r}_0$ and t_0 were considered to be negligible and σ was given as 0.7 J m^{-2} (Kramer *et al.*, 1958). The results were almost the same for all alloys and seem to have been underestimated considering the microstructure shown the sections ahead. The discrepancy may come from a couple of assumptions made when deriving Eq. IV.1. First assumption was the low degree of alloying, and second one was complete partitioning alloying element. Since these assumptions are not justified in the present cases, the results do not match with the experimental data. Moreover, if the equilibrium composition was not reached for cementite, K becomes small and the calculated size is large. Hence, the calculated size was a lot smaller that the experimental size because the particle is in the process of partitioning during tempering.

Alloy	200 h / nm	400 h / nm	800 h / nm
Alloy 1	-	61	77
Alloy 2	48	61	76
Alloy 3	49	61	-

Table IV.17 The calculated cementite particle size from Eq. IV.1 for each alloy.

Considering all the expected values and experimental results, the latter did not exactly match with the former. However, since there were some cementite particles as large as several hundred nanometers and the majority of cementite showed over 30 wt% Mn, the second anneal was good enough to continue the third anneal.

V. Third Anneal – Formation of Austenite

V.1. Alloy 1

By trial and error with dilatometry, the third annealing temperature has been set to 670 ℃ for both 1-400h and 1-800h. The dilatation curves in respect to time and temperature are shown in Figs. V.1 and V.2.
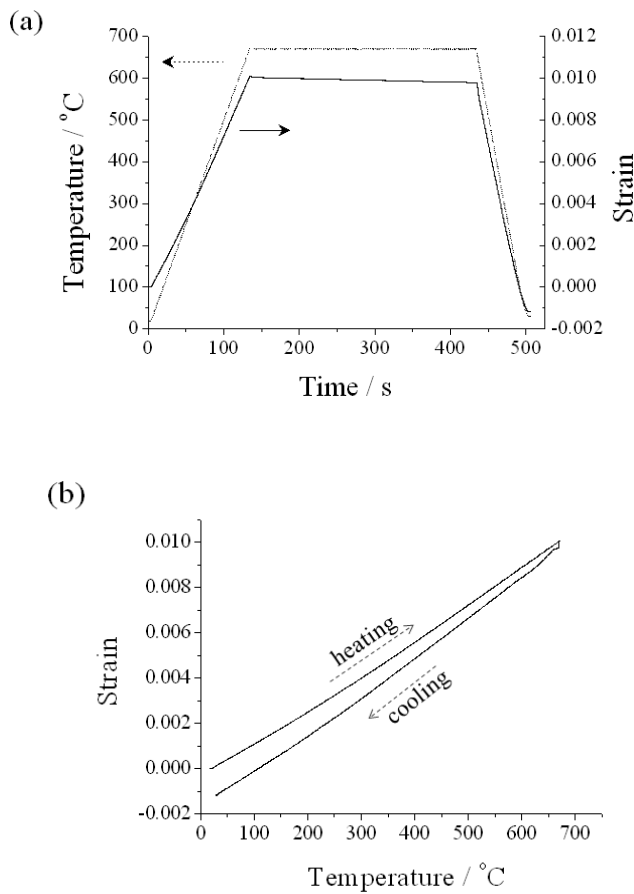
Fig. V.1 Dilatation curves of 1-400h. (a) Temperature and strain with respect to time (b) Strain verses temperature.
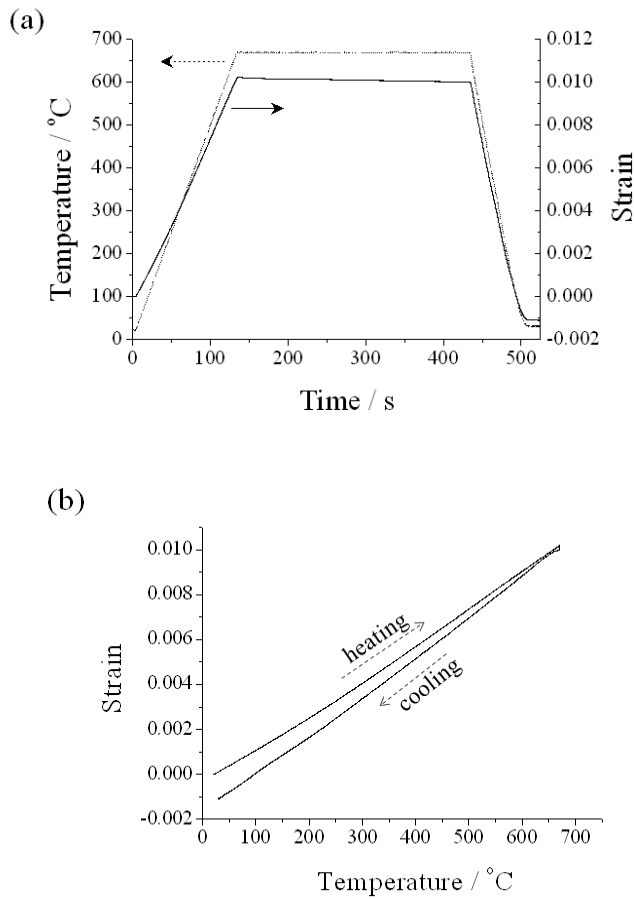
Fig. V.2 Dilatation curves of 1-800h. (a) Temperature and strain with respect to time (b) Strain verses temperature.

In Figs. V.1(a) and V.2(a), the strain decreased steadily during the isothermal heat treatment, which implies that the equilibrium had not been reached. The degree of decrease was small so the amount of austenite formed was expected to be also small. In Figs. V.1(b) and V.2(b), there was a slight

curvature during cooling. Thus, there can be small amount of martensite formed even though the conspicuous strain change was not detected.

The morphologies of 1-400h and 1-800h were similar and representative micrographs are presented in Fig. V.3. Banded regions due to Mn segregation are still evident. High magnification images of each region are given in Fig. V.4. The large protruded part located in the middle of Fig. V.4(a) cannot be austenite nor martensite since it is also observed in Fig. IV.6(a). Instead, at upper right part of Fig. V.4(a) and all regions in Fig. V.4(b), the phase which formed a layer surrounding cementite was expected to be austenite or martensite. This region is observed more frequently in dark-contrast region. Also, there were spherical particles too large, about 2 μm, to be considered as cementite. Several particles of this kind are shown in Fig. V.4(b). However, it was hard to tell whether these were austenite or martensite.

XRD was adopted to check the existence of austenite in the samples and the results are given in Table V.1. It is shown that 9 and 5 vol. % of austenite existed in 1-400h and 1-800h, respectively.
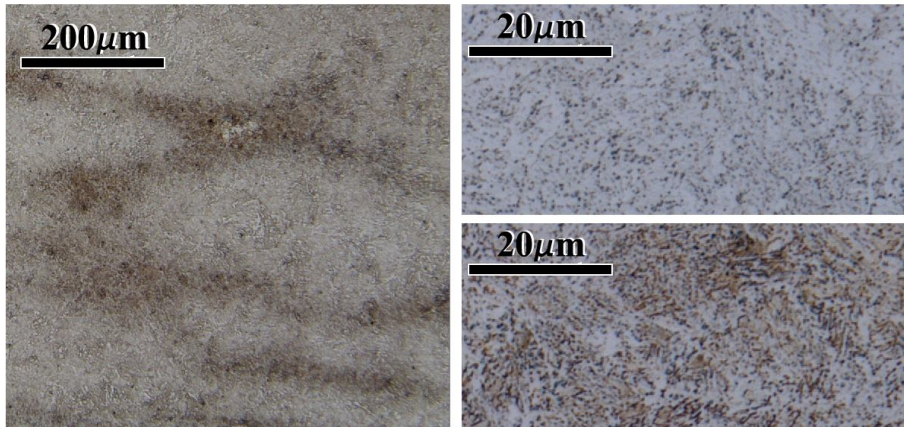
Fig. V.3 Optical micrograph of 1-400h after the third anneal (at 670 ℃ for 5 min). The sample is etched with 1 % nital. Notice the bands of dark contrast parallel to the rolling direction. The upper and lower images are from the light and dark-contrast regions.

(a)
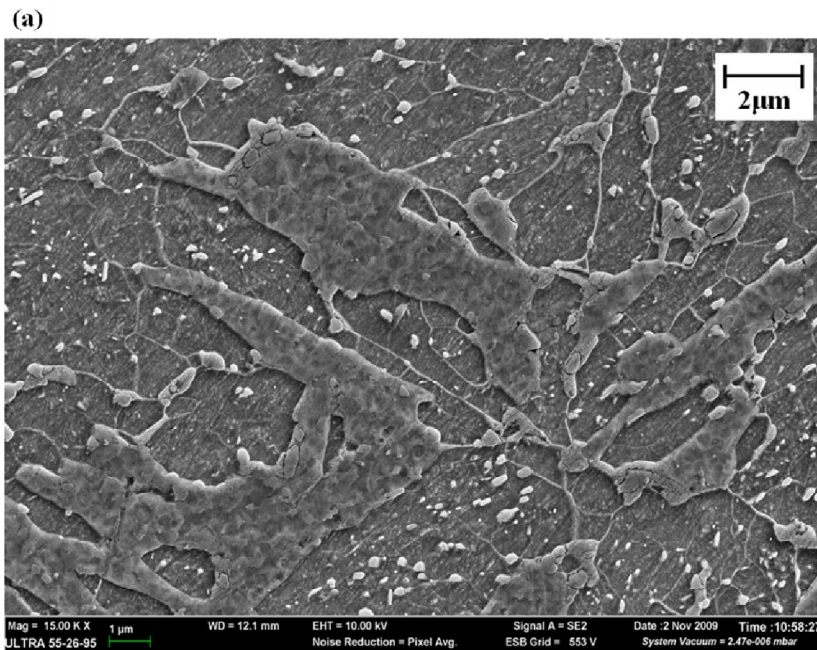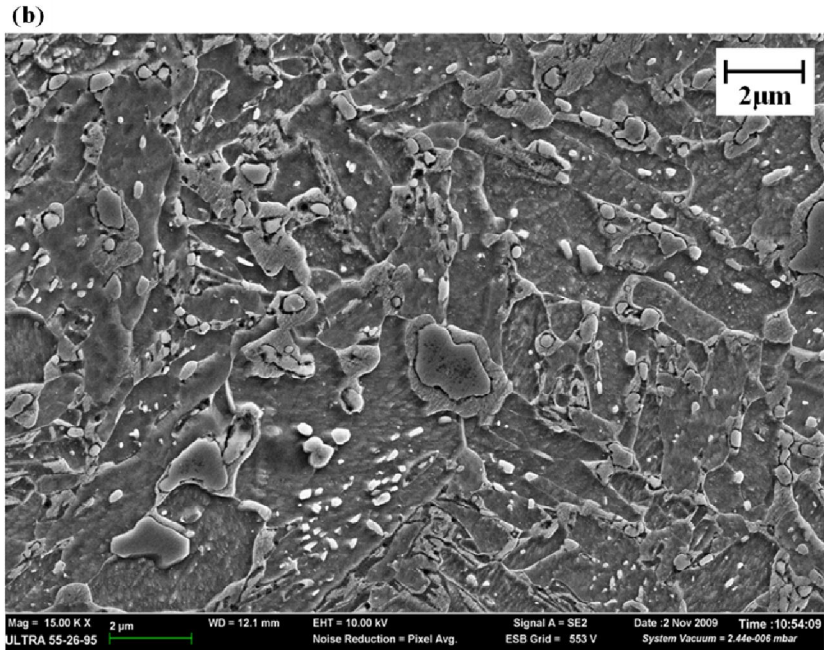
Fig. V.4 FE-SEM images of 1-800h. (a) The light-contrast region and (b) the

dark-contrast region in Fig. V.3.

Alloy	Ferrite or martensite / wt%	Austenite / wt%	Cementite / wt%	R_{wp}	R_{exp}	χ^2
1-400h	91 ± 1	9 ± 1	0 ± 1	22.4	15.85	2.00
1-800h	93 ± 2	5 ± 1	2 ± 1	22.6	20.05	1.27

Table V.1 Quantitative XRD analysis results of Alloy 1 after the third anneal,

using the Rietveld refinement method. The martensite structure is similar to

that of ferrite, so the phases cannot be distinguished.

In order to distinguish austenite, observe its morphology and analyze its Mn content, TEM was adopted (Figs. V.5 and V.6). Many EDS point scans were done for each austenite region and cementite and the results are given in Table V.2. Austenite was observed to form adjacent to cementite. It surrounded the cementite and sometimes grew along the ferrite grain boundaries. The Mn content of cementite in 1-400h seems much lower than that in 1-800h. However, it comes from cementite particles which were embedded in austenite. In Fig. V.5, the cementite particles in the image on the left were all implanted in the austenite, giving low Mn concentrations and large standard deviations since the particles on right side which appears at the surface to gave high values. With the data in Table V.2 and austenite lattice parameter obtained by XRD, the carbon content of austenite was estimated as is shown in Table V.3. Even though Mn was enriched in cementite enough, the austenite that formed adjacent to the cementite did not have a high Mn content. Moreover, the calculated C content values were a little higher than expected from equilibrium, 0.4 wt%. In spite of different periods of the second anneal, 1-400h and 1-800h showed similar Mn content, but the C content was a little higher in 1-800h.
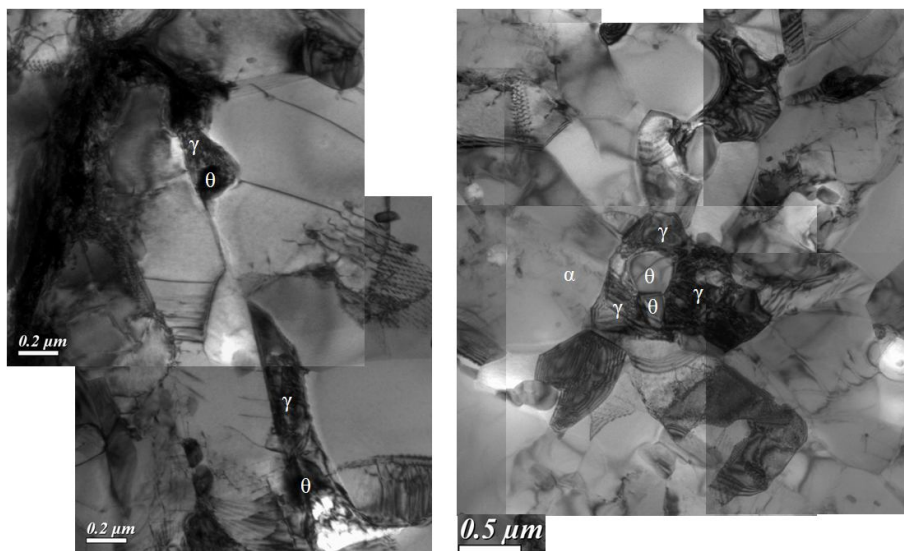
Fig. V.5 Bright field images of 1-400h indicating positions where the Mn content was determined using EDS. Ferrite is indicated as α, cemenite, θ, and austenite, γ.
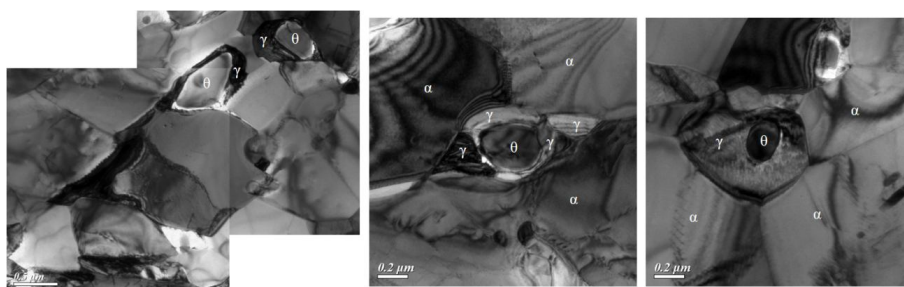
Fig. V.6 Bright field images of 1-800h indicating positions where the Mn content was determined using EDS. Ferrite is indicated as α, cemenite, θ, and austenite, γ.

Alloy	Mn content of θ / wt%	Mn content of θ considering C / wt%	Mn content of γ / wt%	Mn content of α / wt%
1-400h	36.3 ± 13.7	33.8 ± 12.8	7.4 ± 0.6	3.5 ± 0.1
1-800h	47.4 ± 3.1	44.2 ± 3.0	7.8 ± 0.9	2.8 ± 0.7

Table V.2 Mn content of cementite (θ), austenite (γ) and ferrite (α) in Alloy 1 after the third anneal. The values in the third column were calculated by assuming 25 at% C in cementite. The Mn contents of austenite and ferrite are obtained assuming zero carbon.

Alloy	Lattice parameter of γ / Å	C content of γ / wt%	Mn content of γ / wt%
1-400h	3.60137 ± 0.00069	0.496 ± 0.038	7.4 ± 0.6
1-800h	3.60792 ± 0.00447	0.684 ± 0.161	7.8 ± 0.9

Table V.3 C and Mn content of austenite (γ) in Alloy 1 after the third anneal. The C content was considered for acquiring Mn content. The lattice parameters of γ obtained by XRD analysis and Mn contents given Table V.2 were used to calculate C contents.

Regarding its morphology and alloying element concentration, austenite seems to not only grow into cementite but also into ferrite. Since its Mn content was much lower than that of cementite, austenite growth was seen to be accompanied by more consumption of ferrite than cementite. Growth into

126

ferrite seems to have occurred mostly along the ferrite grain boundaries.

The diffraction patterns and dark field images of the regions shown in Figs. V.5 and V.6 are given in Figs. V.7 and V.8. Only some of the phases in the region were under the analysis because all phases cannot satisfy low index-zone axis at the same time. Some of the cementite had a known orientation relationship with ferrite, Fig. V.8 (a.ii), (b.iv). Since the cementite was formed earlier than austenite, it is likely to have orientation relationship with ferrite. As austenite forms, it is shown that it can have orientation relationship with ferrite (Fig. V.8 (b.i, ii)), cementite (Fig. V.7 (b)) or both ferrite and cementite (Figs. V.7(c.viii, ix, x) and V.8(a.i, ii)). The most interesting observation was that all three phases, ferrite, cementite, and austenite are related to each other, Fig. V.8(a).

(a)

(i)

(ii)

$(4\bar{4}1)_\theta$

$(400)_\theta$

$(11\bar{1})_\gamma$

$(\bar{2}20)_\gamma$

$< 112 >_\gamma$ // $< 014 >_\theta$

Austenite
Cementite

0.2 µm

0.2 µm

5 1/nm

(b)

(i)

(ii)

$(\overline{2}\overline{2}0)_\gamma$

$(1\overline{1}3)_\theta$

$(103)_\theta$

$(\overline{1}11)_\gamma$

$[1\overline{1}2]_\gamma \, // \, [\overline{3}01]_\theta$

Austenite

Cementite

0.2 µm

0.2 µm

0.2 µm

5 1/nm

(c-1)

(viii)

5 1/nm

$(220)_\gamma$

$(102)_\theta$

$(111)_\gamma$

020

$[\bar{1}10]_\gamma$ // $[\,201\,]_\theta$

Austenite
Cementite

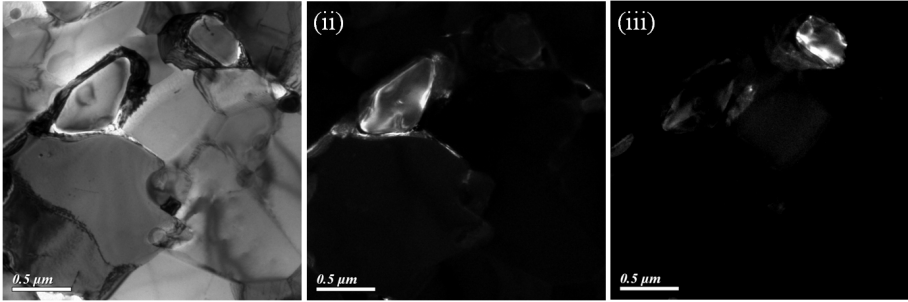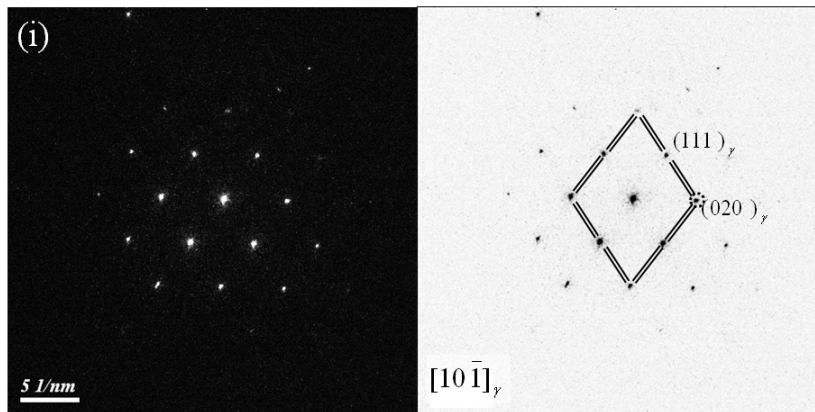(c-2)
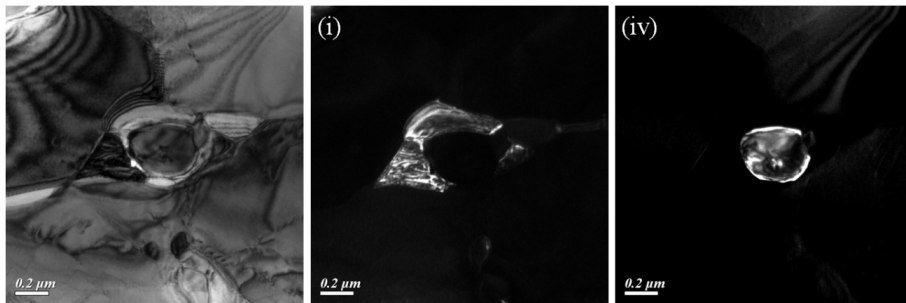
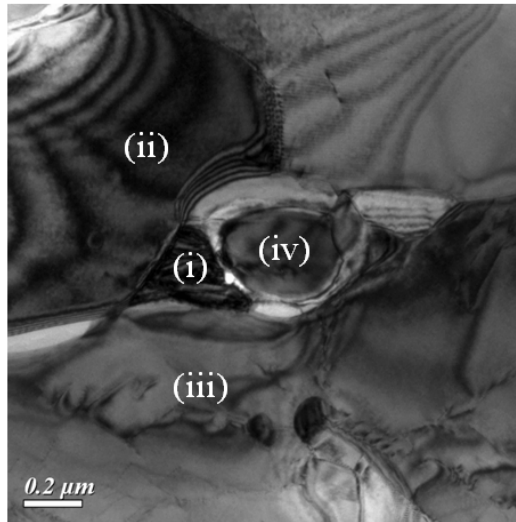0.2 μm

(ix)

0.2 μm

(x)

0.2 μm

133
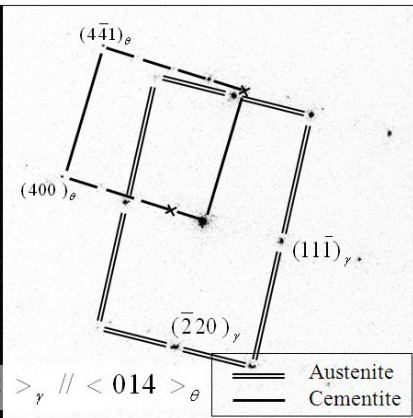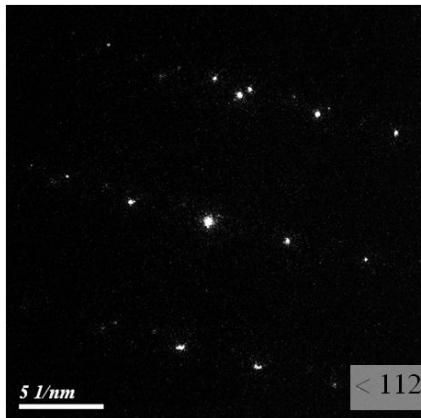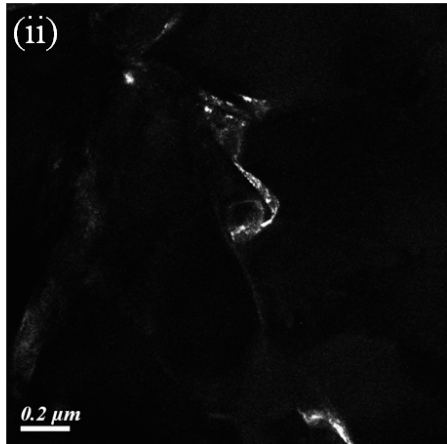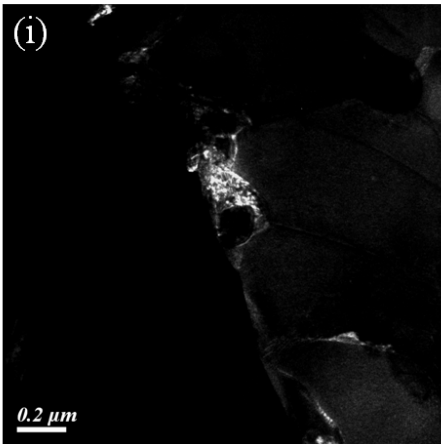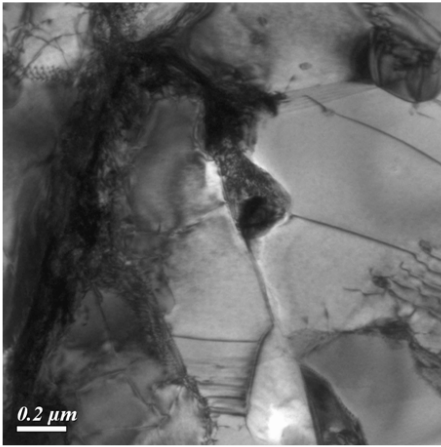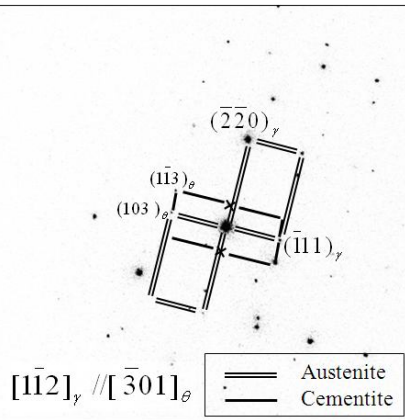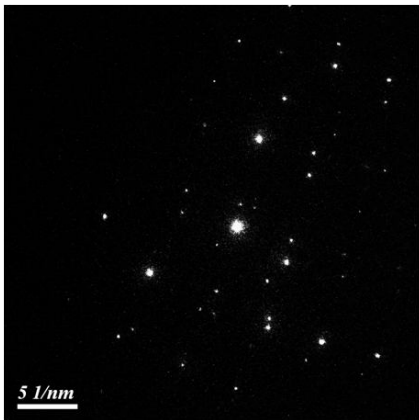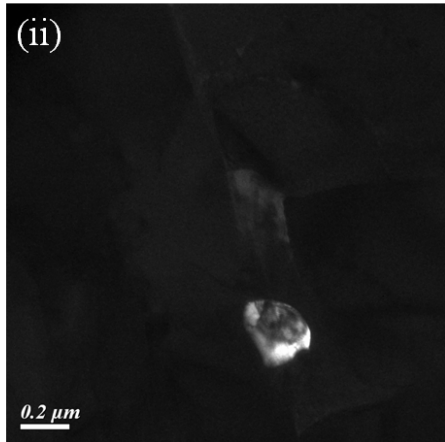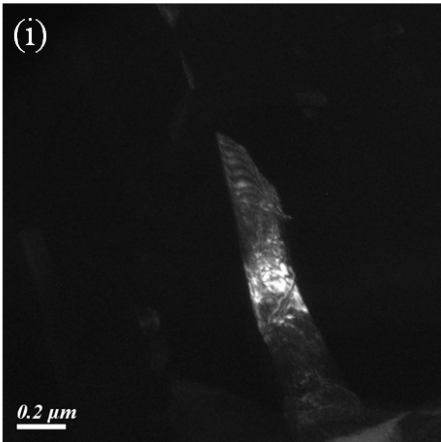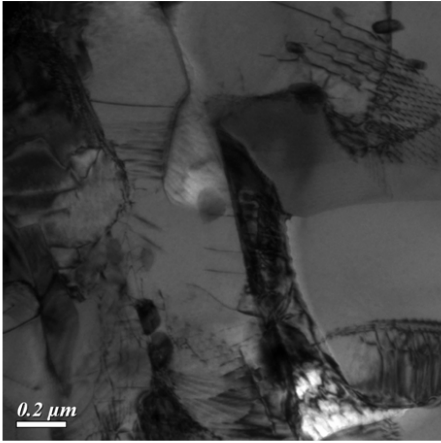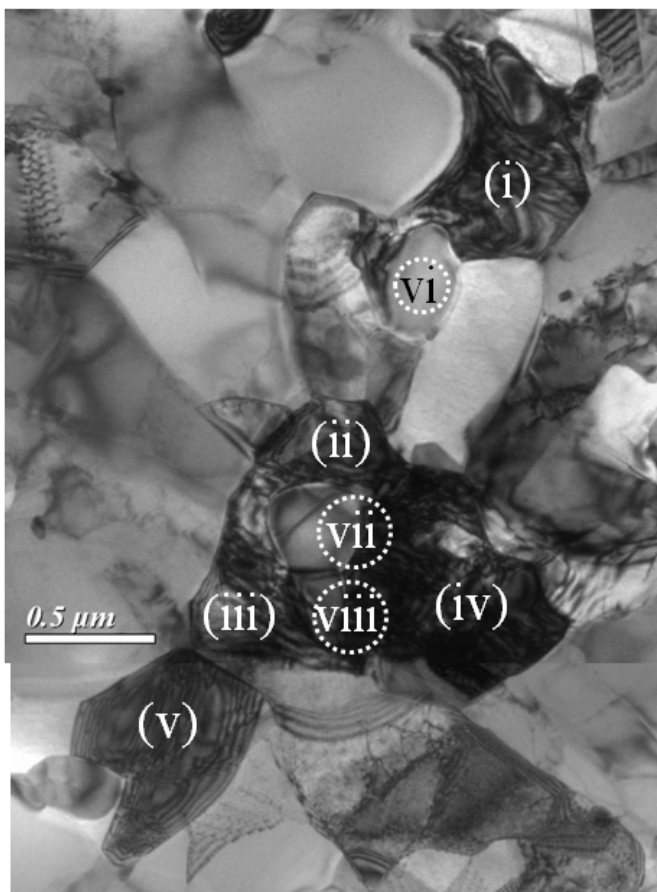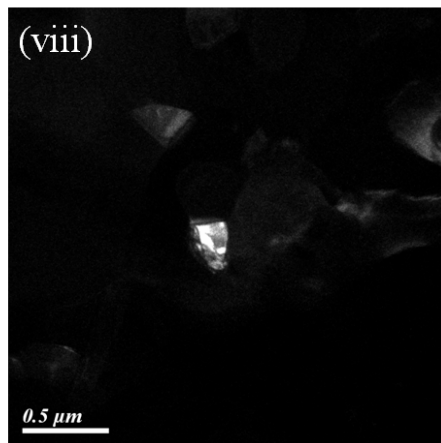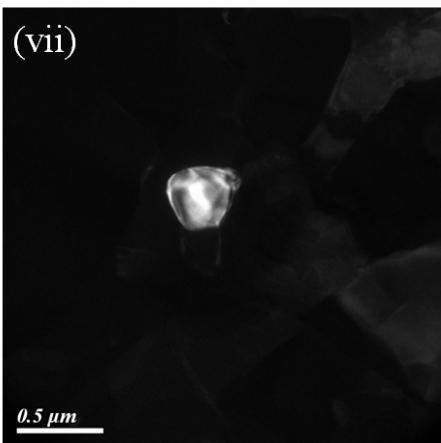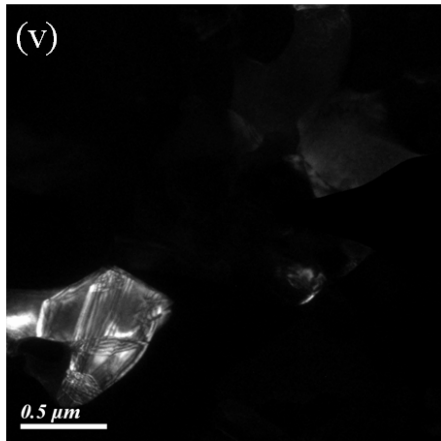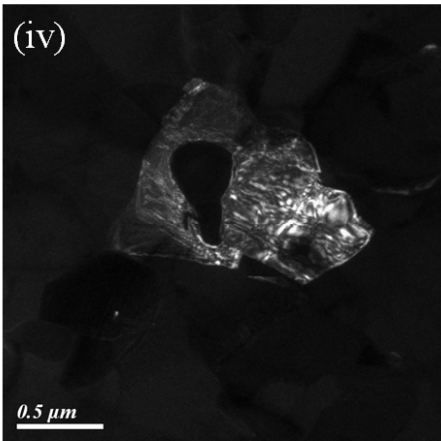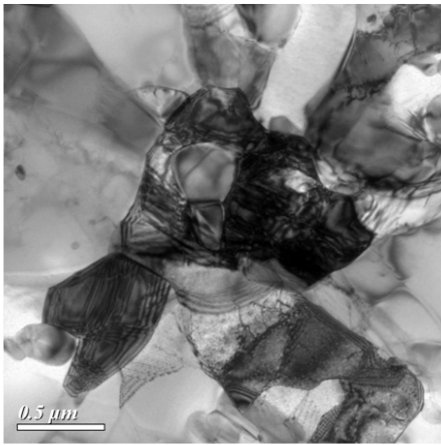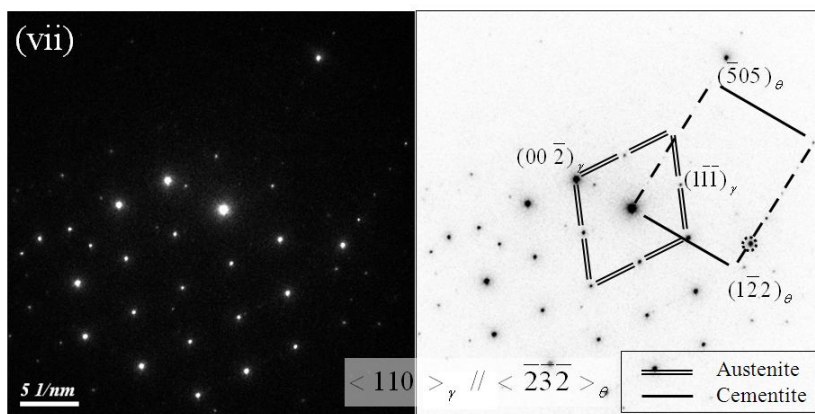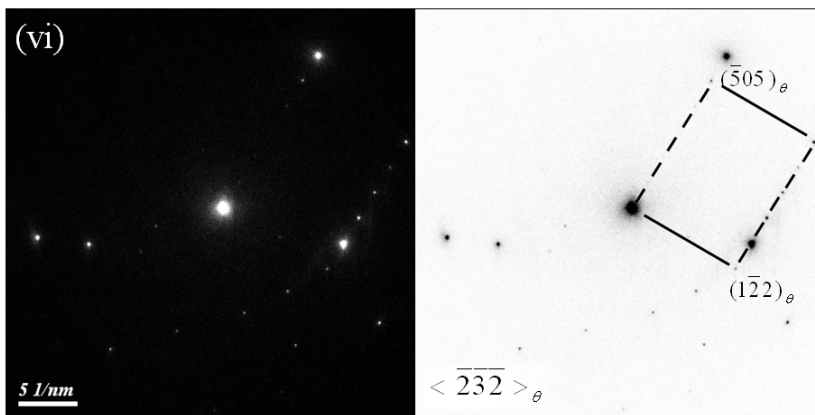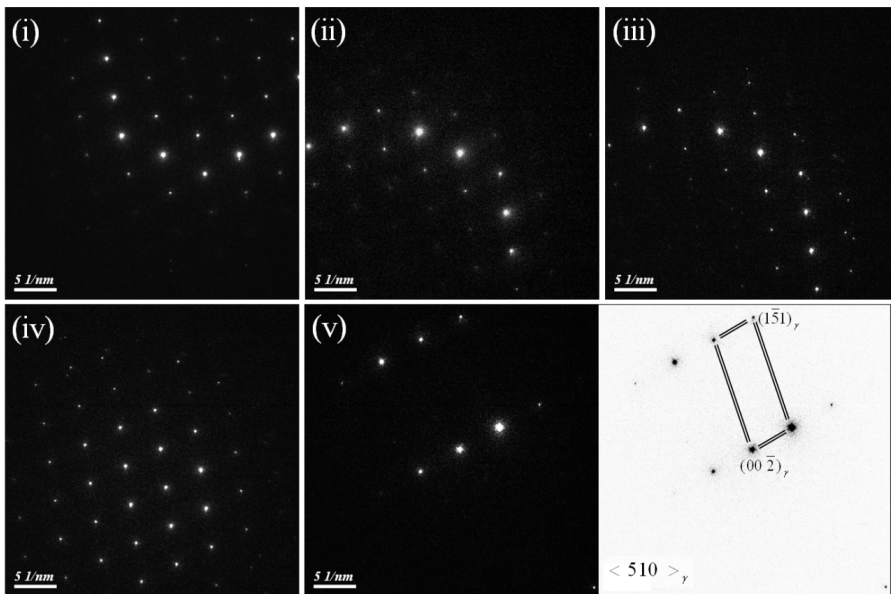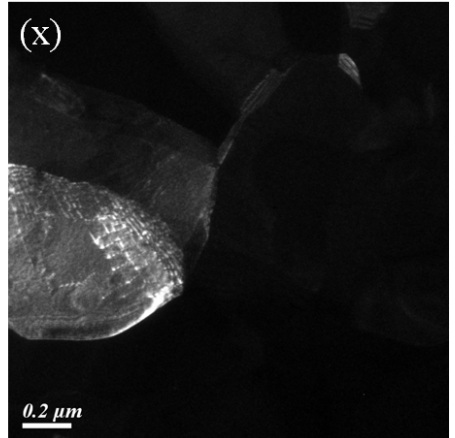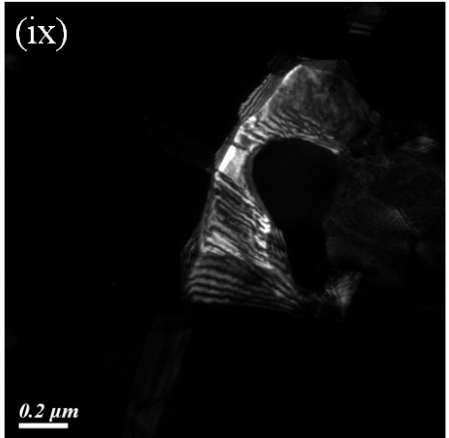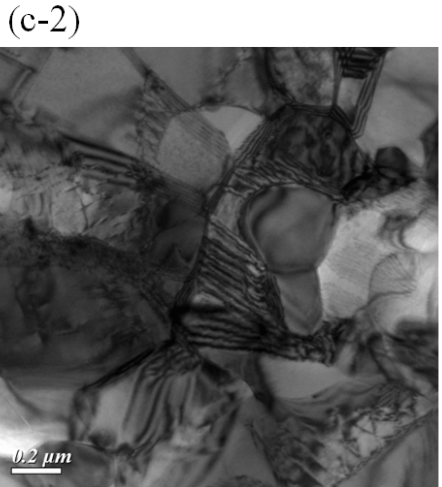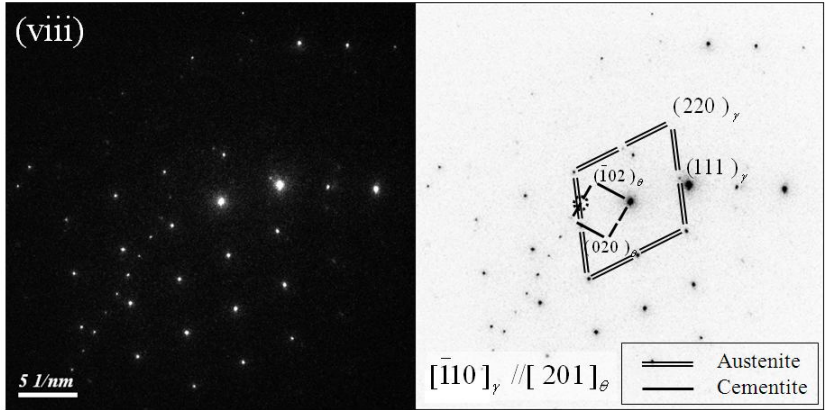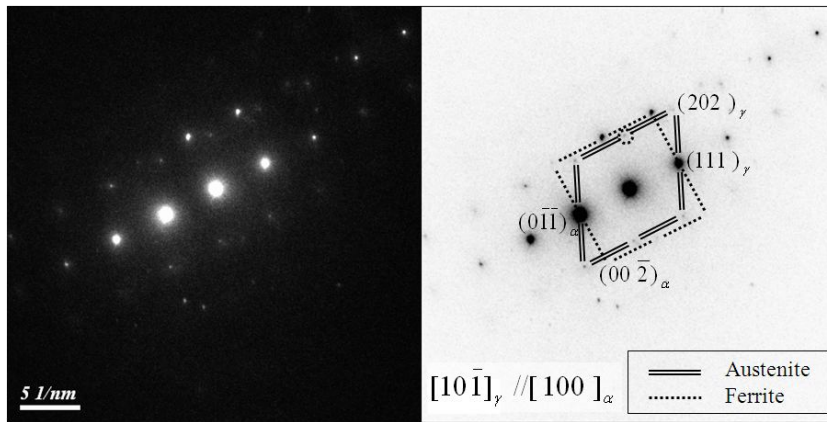
Fig. V.7 Bright field, dark field images and diffraction patterns of the three regions of 1-400h in Fig. V.5. The selected area aperture was placed at the interface between austenite and cementite for (a) and (b). The dark field images of austenite and cementie are shown in (a,i), (b,i) and (a,ii), (b,ii), respectively. (a) did not show any recognizable orientation relationship and (b) showed Pitsch-Petch orientation relationship. In (c-1), austenite and cementite and their interface were numbered and dark field images and diffraction patterns of corresponding regions are followed. Diffraction patterns of each region which were obtained without tilting are followed. The diffraction pattern of (c.i-iv) shows austenite of which zone axis is $\{110\}_\gamma$. Austenite numbered as (c.v) had higher index zone and the index is given next to the diffraction pattern. Austenite and cementite located at the interface (c.vii) did not have any known orientation relationship. Cementite (c.vi) had same orientation as that at the interface (c.vii) having no known orientation
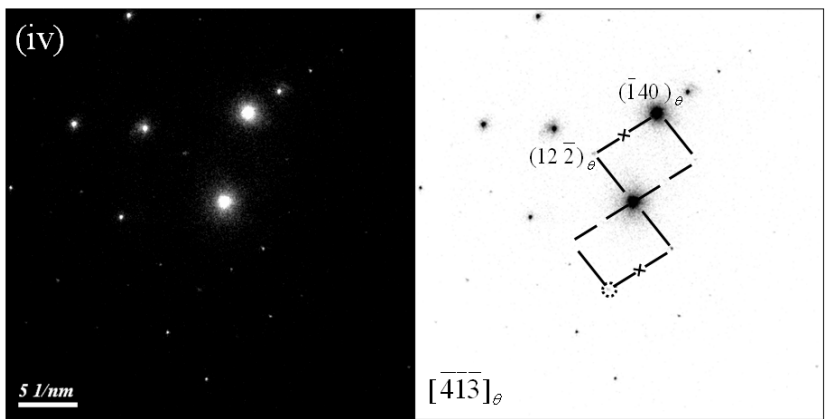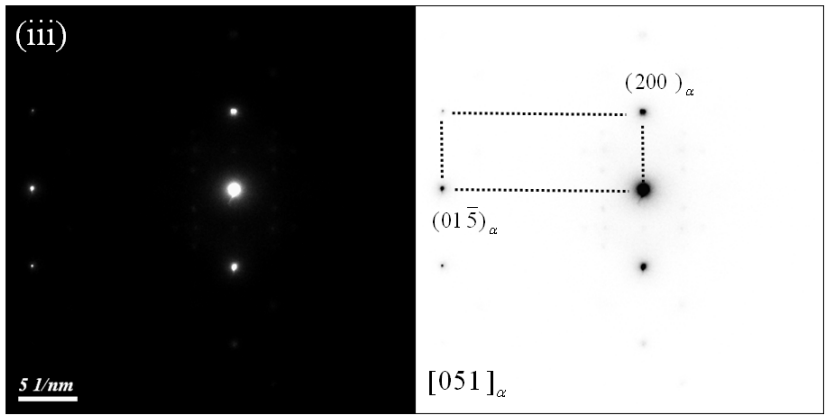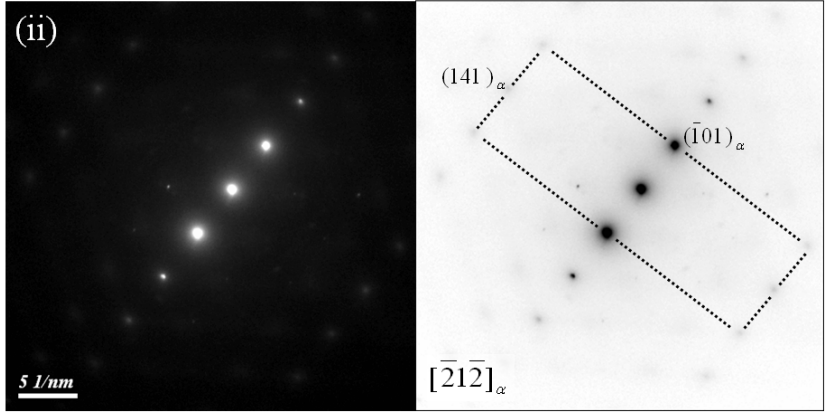
134

relationship. The interface (c.viii) shows Pitsch-Petch orientation relationship. For (c-2), the sample was tilted a little and (c.ix) and (c.x) shows the dark field image of austenite and ferrite, respectively, and the diffraction pattern of their interface is followed. They showed Nishiyama-Wasserman orientation relationship.
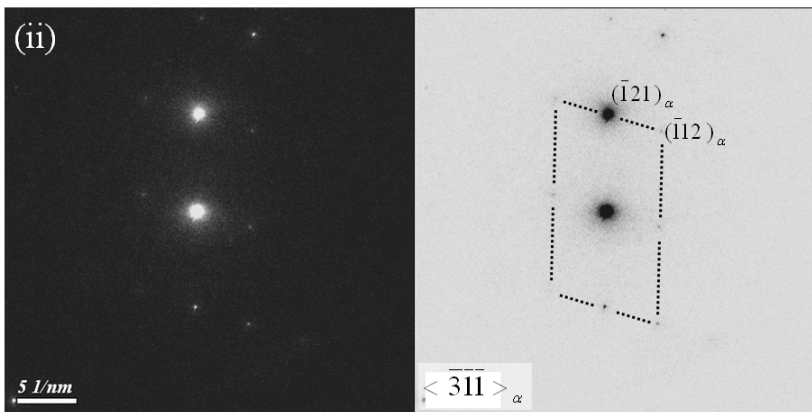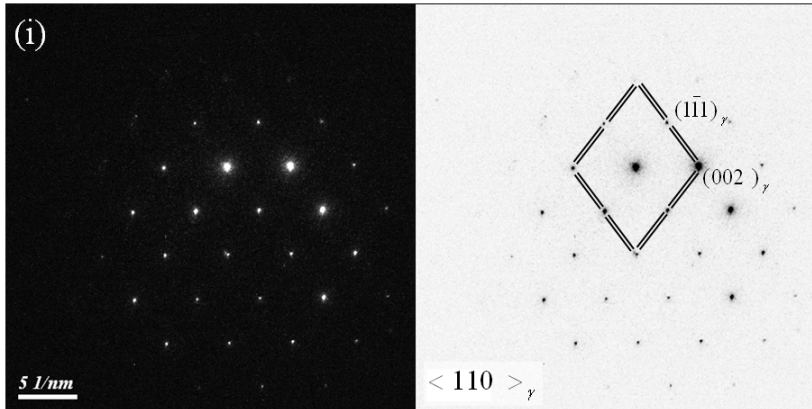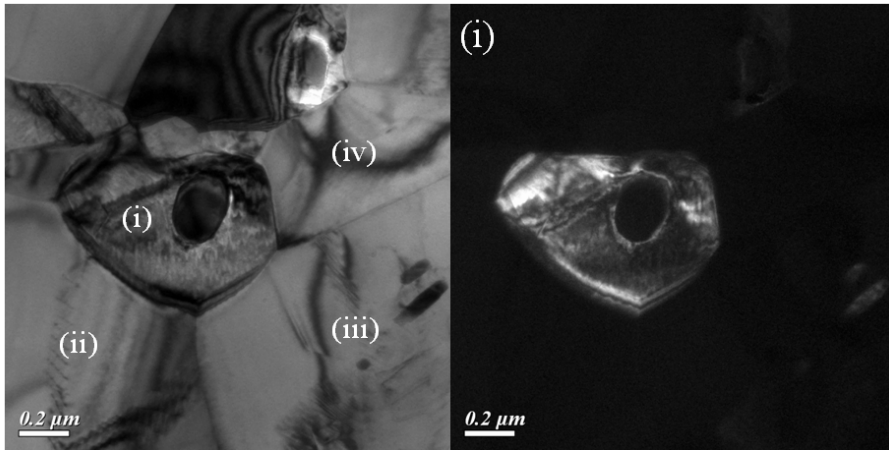
(a)

(b)

(ii)

(i)

(iv)

(iii)

0.2 μm

(i)

0.2 μm

(iv)

0.2 μm

0.2 μm

(i)

$(111)_{\gamma}$

$(020)_{\gamma}$

$[10\bar{1}]_{\gamma}$

5 1/nm
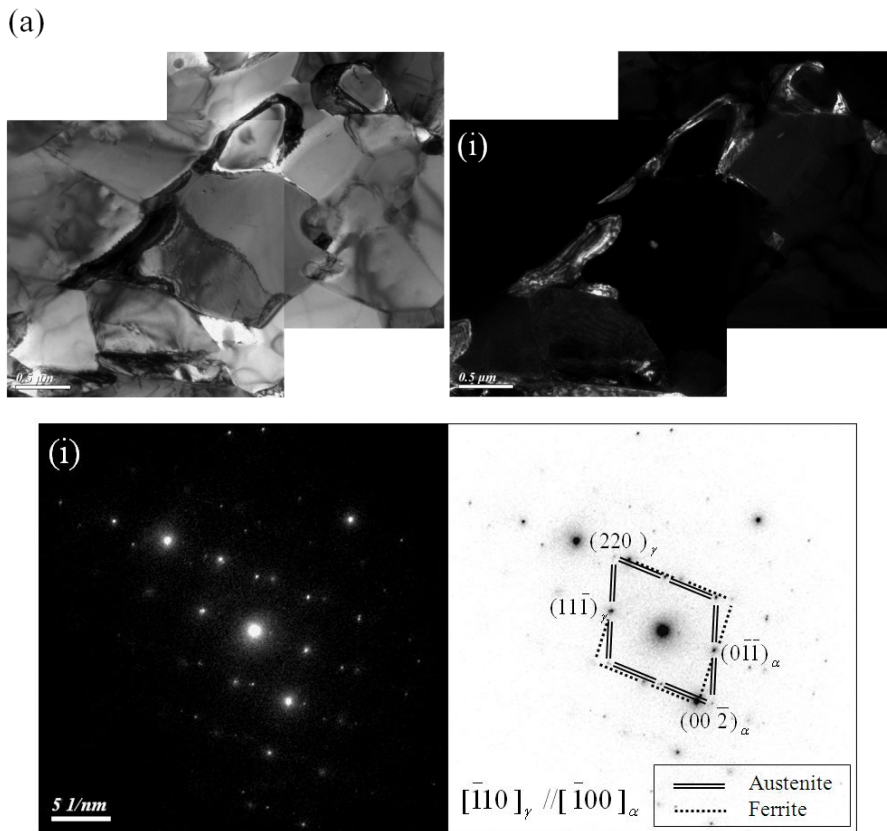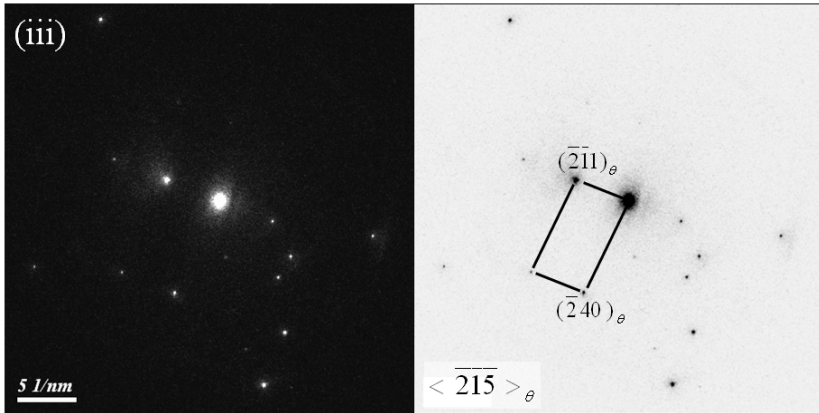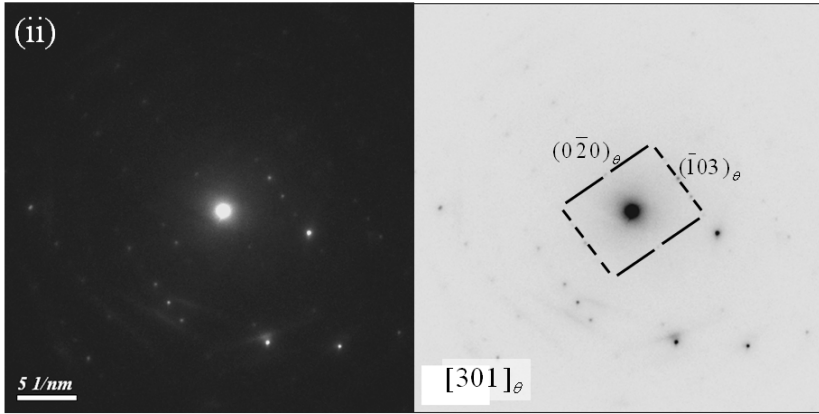
Fig. V.8 Bright field, dark field images and diffraction patterns of the three regions of 1-800h in Fig. V.6. (a.i) Austenite dark field image obtained by placing selected area aperture at the ferrite-austenite interface. It shows Nishiyama-Wasserman orientation relationship. (a.ii, i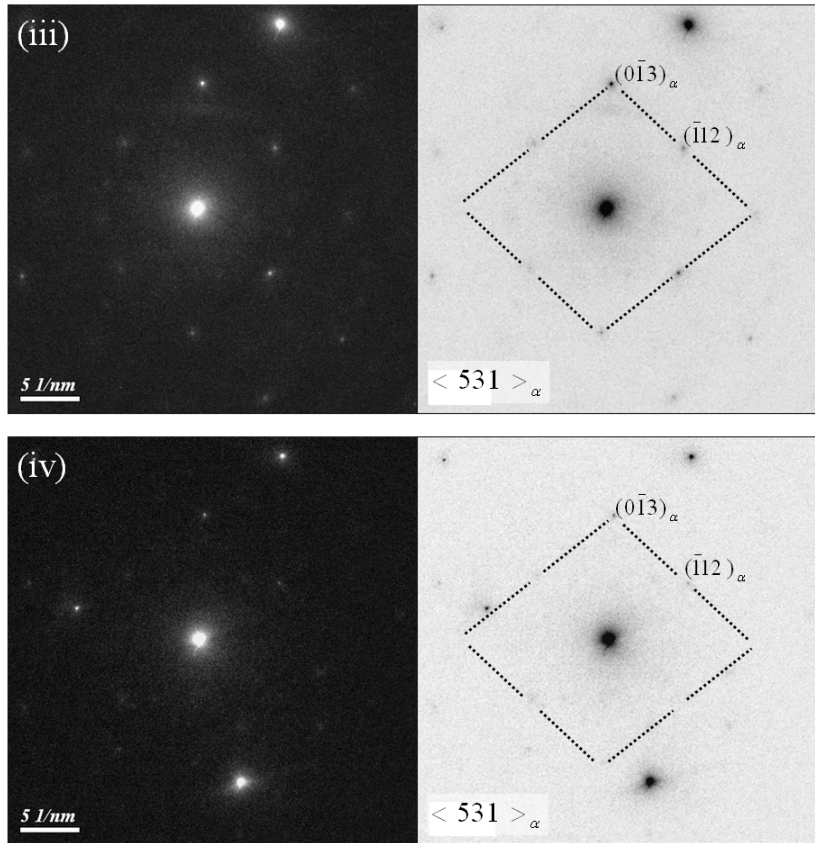ii) Cementite dark field images adjacent to the austenite. Cementite (a.ii) shows Pitsch-Petch orientation relationship with both ferrite and austenite shown in (a.i). Cementite (a.iii) does not show any known relationship with austenite. In (b), each region is designated in the bright field image. (b.i) refers to the austenite

dark field image and diffraction pattern, (b.ii, iii) to the ferrite diffraction patterns and (b.iv) to the cementite dark field image and diffraction pattern. The austenite (b.i) shows Kurdjumo-Sachs orientation relationship with ferrite (b.ii) and Nishiyama-Wasserman with ferrite (b.iii). The cementite (b.iv) shows Isaichev orientation relationship with ferrite (ii). In (c.i), the dark field image and diffraction pattern of austenite are shown. Diffraction patterns of ferrite (c.ii-iv) are also shown but did not reveal any orientation relationship with austenite (c.i).

V.2.   Alloy 2

For all samples of Alloy 2, 2-200h, 2-400h and 2-800h, the third anneal was done at 683 ℃. As in Alloy 1, the temperature was set by trial and error. The dilatation curves for each sample are given in Figs. V.9-V.11.
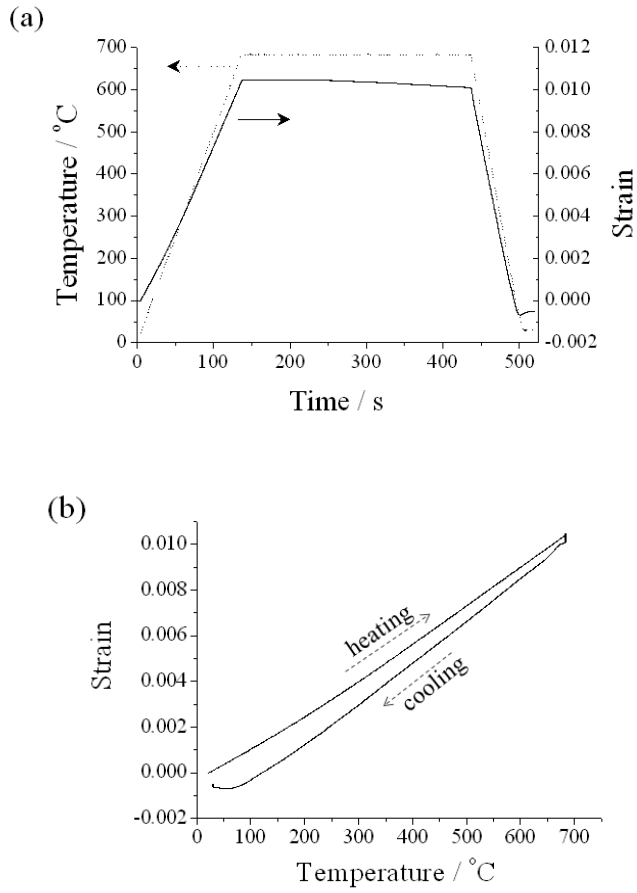
Fig. V.9   Dilatation curves of 2-200h. (a) Temperature and strain with respect

to time (b) Strain verses temperature.
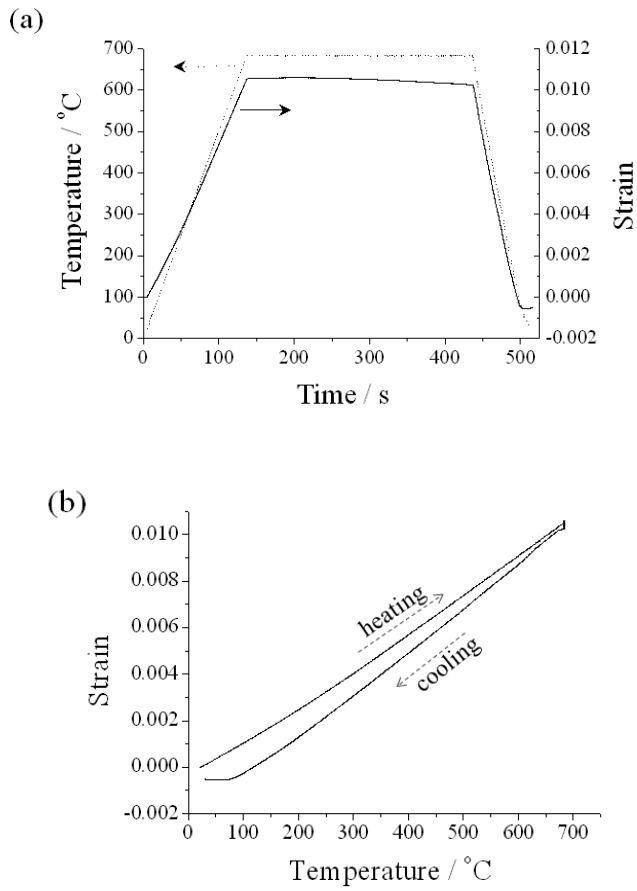
Fig. V.10 Dilatation curves of 2-400h. (a) Temperature and strain with respect to time (b) Strain verses temperature.

(a)

(b)

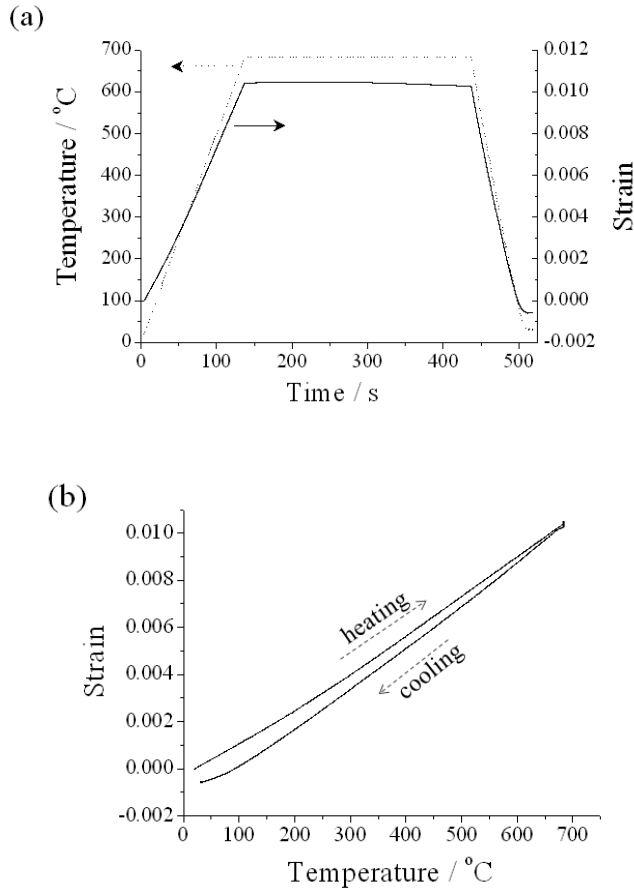Fig. V.11 Dilatation curves of 2-800h. (a) Temperature and strain with respect to time (b) Strain verses temperature.

In Figs V.9-V.11, it is seen that all the samples of Alloy 2 showed a little increase in strain for a while and then it decreased during the isothermal heating period. Moreover, equilibrium had not been reached because the strain decreased steadily. Even though the amount was small, the curve definitely

144

showed increase in strain at the last part of the cooling, which implies martensitic transformation of austenite.

All the samples of Alloy 2 had similar morphology, Figs. V.12 and V.13 with the XRD results given in Table V.4. The austenite was found to occupy 4-6 wt%, so it is difficult to distinguish it in the micrographs. However, there were some unetched islands in Fig. V.13 and these were more often observed in pearlite than in spherodite. Since austenite and martensite are the last phases to be etched with nital, these areas are thought to be martensite or austenite.

Alloy	Ferrite or martensite / wt%	Austenite / wt%	Cementite / wt%	R_{wp}	R_{exp}	χ^2
2-200h	92 ± 1	6 ± 1	2 ± 1	34.7	24.4	2.02
2-400h	91 ± 1	5 ± 1	3 ± 1	23.8	15.85	2.25
2-800h	93 ± 1	4 ± 1	1 ± 1	24.6	15.69	2.45

Table V.4 Quantitative XRD analysis results of Alloy 2 after the third anneal, using the Rietveld refinement method. The martensite structure is similar to that of ferrite, so the phases cannot be distinguished.
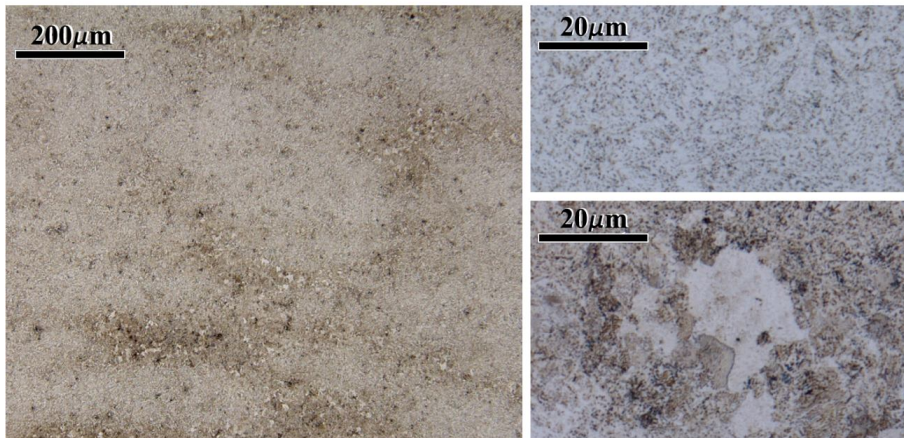
Fig. V.12 Optical micrographs of 2-200h after the third anneal (at 683 ℃ for 5 min). The sample is etched with 1 % nital. Notice the bands of different contrast parallel to the rolling direction in the left image. The upper images show different contrast regions. Upper one is spherical cementite region and the lower one is pearlitic region.
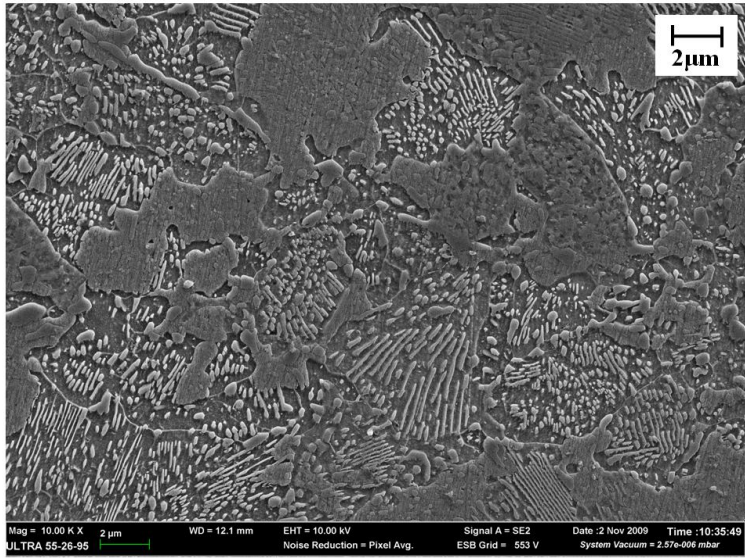
(a)
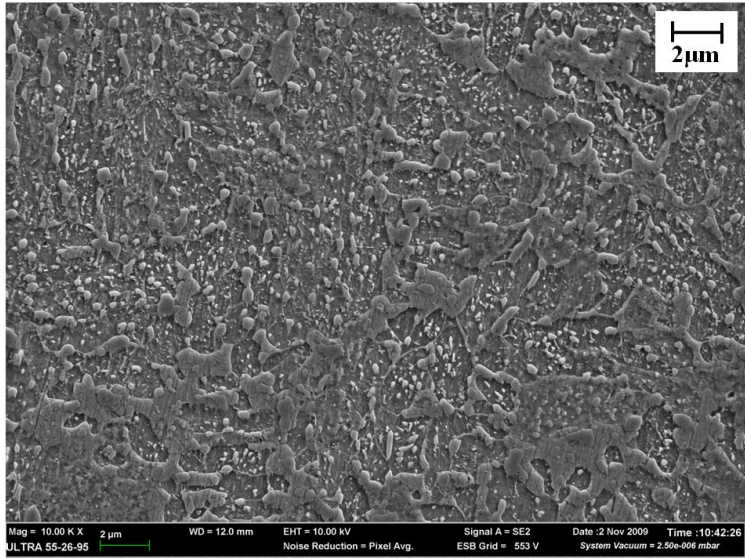
(b)

Fig. V.13 FE-SEM images of 2-800h. (a) The spheroidite region and (b) the pearlitic region in Fig. V.12.

Although the existence of austenite has been confirmed by XRD, it could not be found using TEM and instead, martensite was often seen. This martensite was presumably austenite during the third anneal, but transformed on cooling (Figs. V.14, V.16 and Table V.5). The Mn contents of all samples were between 5.5 and 6.0 wt% and they would be a little lower if C content is considered. Comparing with the result of Alloy 1, 7.4 and 7.8 wt% Mn, it is lower which seems to reduce austenite stability resulting in martensitic transformation during cooling. The lower Mn content seems to come from the lowest Mn content of cementite of Alloy 2 among three alloys after the second anneal. When reaustenitization happens, austenite seems to form at the α/θ interface since the cementite was observed near the martensite. However, the cementite was not consumed fully, because the austenite grew into ferrite grains.

Fig. V.14 Bright field images of 2-200h indicating positions where the Mn content was determined using EDS. Ferrite is indicated as α, cemenite, θ, and martensite, α'.
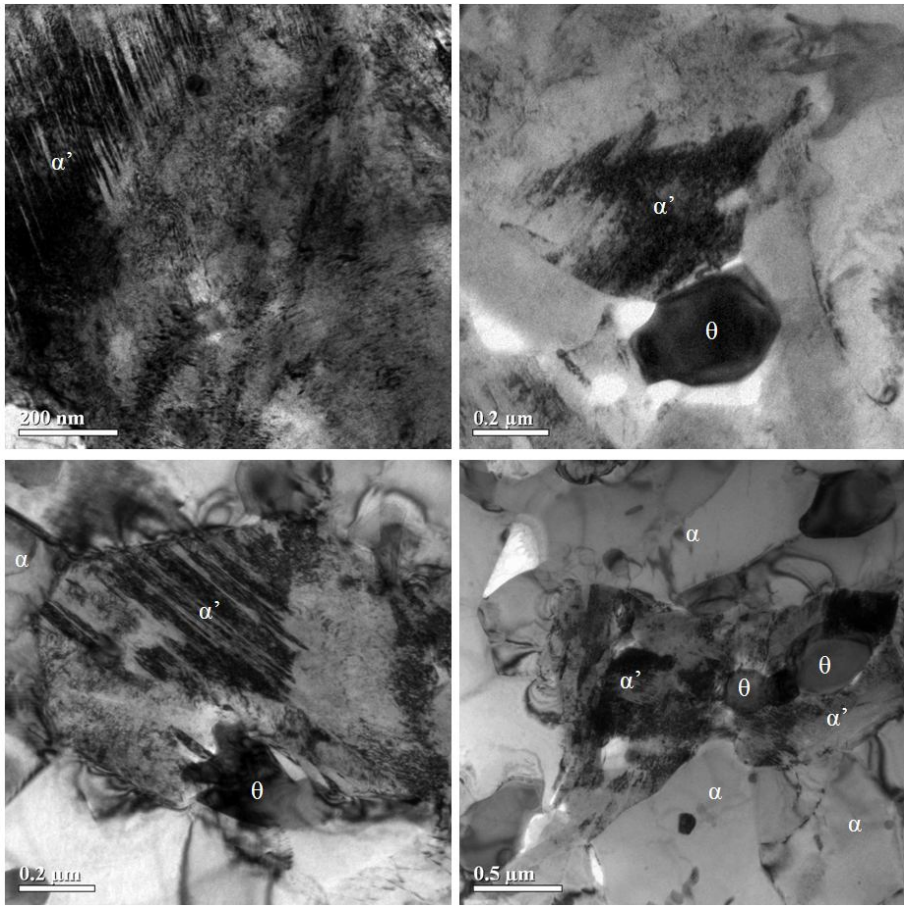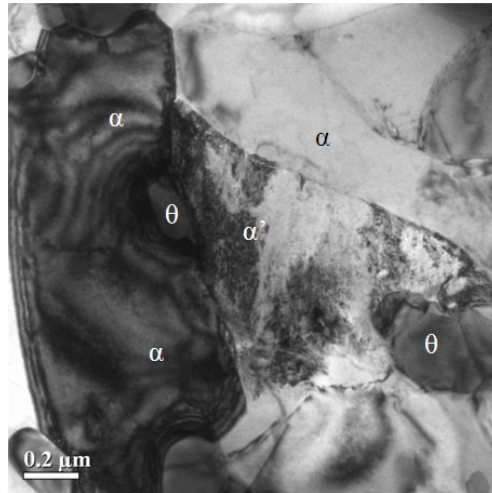
Fig. V.15 Bright field images of 2-400h indicating positions where the Mn content was determined using EDS. Ferrite is indicated as α, cemenite, θ, and martensite, α'.
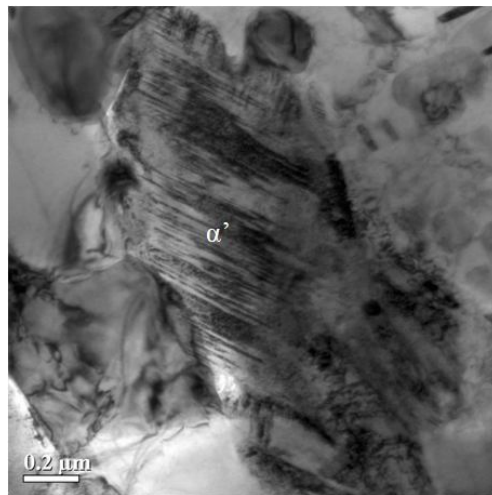
Fig. V.16 Bright field images of 2-800h indicating positions where the Mn content was determined using EDS. Martensite is indicated as α'.

Alloy	Mn content of θ / wt%	Mn content of θ considering C / wt%	Mn content of α' / wt%	Mn content of α / wt%
2-200h	22.0 ± 5.5	20.5 ± 5.2	5.8 ± 0.5	2.8 ± 0.4
2-400h	34.7 ± 3.1	32.4 ± 2.9	5.7 ± 0.9	2.8 ± 0.1
2-800h	-	-	5.6 ± 1.4	-

Table V.5 Mn content of cementite (θ) martensite (α') and ferrite (α) in Alloy 2 after the third anneal. The values in the third column were calculated by assuming 25 at% C in cementite. The Mn contents of austenite and ferrite are obtained assuming zero carbon.

Details of martensite which sometimes contains twins, are shown in Figs. V.17-V.19. The martensitic twins in Figs. V.17(a),(b) and V.19 share the same angle-axis pairs given in Table V.6. Because the region located next to the twins showed different contrast from other ferrite grains, it had been suspected to be austenite but turned out to be martensite (Fig. V.17 (c)).

(a)
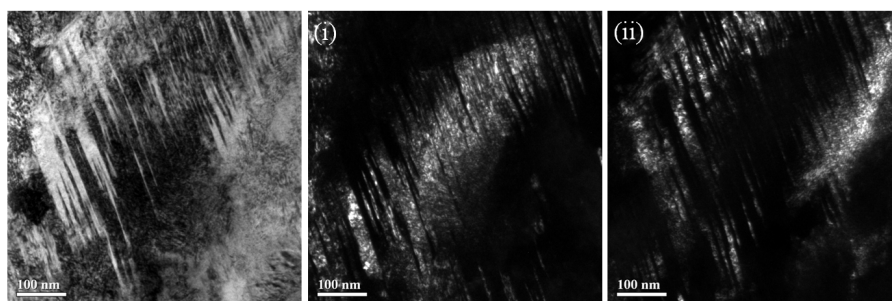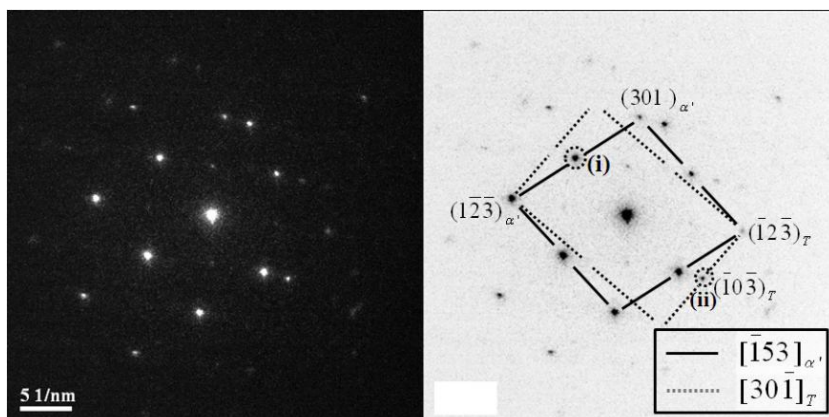
(b)
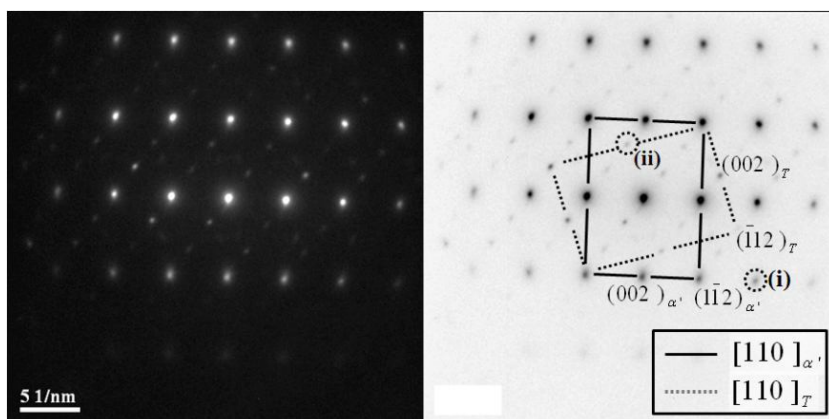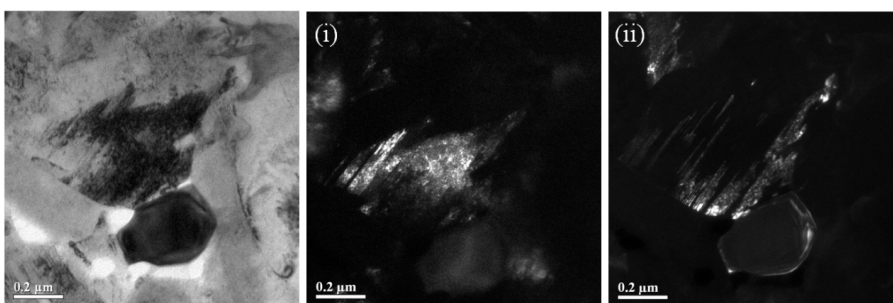
(c)
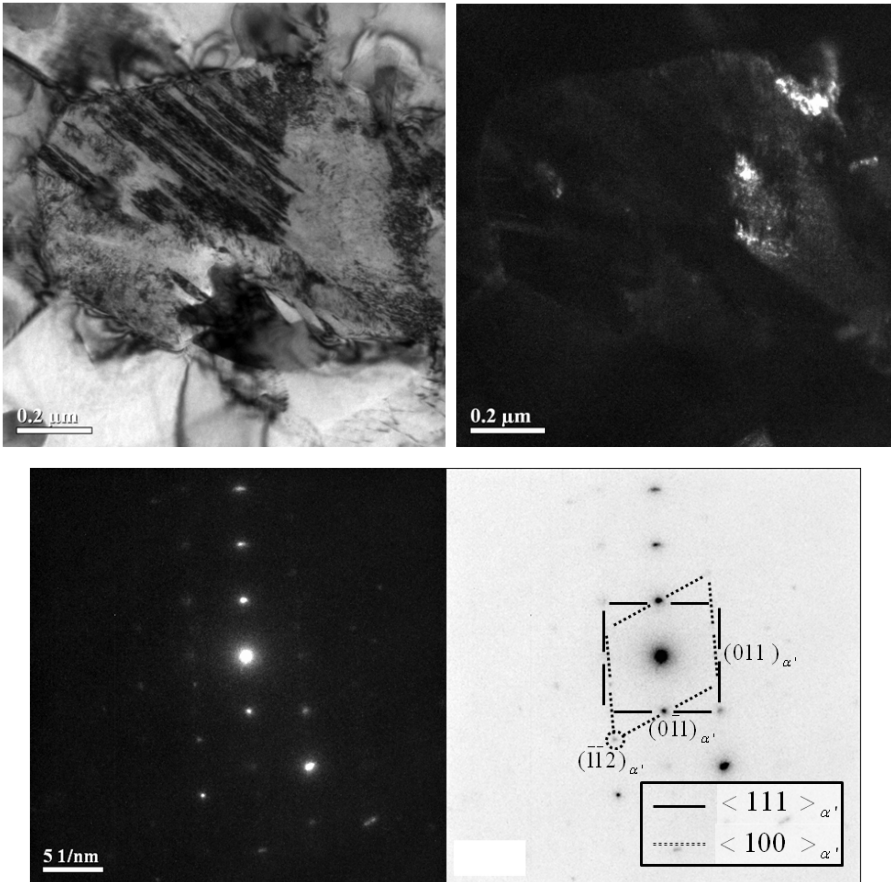
Fig. V.17 Bright field, dark field images and diffraction patterns of the three regions of 2-200h in Fig. V.14. (a) and (b) show two variants of micro-twin in martensite. The reflections for dark field images are marked with dotted circle in diffraction patterns. Corresponding reflections and dark filed images are marked by the same number. (c) shows martensite region.
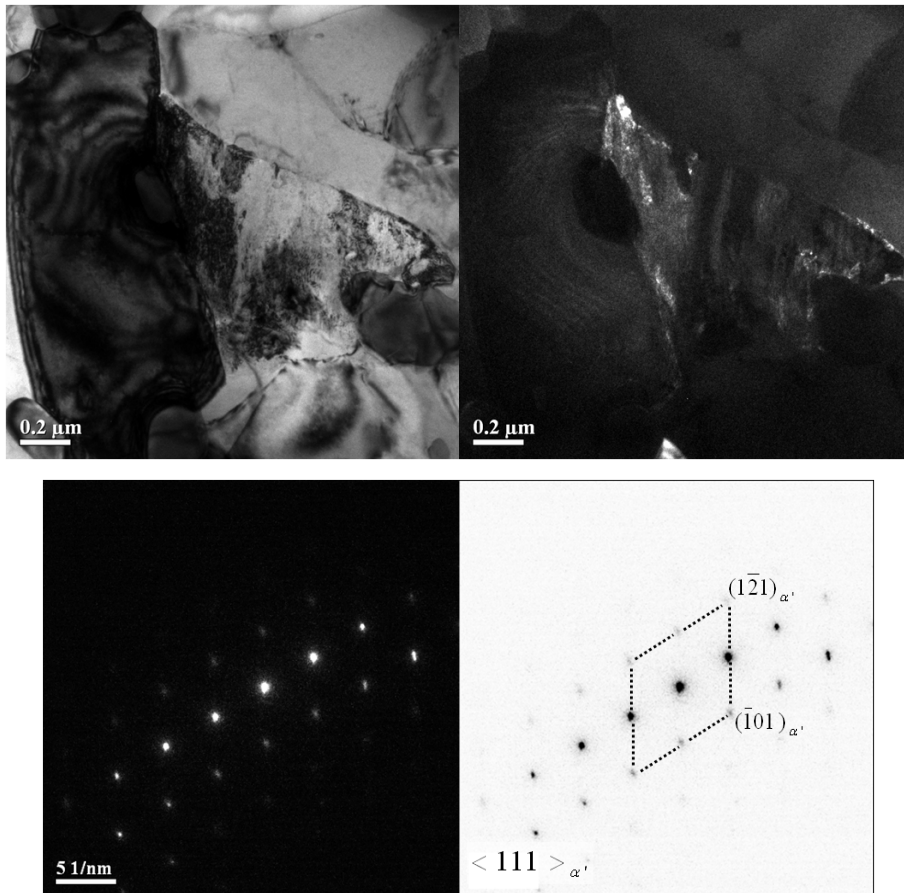
Fig. V.18 Bright field, dark field images and diffraction patterns of the regions

of 2-400h in Fig. V.15 showing martensite region.
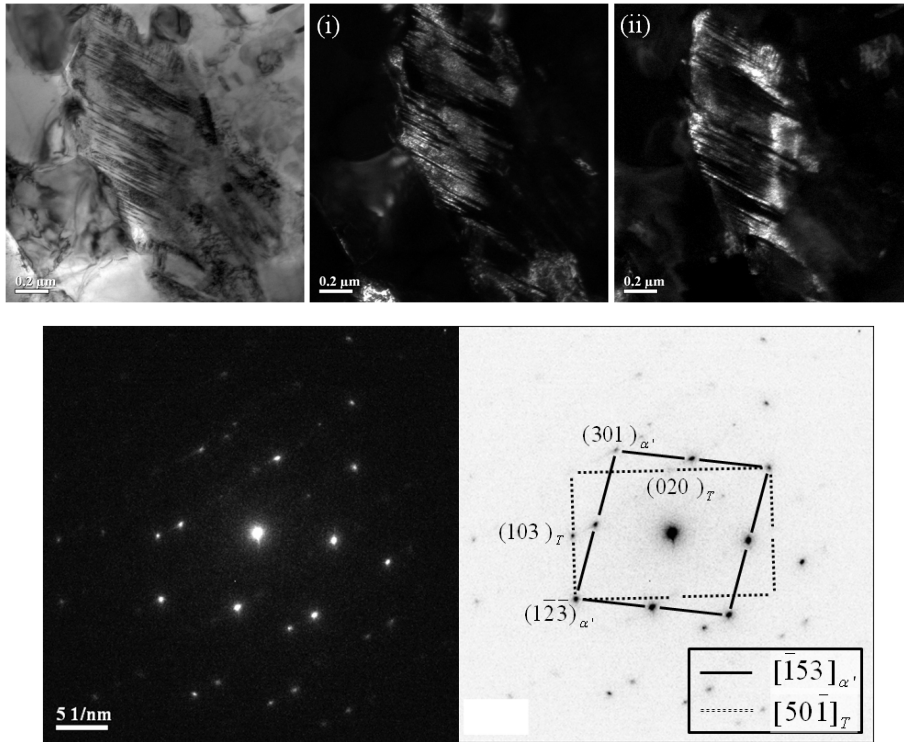
Fig. V.19 Bright field, dark field images and diffraction patterns of the region of 2-800h in Fig. V.16 showing martensite region. Two variants of the micro-twins are shown.

Index	Axis			Angle
1	-0.7071	-0.7071	0	109.5
2	0.9045	0.3015	0.3015	146.4
3	0.5773	-0.5774	0.5773	60.0
4	-0.4472	0.8944	0	131.8
5	0.4082	0.4082	0.8165	180.0
6	0	0.4472	-0.8944	131.8
7	0.8165	0.4082	0.4082	180.0
8	-0.7071	0	0.7071	70.5
9	0.7071	0.7071	0	70.5
10	-0.3015	-0.3015	-0.9045	146.4
11	0.3015	-0.9045	-0.3015	146.4
12	0.5774	0.5774	0.5773	180.0
13	0	-0.7071	-0.7071	70.5
14	0.8944	-0.4472	0	131.8
15	-0.8944	0	-0.4472	131.8
16	-0.3015	-0.3015	0.9045	146.4
17	0.3015	0.9045	-0.3015	146.4
18	0	0.7071	0.7071	109.5
19	0.4082	0.8165	0.4082	180.0
20	0.4472	0	0.8944	131.8
21	0	-0.8944	0.4472	131.8
22	-0.5774	0.5773	-0.5773	60.0
23	-0.9045	0.3015	0.3015	146.4
24	0.7071	0	-0.7071	109.5

Table V.6   24 equivalent axis-angle pairs relating twins in martensite.

V.3. Alloy 3

The third anneal temperature was set to be 638 ℃ for 3-200h and 3-400h and the dilatation curves are given in Figs. V.20 and V.21.
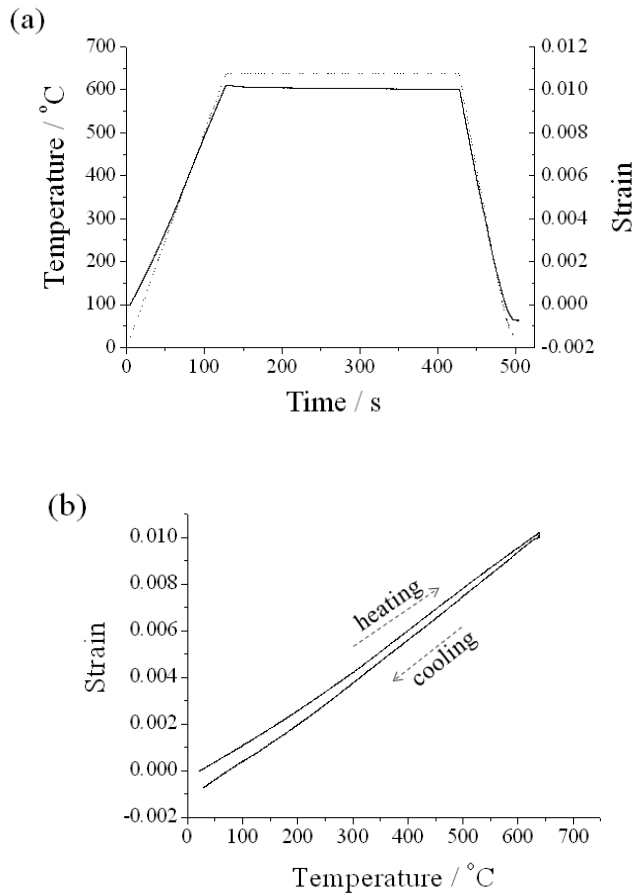
Fig. V.20 Dilatation curves of 3-200h. (a) Temperature and strain with respect to time (b) Strain verses temperature.
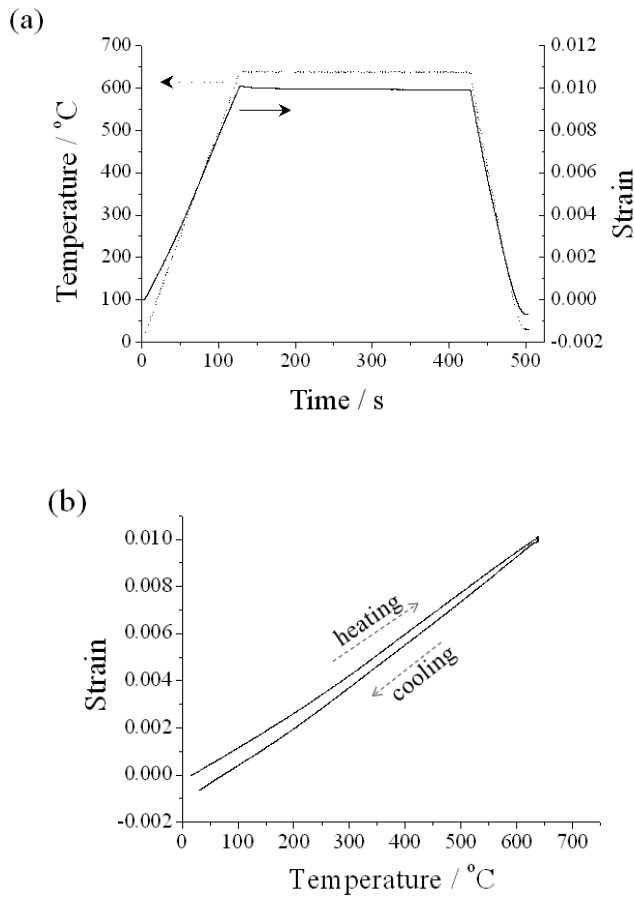
Fig. V.21 Dilatation curves of 3-400h. (a) Temperature and strain with respect to time (b) Strain verses temperature.

It is seen that the decrease in transformation strain has been retarded during isothermal heat treatment. The rate of this became lower than that of Alloys 1 and 2, which implies that Alloy 3 reached closer to the equilibrium. Moreover, martensite transformation occurred during cooling as indicated by

the curvature change during cooling (Figs. V.20(b) and V.21(b)).

Morphology of 3-200h and 3-400h were similar and representative optical micrographs are presented in Fig. V.22. Also, XRD results are shown in Table V.7 and two samples had almost the same austenite amount, 8-9 wt%. It contained large islands which consisted of austenite with martensite. The matrix was pearlite and the darker region around the islands was composed of deeply etched pearlite. Some of the pearlitic regions have transformed into austenite then the austenite have transformed into martensite during cooling. The regions contain martensite and austenite are so large that it can be clearly seen by OM. However, there is a possibility of small austenite formed in the pearlite that cannot be seen. Moreover, the martensite structure was obtained by SEM and shown in Fig. V.23. Even though it may look like the ferrite which was seen after the second anneal (Fig. IV.22(a)), martensite can be differentiated from ferrite by its protruding structure when etched with nital. Fig. V.23 contains martensite which is embedded in pearlite and also surrounds small pearlitic colony. From martensite morphology of selective pearlitic colony consumption, the austenite seems to have consumed pearlite colonies one by one during isothermal heating.

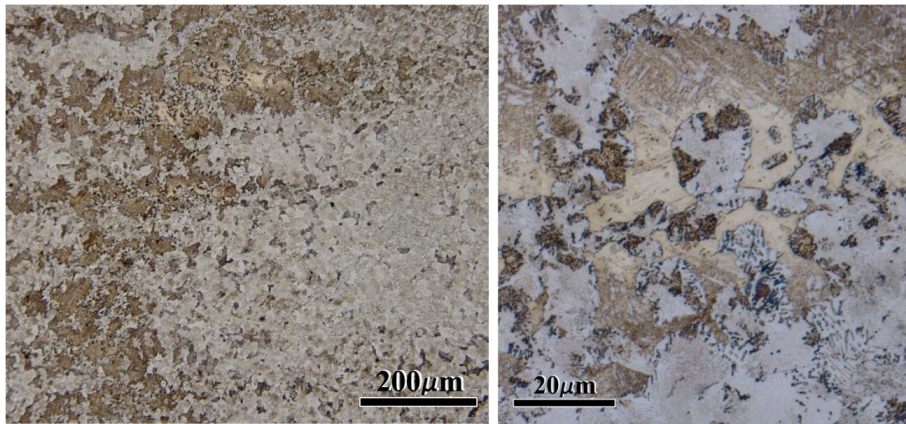Fig. V.22 Optical micrograph of 3-200h after the third anneal (at 638 ℃ for 5 min). The sample is etched with 1 % nital. Notice the long islands parallel to the rolling direction in the left image. The right is the magnified image of the islands.
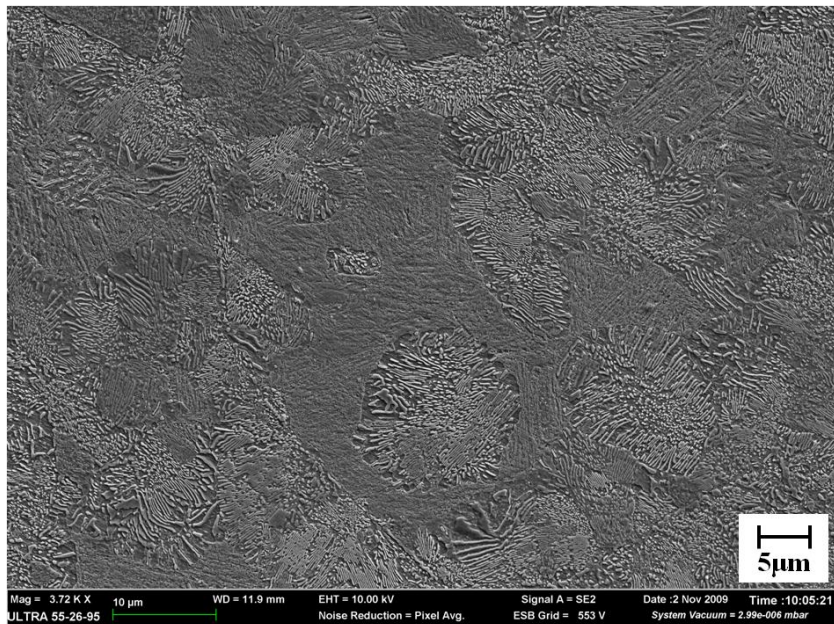
Fig. V.23 FE-SEM images of 3-200h.

Alloy	Ferrite or martensite / wt%	Austenite / wt%	Cementite / wt%	R_{wp}	R_{exp}	χ^2
3-200h	89 ± 1	9 ± 1	2 ± 1	25.1	16.11	2.42
3-400h	91 ± 1	8 ± 1	1 ± 1	31	16.12	3.69

Table V.7 Quantitative XRD analysis results of Alloy 3 after the third anneal, using the Rietveld refinement method. The martensite structure is similar to that of ferrite, so the phases cannot be distinguished.

TEM was adopted for more details of austenite morphology and its Mn content (Figs. V.24 and V.25). In order to reduce ambiguity dark field images and diffraction patterns are also shown with the bright field images, together with EDS line scans (Figs. V.26-V.29).

One region had small austenite particles formed at the end of the pearlite colony boundary creating two α/γ and one γ/θ interfaces (Fig. V.24(a)). Another case shows the possibility of austenite formation at the corner of pearlite colonies where three of them meet together (Fig. V.25(d)). The austenite then seems to have grown along the colony boundaries. The two regions shown in Figs. V.24(c) and V.25(a) consist of large austenite grains which seem to have consumed a single pearlite colony. The Mn contents of these austenitic regions were analyzed separately by EDS. In Fig. V.24(c), while upper part was almost fully austenitic, the lower part had austenite surrounding cementite. For the upper part in Fig. V.24 where large austenite

was seen, the Mn content was 9.1 ± 2.0 wt%. The austenite shown in Fig. V.25(a) had an unusual morphology and gave a Mn content of 7.6 ± 1.6 wt%.

All line scan results showed a discrete step at the α/γ and γ/θ interfaces. Thus, different phases can be identified with EDS data. However, despite the high Mn content of the cementite, the austenite had Mn content lower than 10 wt%.

Since the Mn contents of small austenite particles and large austenite region showed similar values, all EDS data from line and point scans are given in Table V.8. It is seen that the average values of Mn content of cementite, austenite and ferrite were lower in 3-400h than in 3-200h. However, since 3-200h showed large standard deviation, it is concluded that two alloys showed similar values within the error range. Moreover, the C content in Table V.9 shows that austenite C content is much lower than that of cementite and even lower than the overall C content.

Among all the austenite under analysis, two showed an unknown structure within the austenite (Figs V.24(d) and V.25(d)), consisting of thin parallel pairs of plates which were possibly associated with stacking faults.

The orientation relationships among the phases vary although their differences may be due to experimental error in the diffraction patterns. For

the phases in Fig. V.25(e), ferrite had Nishiyama-Wasserman orientation relationship with austenite and Bagaryatski or Isaichev with cementite, but austenite and cementite did not have any known relationship. The Nishiyama-Wasserman between austenite and ferrite was also observed in Fig. V.25(b) and this region can be also matched with Kurdjumo-Sachs. Besides, there was austenite that had no known orientation relationship with any adjacent phases (Figs. V.24(b) and V.25(c)).

(ii)

5 1/nm

$(0\bar{2}2)_\gamma$

$(\bar{1}11)_\gamma$

$(101)_\alpha$

$(002)_\alpha$

$< 211 >_\gamma \,//\, < 0\bar{1}0 >_\alpha$

	Austenite
	Ferrite

(iii)

5 1/nm

$(\bar{2}2\bar{2})_\theta$

$(1\bar{1}\bar{1})_\gamma$

$< 211 >_\gamma \,//\, < 32\bar{1} >_\theta$

	Austenite
	Cementite

(iv)

5 1/nm

$(\bar{2}2\bar{2})_\theta$

$(\bar{1}0\bar{3})_\theta$

$(101)_\alpha$

$(002)_\alpha$

$[0\bar{1}0]_\alpha \,//\, [32\bar{1}]_\theta$

	Ferrite
	Cementite
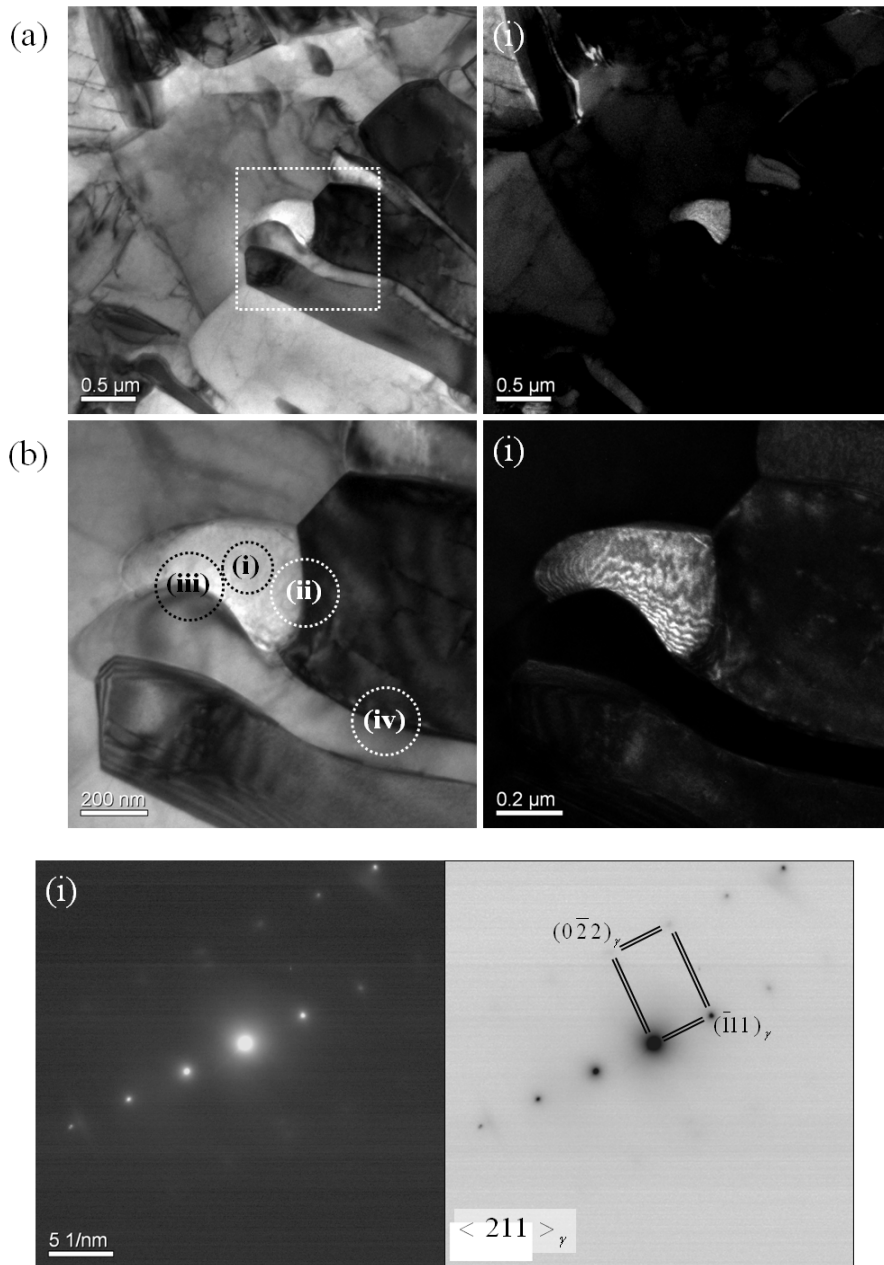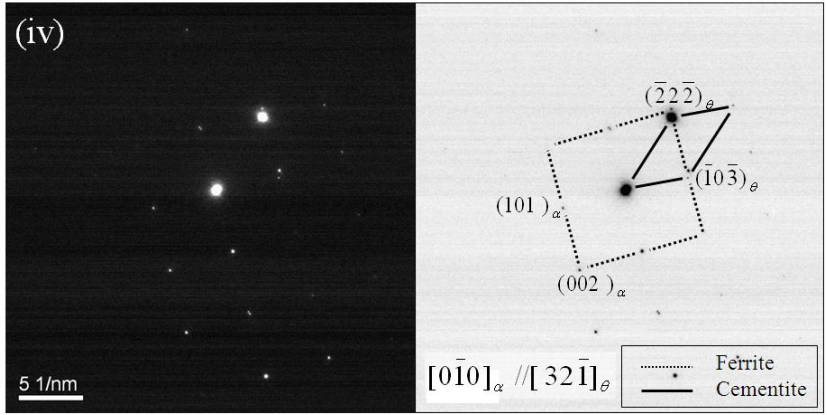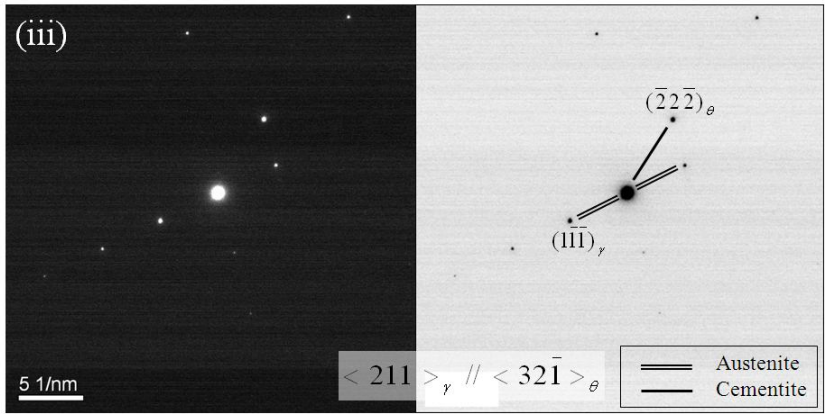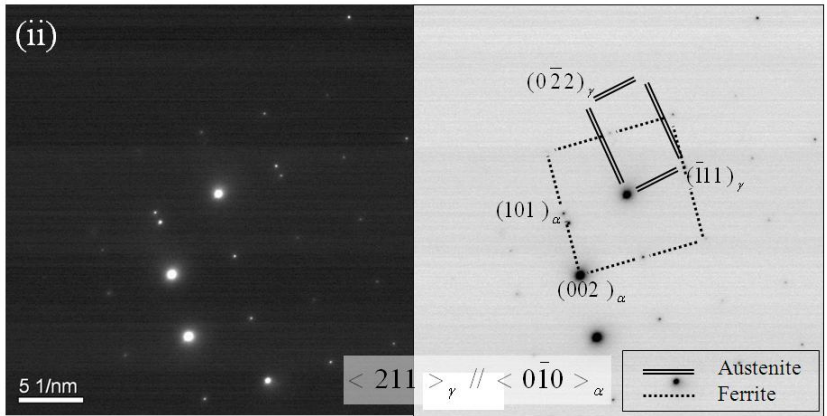
(c)

(d)

Fig. V.24 Bright field, dark field images and diffraction patterns of the austenite regions of 3-200h. (b) is a magnified image of the region shown in (a). Both dark field images in (a) and (b) shows austenite. The regions shown in bright field image of (b) and corresponding diffraction patterns are designated by same number. (b.i) Austenite. (b.ii) α/γ interface. (b.iii) γ/θ interface. (b.iv) α/θ interface. All diffraction patterns were obtained together without tilting. Both diffraction patterns (b.ii) and (b.iii) show no known orientation relationship while diffraction pattern (b.iv) shows Isaichev orientation relationship. The dark field image in (c) shows austenitic region and the corresponding austenite diffraction pattern is given. (d) The magnified image of the region marked in (c).

(a)

1 µm

1 µm

1 µm

(b)

0.5 µm

0.5 µm

(d)

(e)

(i) $[10\bar{1}]_\gamma$ — $(202)_\gamma$, $(111)_\gamma$

(ii) $[100]_\alpha$ — $(011)_\alpha$, $(00\bar{2})_\alpha$
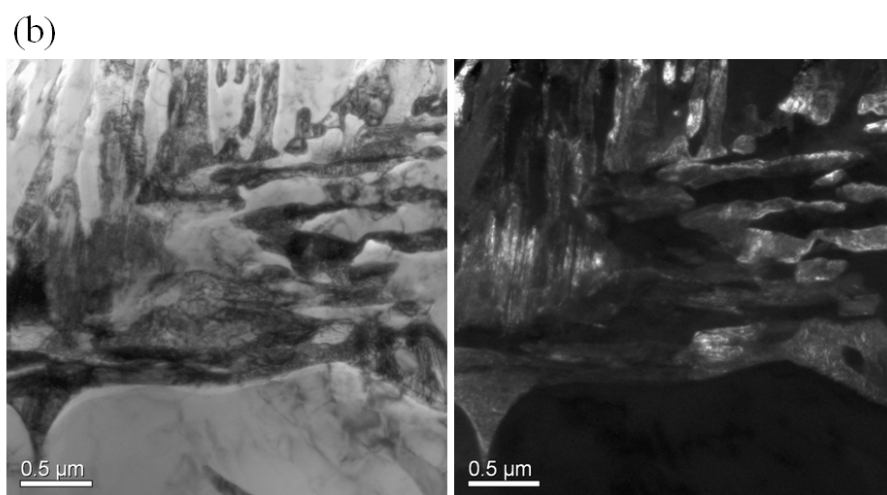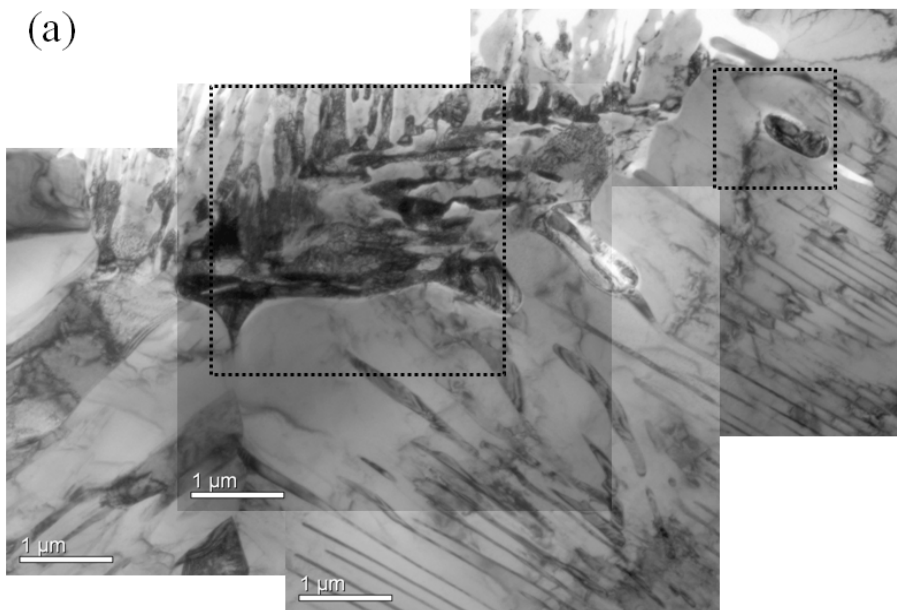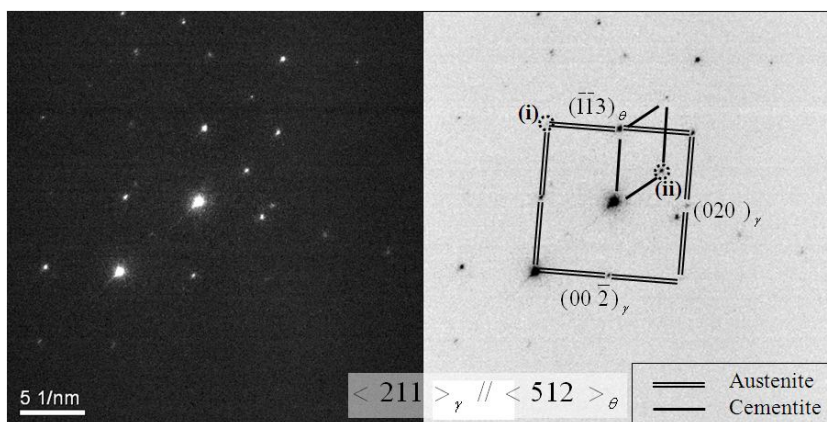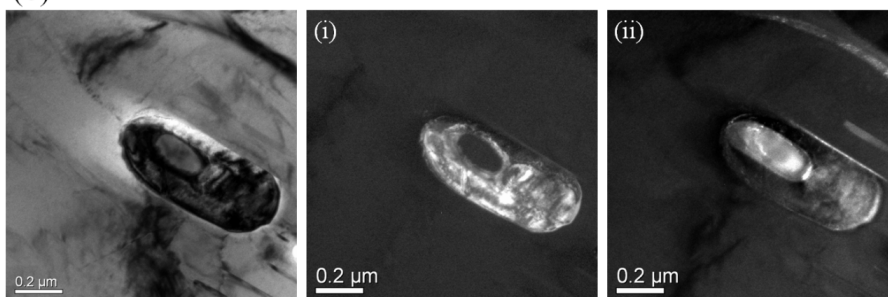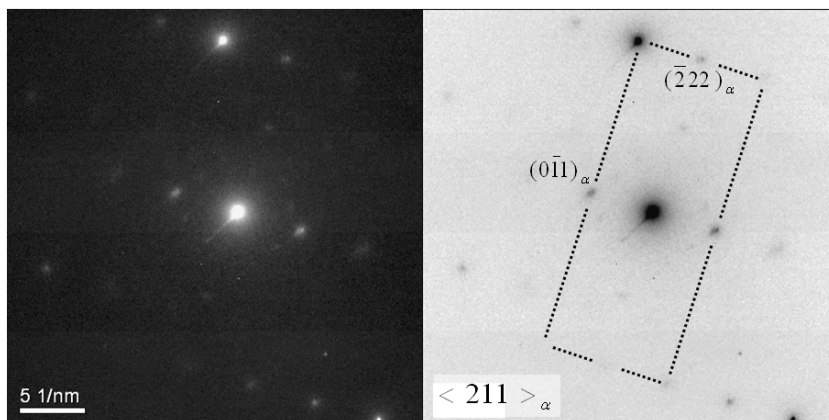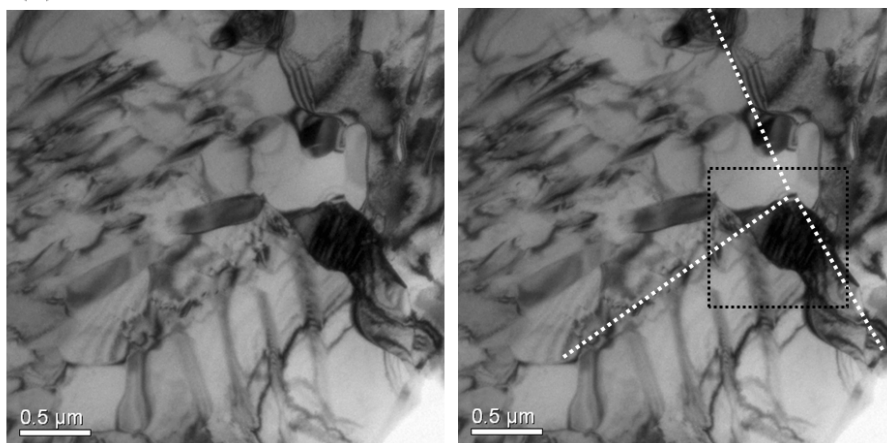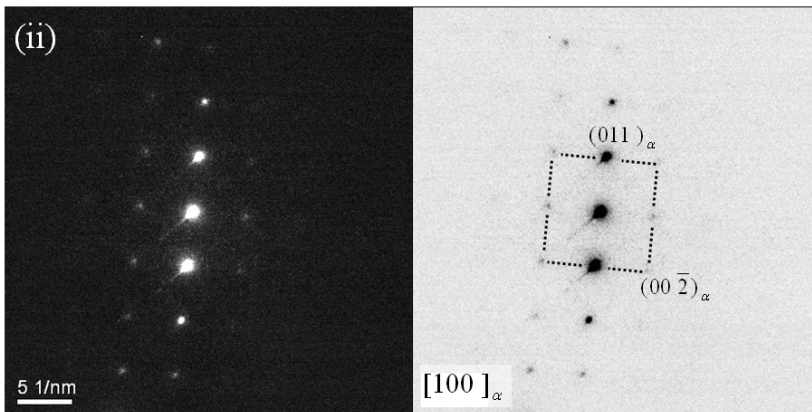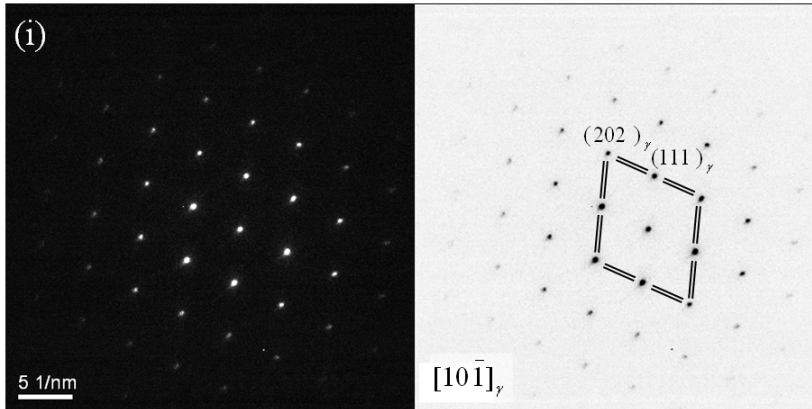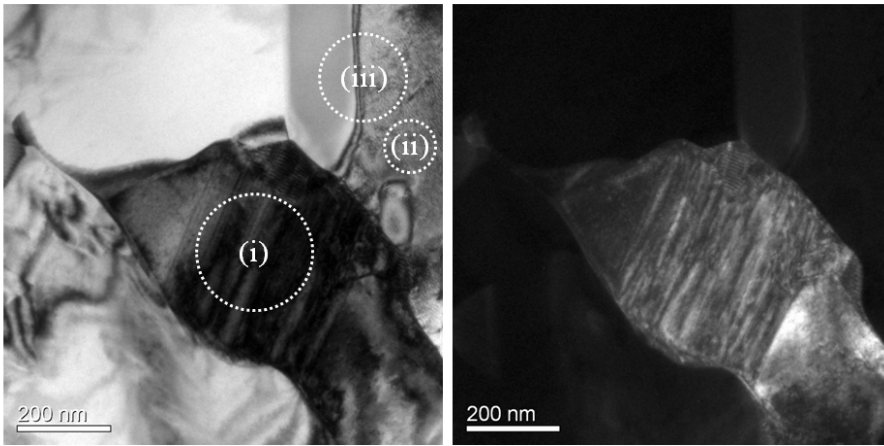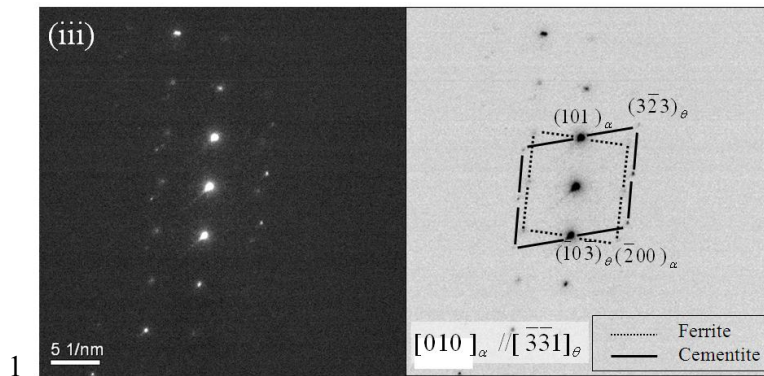
Fig. V.25 Bright field, dark field images and diffraction patterns of the austenite regions of 3-400h. The two regions enclosed by dotted rectangle were magnified into (b) and (c). In (b), the dark field image of austenite is shown and the diffraction pattern represents orientation relationship which fits into both Nishiyama-Wasserman and Kurdjumo-Sachs with ferrite. In (c), the dark field image (i) is of austenite and (ii) is of cementite. Corresponding reflections ar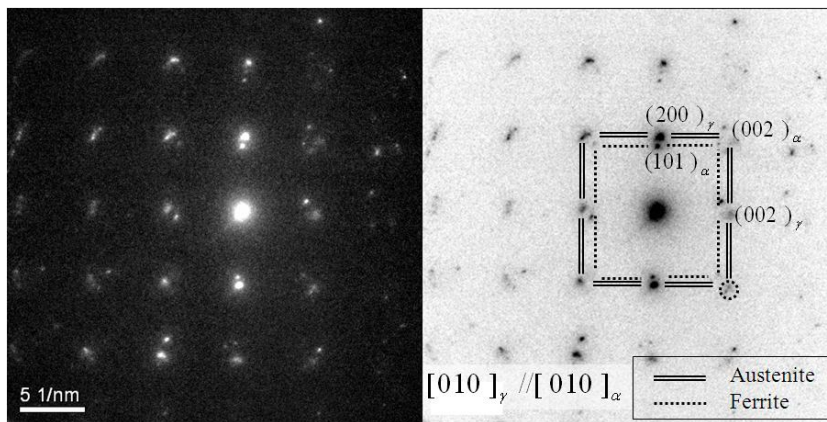e shown in dotted circle in following diffraction patterns. Last diffraction pattern in (c) is of ferrite not showing any known orientation relationship with each other. (d) Austenite region in which pearlite colony boundaries are indicated by dotted lines. (e) The magnified image of the marked region in (d). The regions shown in the bright field image of (e) and corresponding diffraction patterns are designated by same number. (d.i) Austenite. (d.ii) Ferrite. (d.iii) α / θ interface. All diffraction patterns were obtained together without tilting. Austenite shows Nishiyama-Wasserman and cementite shows Bagaryatski or Isaichev with ferrite.
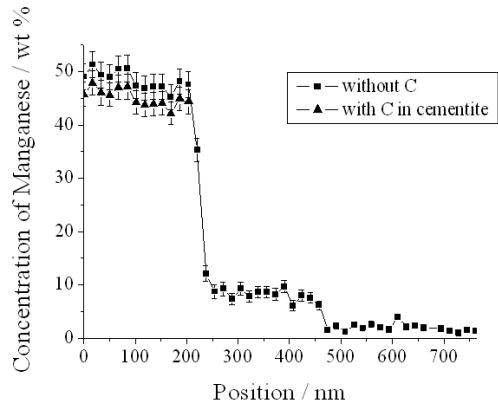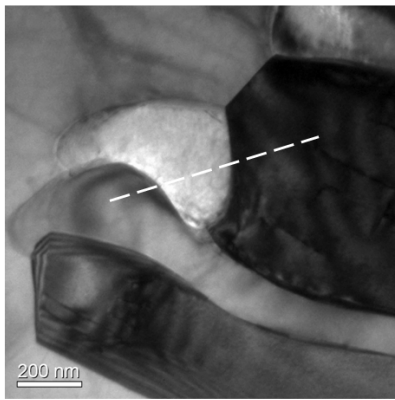
Fig. V.26 EDS line scan results of 3-200h shown in Fig. V.24(b). For cementite region, additional data which were calculated by assuming 25 at% C were provided in the plot.

(a)

(b)
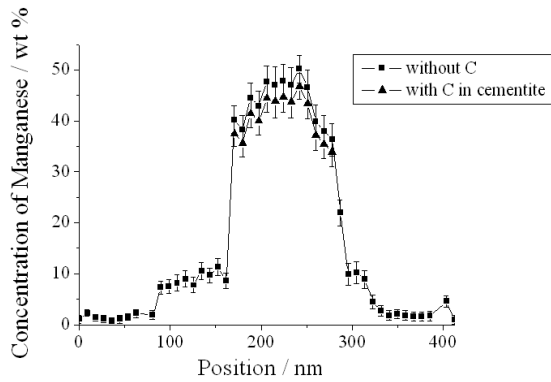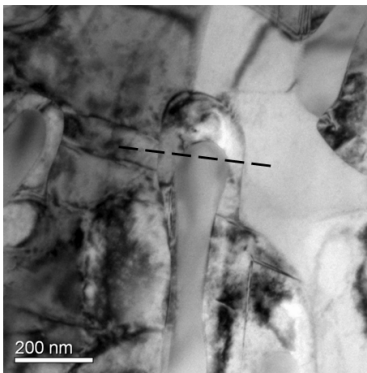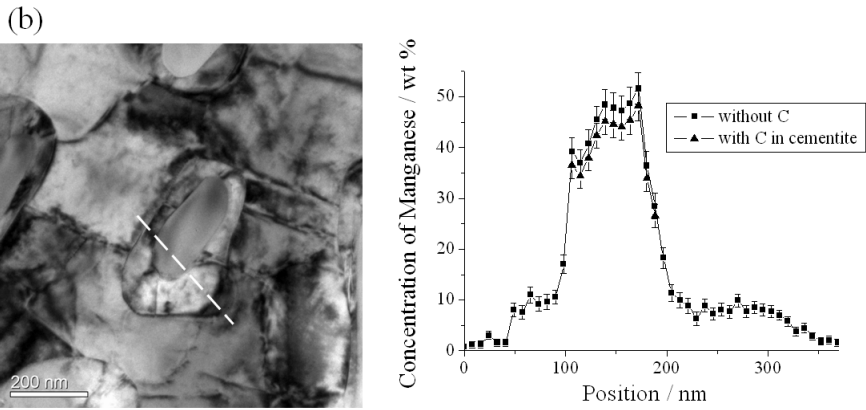
Fig. V.27 EDS line scan results for two regions in 3-200h shown in Fig. V.24(c). For cementite region, additional data which were calculated by assuming 25 at% C were provided in the plot.
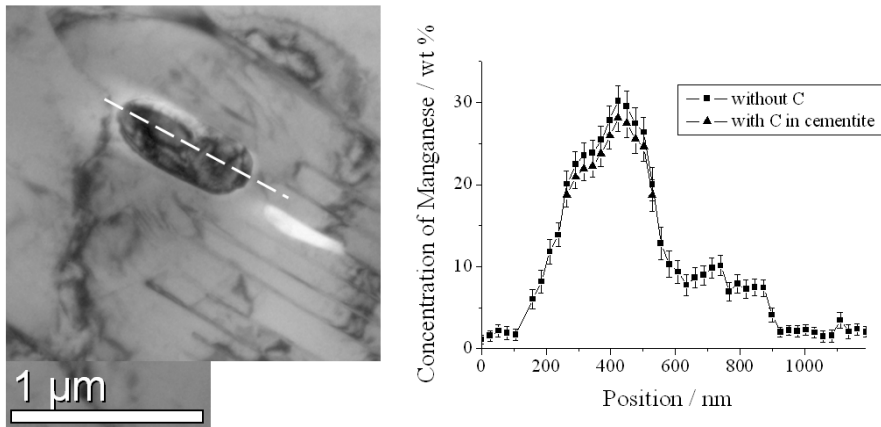
Fig. V.28 EDS line scan results of 3-400h shown in Fig. V.25(c). For cementite region, additional data which were calculated by assuming 25 at% C were provided in the plot.
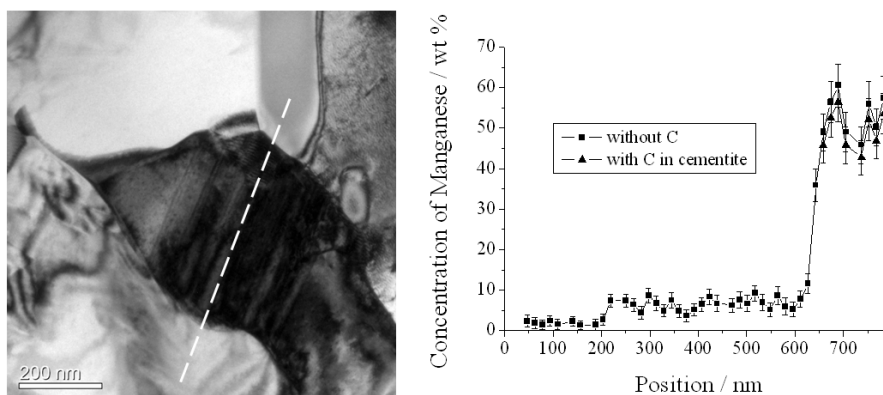
Fig. V.29 EDS line scan results of 3-400h shown in Fig. V.25(e). For cementite region, additional data which were calculated by assuming 25 at% C were provided in the plot.

Alloy	Mn content of θ / wt%	Mn content of θ considering C / wt%	Mn content of γ / wt%	Mn content of α / wt%
3-200h	46.3 ± 6.1	43.1 ± 5.7	8.8 ± 1.6	2.0 ± 1.0
3-400h	32.6 ± 11.2	30.4 ± 10.4	7.3 ± 2.6	1.7 ± 0.6

Table V.8 Mn content of cementite (θ), austenite (γ) and ferrite (α) in Alloy 3 after the third anneal. The data were obtained from EDS line scan data (Figs V.26-V.29) and point scan data in Fig. V.25 (b). The values in the third column were calculated by assuming 25 at% C in cementite. The Mn contents of austenite and ferrite are obtained assuming zero carbon.

175

Alloy	Lattice parameter of γ / Å	C content of γ / wt%	Mn content of γ / wt%
3-200h	3.59852 ± 0.00058	0.369 ± 0.064	8.8 ± 1.6
3-400h	3.59933 ± 0.00070	0.437 ± 0.096	7.3 ± 2.6

Table V.9 C and Mn content of austenite (γ) in Alloy 3 after the third anneal. The C content is considered for acquiring Mn content. The lattice parameters of γ obtained by XRD analysis and Mn contents given Table V.8 were used to calculate C contents.

V.4. Discussion

All analysis results of austenite are shown together with calculated equilibrium values in Table V.10. The mass percent of austenite was very much lower than equilibrium implying equilibrium has not yet reached. However, the Mn and C concentration in austenite were similar to the equilibrium values.

Alloy	Mass percent of austenite		Mn content of austenite / wt%		C content of austenite / wt%	
	Equilibrium	Actual	Equilibrium	Actual	Equilibrium	Actual
1-400h	62	9 ± 1	7.0	7.4 ± 0.6	0.40	0.496 ± 0.038
1-800h	62	5 ± 1	7.0	7.8 ± 0.9	0.40	0.684 ± 0.161
2-200h	99	6 ± 1	4.9	5.8 ± 0.5 (α')	0.62	-
2-400h	99	5 ± 1	4.9	5.7 ± 0.9 (α')	0.62	-
2-800h	99	4 ± 1	4.9	5.6 ± 1.4 (α')	0.62	-
3-200h	65	9 ± 1	9.0	8.8 ± 1.6	0.48	0.369 ± 0.064
3-400h	65	8 ± 1	9.0	7.3 ± 2.6	0.48	0.437 ± 0.096

Table V.10 Comparison of compositions of austenite between equilibrium and actual data after the third anneal. Actual data are obtained from XRD and EDS results (Tables V.1, V.3, V.4, V.7 and V.9). Notice that the actual Mn content data of Alloy 2 are of martensite (α') since no austenite was detected for Alloy 2.

According to Grujicic *et al.*, austenite formed at α/θ interface is expected to grow into cementite during austenitization. However, the growth is accompanied by conveying C to ferrite and stops when the C activity of ferrite is no longer lower than ($\theta + \gamma$) region (Grujicic *et al.*, 1987). In this study, it is found that the austenite growth does not occur by only consuming the cementite. Even though the austenite is likely to form at the α/θ interface and grow into cementite, ferrite should be transformed into austenite by taking in C from ($\theta + \gamma$) region. Hence, it is expected that both ferrite and

cementite have to be transformed into austenite at the same time.

Then, the problem of how much ferrite and cementite should be consumed arises. With the results obtained in this study, the fraction of ferrite and cementite transformed into austenite has been calculated by simple mass balance of alloying elements. It is assumed that the Mn and C contents in austenite come from the contributions of both phases: cementite and ferrite. Then, the following equation is obtained on the basis of mass balance:

$$f^\alpha x_C^\alpha + f^\theta x_C^\theta = x_c^\gamma \qquad \text{(Eq. V.1)}$$

$$f^\alpha x_{Mn}^\alpha + f^\theta x_{Mn}^\theta = x_{Mn}^\gamma \qquad \text{(Eq. V.2)}$$

$$f^\alpha + f^\theta = 1 \qquad \text{(Eq. V.3)}$$

where f^j is the mol-fraction of the phase j which has been incorporated in austenite, x_c^j and x_{Mn}^j are the mol-fraction of C and Mn in phase j. x_{Mn}^α and x_{Mn}^θ are calculated from the data after the second anneal (Tables IV.6 and IV.16) assuming all concentrations of alloying elements remained the same in ferrite and cementite because the third annealing period was short. It is consistent with the results that Mn concentration of cementite and ferrite after the second anneal were not different from after the third anneal. x_C^α is

set zero and x_C^θ is given 0.25. x_{Mn}^γ and x_C^γ are calculated from the data after the third anneal (Tables V.3 and V.9). All of values used are average ones. Samples of Alloy 2 were excluded because there were only martensite data and C content of martensite were unknown. Using Eq. V.1 and V.3 and Eq. V.2 and V.3, the two f^θ values were obtained. The results are shown in Table V.11. From mass balance of C (Eq. V.1), it is seen that cementite contributed about 10 mol% of austenite for all samples of Alloys 1 and 3. From mass balance of Mn (Eq. V.2), the cementite contribution is about 15 mol%. For 3-200h, the Mn content of cementite seems to have been underestimated, giving high f^θ.

Alloy	x_{Mn}^α	x_{Mn}^θ	x_C^γ	x_{Mn}^γ	f^θ from Eq. V.1	f^θ from Eq. V.2
1-400h	0.0386	0.240	0.0226	0.0738	0.09	0.18
1-800h	0.0305	0.323	0.0301	0.0773	0.12	0.16
3-200h	0.0305	0.283	0.0169	0.0881	0.07	0.23
3-400h	0.0417	0.332	0.0200	0.0730	0.08	0.11

Table V.11 Fraction cementite portion in austenite (f^θ) calculated from mol-fractions of Mn and C in each phase (x_{Mn}^α, x_{Mn}^θ, x_C^γ, x_{Mn}^γ) which are obtained from Tables IV.6, IV.16, V.3 and V.9.

In conclusion, the austenite formation is found to occur by consuming both cementite and ferrite. Moreover, the Mn and C content in austenite were similar to the equilibrium values. It is evident that there is driving force for both ferrite and cementite to transform into austenite and that the kinetics of two reactions are not sufficiently different for austenite formation to be confined to the consumption of just the cementite. After all, the equilibrium fraction of austenite is greater than that of cementite. In order to keep equilibrium composition of austenite, the contribution of cementite was only 10-15 mol% of austenite.

VI. Mechanical Properties

VI.1. Temperature Control of Salt Bath

For the third anneal of samples for tensile test, salt bath was adopted in order to keep a stable temperature environment around each sample. However, it was found that the amount of austenite formed was far exceeding the results by dilatometer presented in the previous chapter. The possible explanation of the discrepancy is that the heating of the specimen in salt bath was slower than that using dilatometry. Tensile specimens had large dimension and when they were put into the bath, it took several minutes to reach the third annealing temperature resulting in the excess austenite; for dilatometry, it took approximately two minutes. Even though the microstructures were different from that shown in the previous chapter, the tensile test results with microstructure were still interesting and reported here.

VI.2. Tensile Properties

Tensile curves were grouped by composition categories since samples from each alloy composition showed similar deformation behavior. The denotations are the same as used in previous chapters with additional information of sample direction: longitudinal ones are indicated with "L", and transversal ones are with "T" (Fig. II.13). Tensile curves are given in Fig. VI.1

and important tensile properties are given in Table VI.1.

There are three features common to all alloys. First, there was no necking. All alloys were stressed to the highest level and then failed. Second, the curve contained serrated flow indicating instability during loading. Generally, the serration is a characteristic of dynamic strain aging originated from the interaction between moving dislocation and mobile dislocation barriers such as impurities and solute atoms (Reed-Hill and Abbaschian, 1992). However, it is not yet shown that the phenomena is related to the results in this study and needs further study. Last feature is that the maximum stress is achieved very rapid according to strain after reaching yield point.

(a)
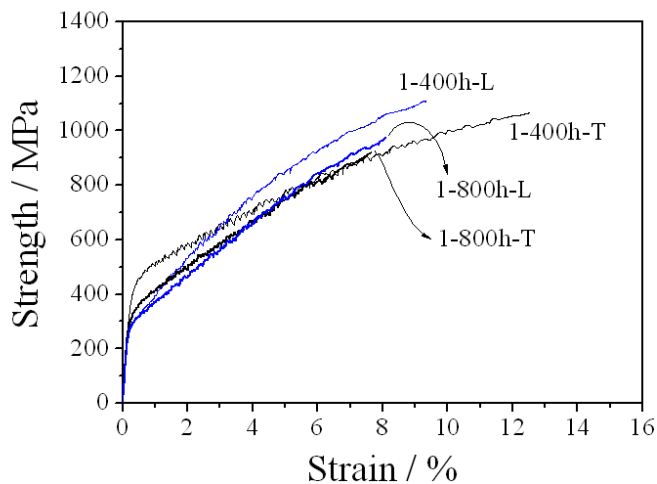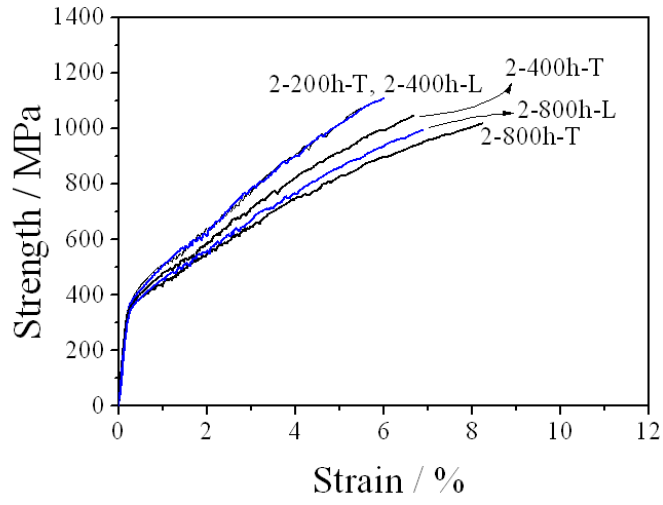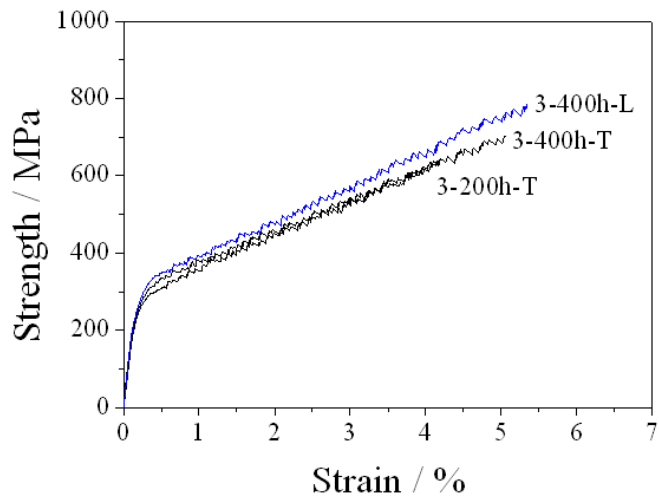
Fig. VI.1 Tensile curves of all alloys (a) Alloy 1 (b) Alloy 2 (c) Alloy3

Alloy	0.2% Proof stress / MPa	UTS / MPa	Elongation / %
1-400h-T	447	1068	12.55
1-400h-L	303	1109	9.36
1-800h-T	342	919	7.65
1-800h-L	307	975	8.10
2-200h-T	425	1100	5.85
2-400h-T	392	1049	6.67
2-400h-L	413	1111	5.99
2-800h-T	377	1019	8.22
2-800h-L	383	997	6.89
3-200h-T	294	637	4.18
3-400h-T	309	706	5.06
3-400h-L	331	783	5.34

Table VI.1 0.2% Proof stress, ultimate tensilte stress (UTS) and elongation of all samples. The elongation corresponds to uniform elongation since no necking occurred.

VI.3. Microstructures of Tensile Samples

VI.3.1. Alloy 1

XRD results are given in Table VI.2 and micrographs are shown in Figs. VI.2 and VI.3. All results include both before and after tensile testing. XRD results shows that there were small difference between 1-400h-T and 1-800h-T and also microstructures were similar through OM. Therefore, only

representative images are shown.

Alloy	Ferrite or martensite / wt%	Austenite / wt%	Cementite / wt%	R_{wp}	R_{exp}	χ^2
1-400h-T (U)	60 ± 1	40 ± 1	0 ± 1	20.1	16.34	1.52
1-400h-T (D)	91 ± 3	8 ± 1	0 ± 1	28.0	18.93	2.19
1-800h-T (U)	55 ± 2	45 ± 1	0 ± 1	20.8	14.82	1.97
1-800h-T (D)	87 ± 1	12 ± 1	0 ± 1	34.7	23.3	2.22

Table VI.2 Quantitative XRD analysis results of Alloy 1 before (U) and after (D) tensile test using the Rietveld refinement method. The martensite structure is similar to that of ferrite, so the phases cannot be distinguished. Only transversal samples are analyzed assuming that longitudinal ones would share the similar behavior.

(c)

(d)
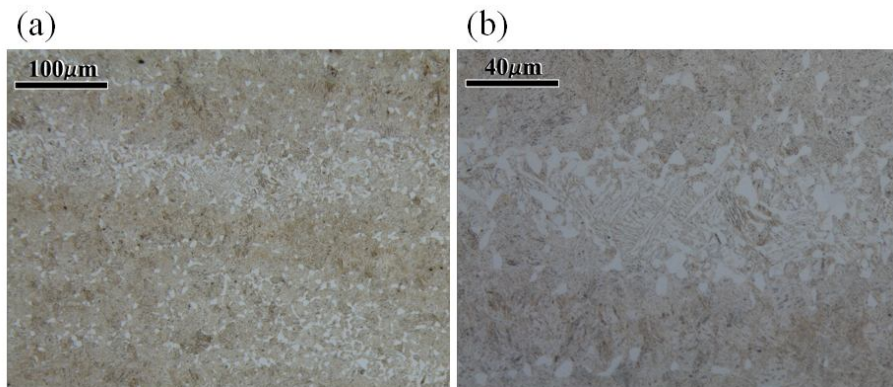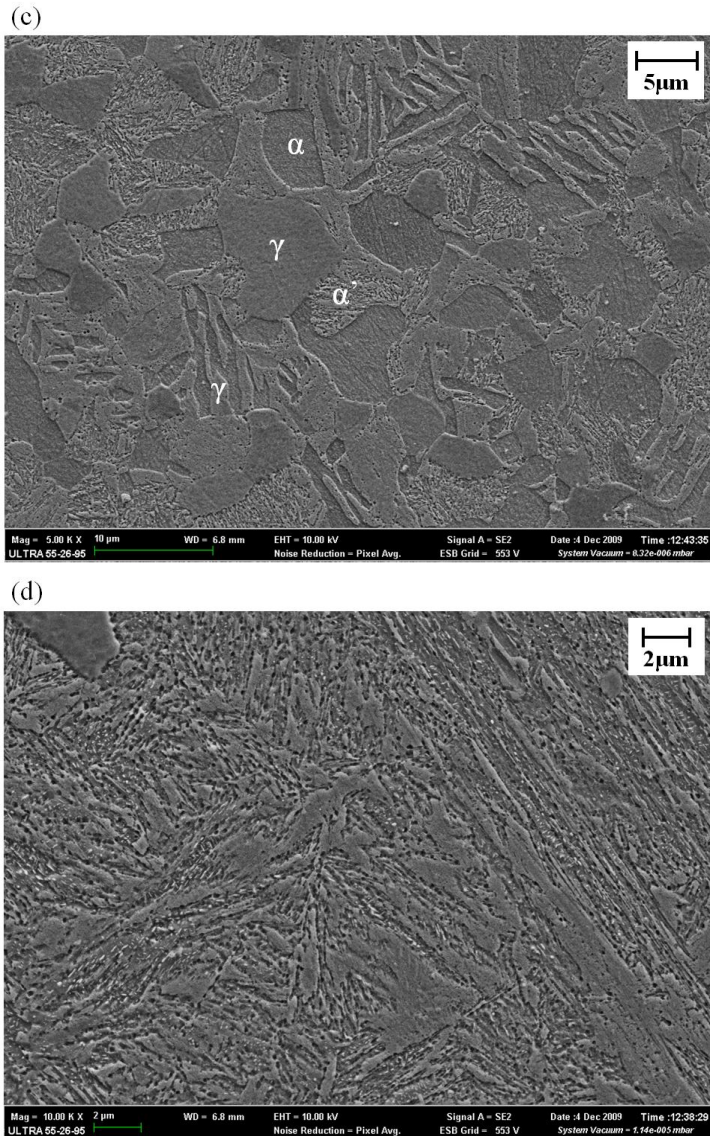
Fig. VI.2 Micrographs of 1-400h-T before tensile test. (a,b) Optical micrographs. (c) FE-SEM image of light-contrast region. Some regions of ferrite (α), austenite (γ), martensite (α') are indicated. (d) FE-SEM image of dark-contrast region.
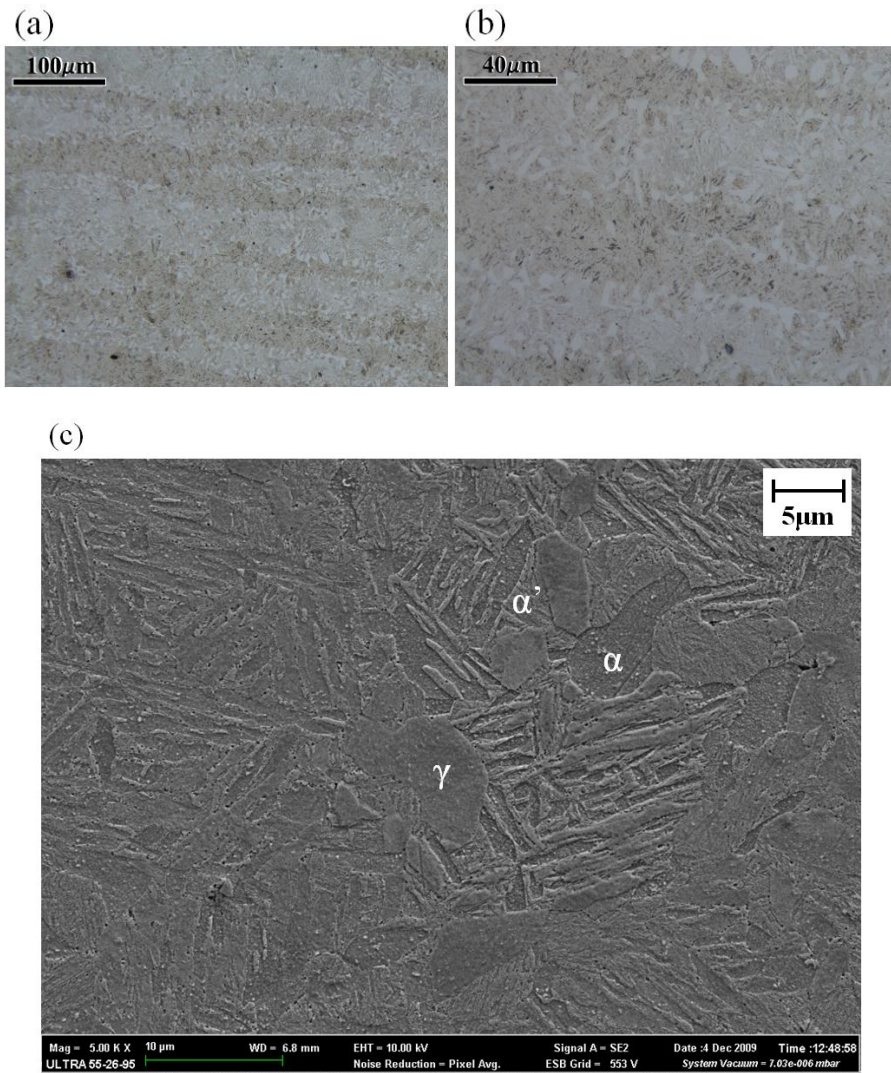
Fig. VI.3 Micrographs of 1-400h-T after tensile test. (a,b) Optical micrographs. (c) FE-SEM image of light-contrast region. Some regions of ferrite (α), austenite (γ), martensite (α') are indicated.

In Fig. VI.2(a) and (b), the samples consisted in three regions. One region was the dark-contrast region which is composed of martensitic structure (Fig. VI.2(d)). Within the martensite, some cementite particles are shown, implying that austenite had been formed in the region containing cementite and then transformed into martensite during cooling. Also, retained austenite seemed to exist since the microhardness was only HV 356 ± 14 for this region. In the middle of the light-contrast region, there were thin ferrite grains with martensite or austenite between them (Fig. VI.2(c)). At the interface between dark and light-contrast region, there were polygonal phases. These regions had polygonal ferrite, austenite and sometimes martensite which was often connected to the martensite in the dark-contrast region (Fig. VI.2(c)).

There was a banded structure after the second anneal and distinct ferrite grain boundaries did not appear in this region (Fig. IV.6(b)). This whole region seems to have been transformed into austenite during heating. For the other region containing ferrite grains, it is expected to consume single ferrite grain one by one thereby leaving polygonal austenite grains as austenite formed. If the austenite is enriched enough with Mn, it would be retained, but if not, it would transform into martensite during cooling.

After deformation, the microstructure seems similar to the undeformed one, consisting both dark and light-contrast region (Fig. VI.3(a,b)). Also, there

were still polygonal austenite, martensite and ferrite but austenite is detected less than before. The dramatic decrease of austenite weight percent detected by XRD implies that large amount of retained austenite in martensite transformed into martensite.

A fractograph is presented in Fig. VI.4. Upper left and middle region experienced ductile fracture while other region consists of transgranular fracture facets. Since the the grain size matches with polygonal ferrite grains, it seems brittle fracture occurred in the light-contrast region.
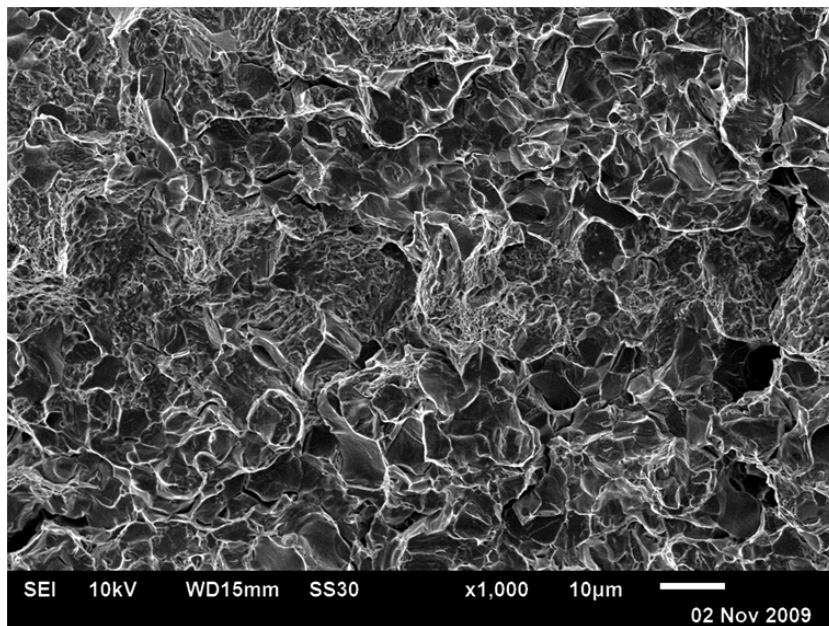
Fig. VI.4 A fractograph of 1-800h-T using SEM.

VI.3.2. Alloy 2

Quantitative XRD results are shown in Table VI.3. Unlike Alloy 1, as the second anneal period gets longer, the austenite weight percent after third anneal decreased and the transformed austenite ratio during deformation increased. For 2-200h, about half of austenite had been transformed, for 2-400h, about two-third, for 2-800h about three-fourth. This difference seems to cause the different tensile test results among the samples of Alloy 2 (Fig. VI.1(b)). It is interesting that the samples with smaller amount of austenite showed higher ductility with lower strength.

Alloy	Ferrite or martensite / wt%	Austenite / wt%	Cementite / wt%	R_{wp}	R_{exp}	χ^2
2-200h-T (U)	53 ± 1	45 ± 1	2 ± 1	22.3	14.27	2.45
2-200h-T (D)	77 ± 3	22 ± 1	1 ± 1	34.6	22.49	2.37
2-400h-T (U)	64 ± 1	34 ± 1	2 ± 1	23.4	15.43	2.30
2-400h-T (D)	86 ± 3	12 ± 1	2 ± 1	33.2	22.49	2.18
2-800h-T (U)	68 ± 1	29 ± 1	3 ± 1	19.2	13.86	1.93
2-800h-T (D)	91 ± 3	7 ± 1	2 ± 1	37.1	20.76	3.20

Table VI.3 Quantitative XRD analysis results of Alloy 2 before (U) and after (D) tensile test using the Rietveld refinement method. Since the martensite structure is similar to the ferrite crystal structure, it cannot be distinguished. Only transversal samples are analyzed assuming that longitudinal ones would share the similar behavior.

The micrographs are shown in Figs. VI.5-VI.6. Although the phase fraction was different, all samples contained the same morphologies so only representative images are shown. In Fig. VI.5, there were banded regions which contain martensite. As in Alloy 1, it contained some of cementite particles within the structure indicating cementite was not fully consumed during the third anneal (Fig. VI.5(c)). Sometimes, there was austenite embedded in the martensite islands. Another region showing light-contrast is composed of spherical austenite particles in ferrite (Fig. VI.5(d)). The austenite particles are usually located on the ferrite grain boundaries.

It is expected that the martensite islands are from previous pearlitic region after the second anneal. All pearlitic regions seemed to have been consumed by austenite. Moreover, it seems that the region of spherical austenite was originated from spherodite region. Since coarse spherical cementite was mainly found at ferrite grain boundaries, the austenite seems to have been nucleated at α/θ interface then it grows consuming several other cementite particles and some part of the ferrite grain. Even though the austenite which had formed at pearlitic region went through martensite transformation, the spherical austenite particles were retained during cooling.

After deformation, the microstructure was similar to the undeformed one. Rarely, mechanical twins can be seen in austenitie islands in martensite (Fig.

VI.6(b)). The spherical austenite did not seem to transform into martensite nor twinned. Thus, with XRD results, the retained austenite in martensite islands is expected to have transformed into martensite.
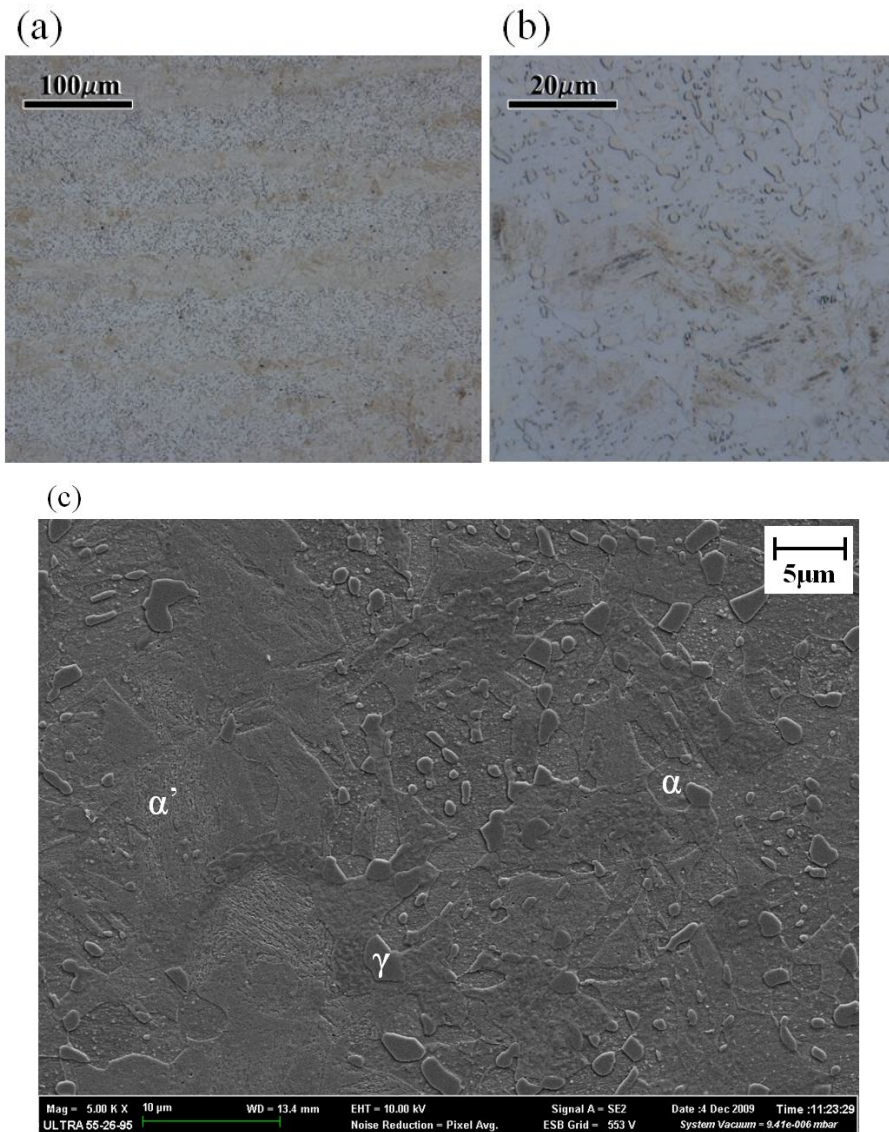
(d)
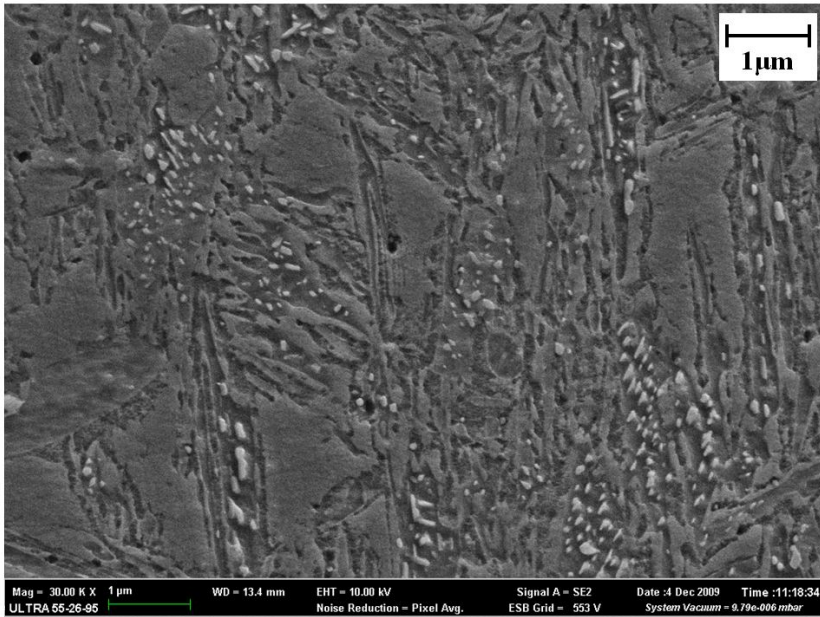
Fig. VI.5 Micrographs of 2-800h-T before tensile test. (a,b) Optical micrographs. (c) FE-SEM image of light-contrast region. Some of ferrite (α), austenite (γ), martensite (α') are indicated. (d) FE-SEM image of banded region.

(a)

(b)

(c)
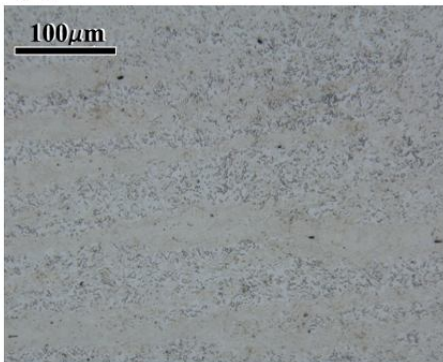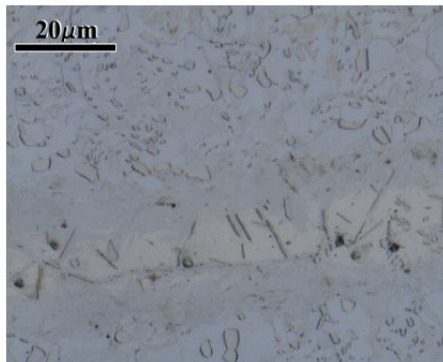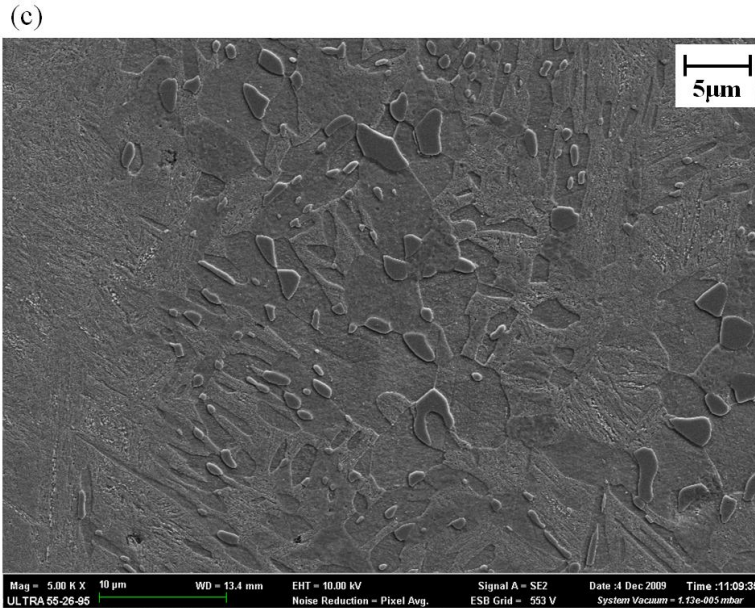
Fig. VI.6 Micrographs of 2-800h-T after tensile test. (a,b) Optical micrographs. (c) FE-SEM image of light-contrast region.

The fractograph is shown in Fig. VI.7. There were both ductile and brittle fracture in all samples of Alloy 2 but the brittle fractured regions were in the majority. Sometimes, transgranular fracture is seen in about 3-5 μm sized grains which are expected to be ferrite grains (Fig. VI.7(a)). The microcracks are seen at the grain boundaries. There were several micrometer-sized particles in this region and it seems to be austenite and the fracture mode was intergranular. Sometimes, the cleavages seen lie in large areas about 30-50 μm in size (Fig. VI.7(b)). However, it is not interpreted completely and needs further study.

(a)

SEI   10kV   WD15mm   SS30   x4,500   5µm   ▬▬▬
                                                      03 Nov 2009

(b)

SEI   10kV   WD14mm   SS30   x1,000   10µm   ▬▬
                                                      03 Nov 2009
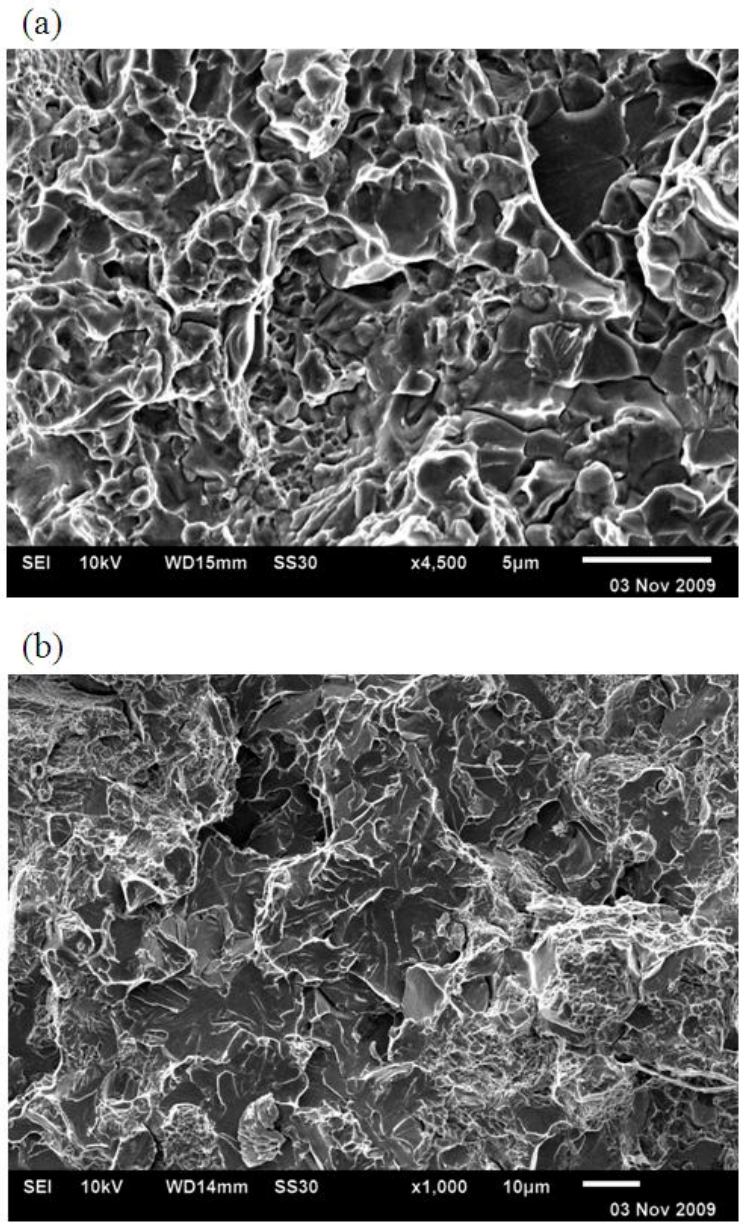
Fig. VI.7 Fractographs of 2-800h-T using SEM.

VI.3.3. Alloy 3

XRD results for samples of Alloy 3 are given in Table VI.4. Comparing with Alloys 1 and 2, a small degree of the stress induced martensitic transformation occurred. For 3-200h-T, there were almost no transformation while about 10 % of austenite has been transformed during deformation for 3-400h-T. This might explain why 3-400h-T showed higher strength and ductility than 3-200h-T, in spite of following the similar deformation curve (Fig. VI.1(c)).

Shown in Fig. VI.8, the samples before and after tensile test share almost the same microstructure. It contains two banded region parallel to RD: austenite and martensite. Both regions contain dark boundaries which are distributed all over the sample. Sometimes, the boundaries are disconnected. When observed with SEM, it was found that the boundaries contained narrow layers of pearlite. Some protruded phase within the pearlite is expected to be austenite. As mentioned in the previous chapter, the microstructure of Alloy 3 after the second anneal is pearlite and ferrite. During the third annealing, almost all regions seem to have transformed into austenite. Since austenite consumes pearlite colonies one by one, it is expected that some pearlite remained at the colony boundaries during the austenitization. Then, during cooling, austenite in the high Mn banded areas retained and that in the low

Mn areas transformed into martensite. Sometimes, spherical austenite regions which were often seen in Alloy 2 were observed which were expected to be originated from spherodite areas (Fig. VI.10).

Alloy	Ferrite or martensite / wt%	Austenite / wt%	Cementite / wt%	R_{wp}	R_{exp}	χ^2
3-200h-T (U)	46 ± 1	54 ± 1	1 ± 1	36.8	18.27	4.06
3-200h-T (D)	48 ± 2	52 ± 2	0 ± 1	24.3	17.78	1.87
3-400h-T (U)	45 ± 2	54 ± 1	0 ± 1	31.9	15.77	4.09
3-400h-T (D)	54 ± 2	46 ± 2	0 ± 1	26.2	18.31	2.04

Table VI.4 Quantitative XRD analysis result of Alloy 3 before (U) and after (D) tensile test using the Rietveld refinement method. Since the martensite structure is similar to the ferrite crystal structure, it cannot be distinguished. Only transversal direction samples are analyzed assuming that longitudinal ones would share the similar behavior.
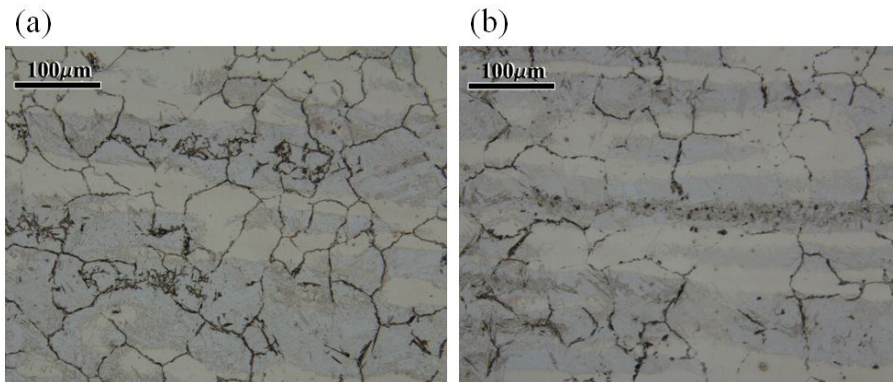
Fig. VI.8 Optical micrographs of 3-200h-T before (a) and after (b) tensile test.
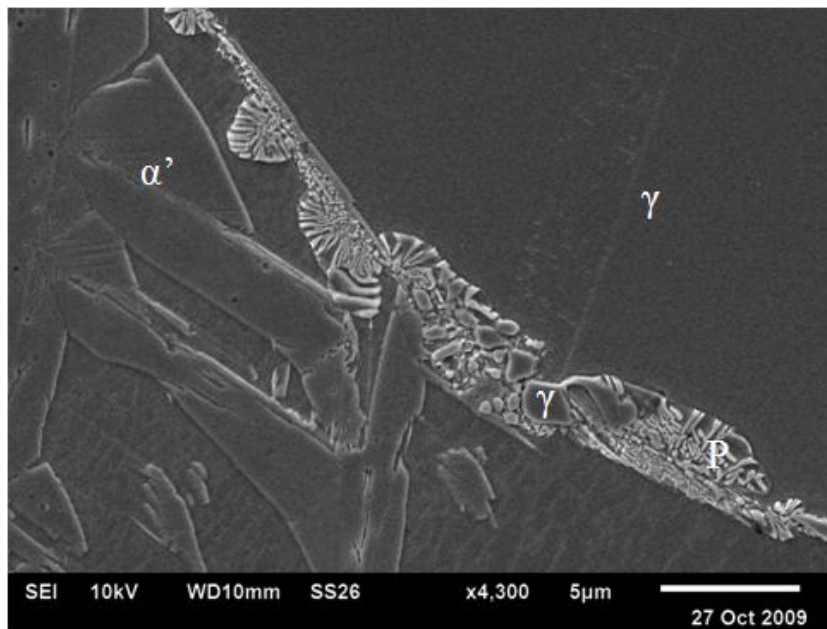
Fig. VI.9 A SEM image of the dark boundary shown in Fig. VI.8. Austenite

(γ), martenisite (α') and pearlitic (P) regions are indicated.
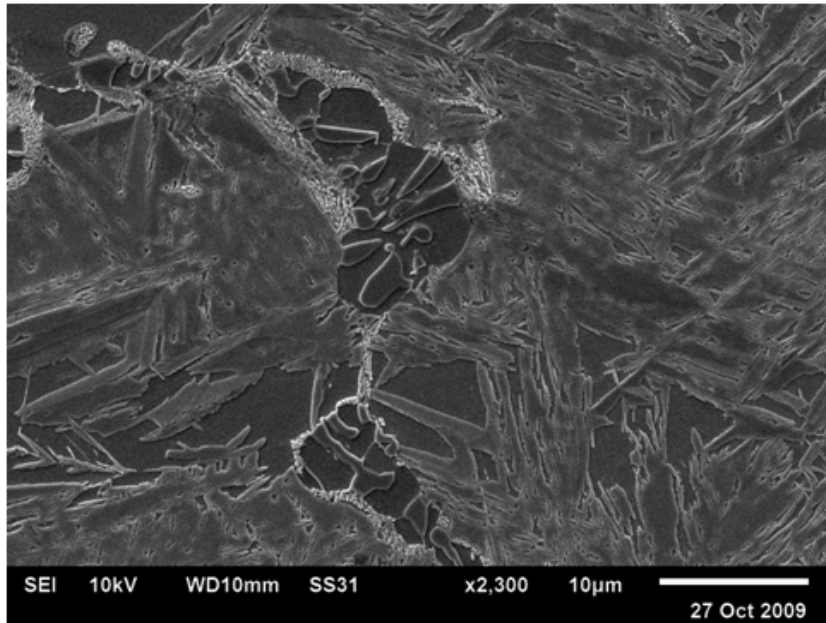
Fig. VI.10 A SEM image of 3-400h before tensile test showing spherical austenitic region.

The fractographs are shown in Fig. VI.11. All samples of Alloy 3 showed similar morphology. The fracture surface seemed to be along the colony boundaries since the protruded parts in Fig. VI.11(a) are the same size to the area enclosed by leftover pearlite in Fig. VI.8. However, the magnified images showed both microvoid coalescence and cleavage facets which are not fully understand yet (Fig. VI.11(b,c,d,e)).

(a)

SEI 10kV WD14mm SS30   x200   100μm
                                        03 Nov 2009

(b)

SEI 10kV WD14mm SS30   x4,000   5μm
                                    03 Nov 2009

(c)

SEI 10kV WD14mm SS30   x2,500   10μm
                                    03 Nov 2009
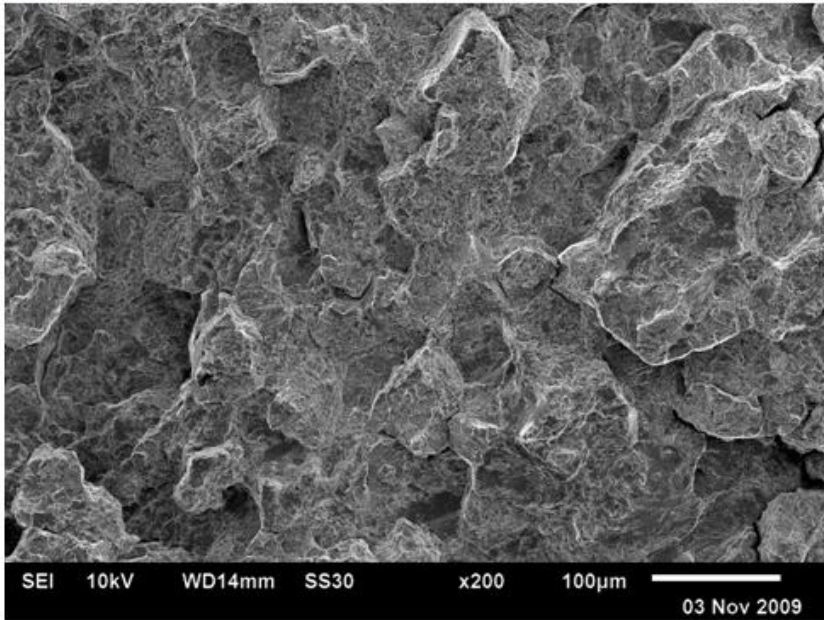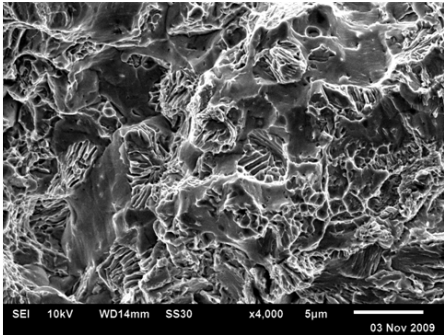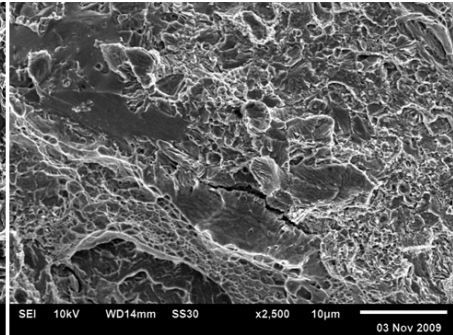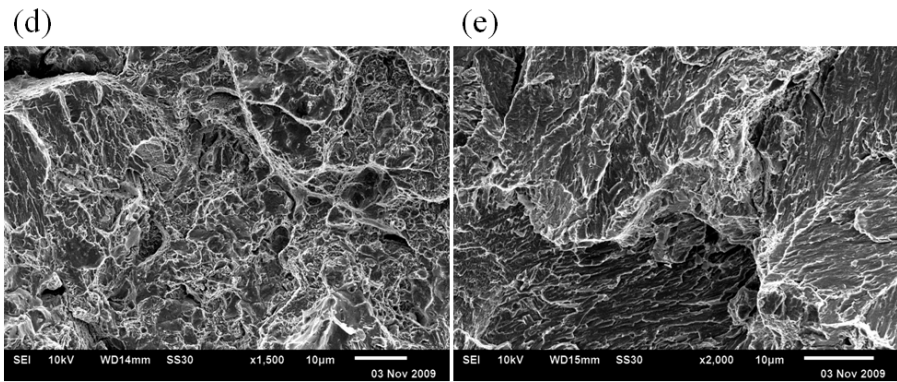
Fig. VI.11 Fractographs of (a,b) 3-200h-T, (c) 3-400h-T, (d) 3-400h-L using SEM.

VII.   Conclusions

The aim of the wok presented in this thesis was to create local regions of austenite which contain sufficient manganese to permit deformation by mechanical twinning at ordinary strain rates. The task was to achieve this whilst maintaining a relatively small overall manganese content in the steel, given that there are significant and costly manufacturing issus associated with making fully austenitic TWIP steels.

The concept was to create mixtures of cementite and ferrite such that after appropriate tempering in the two phase cementite+ferrite field, the cementite would enrich with Mn. This enriched cementite would then be transformed into austenite by heating, and that the austenite should be retained on cooling to ambient temperature. The final microstructure in these circumstances would consist of islands of Mn-rich austenite capable of exhibiting TWIP, in a matrix of ferrite, thus forming the desired TWIP-assis ted steel by analogy with TRIP-assisted steels.

Three alloys, containing different equilibrium fractions of cementite were designed using phase stability calculations. The heat treatments needed to enrich the cementite were also designed using thermodynamic equilibrium calculations combined with a finite difference kinetic model. Finally, the

ultimate task of generating austenite by heating the mixture of enriched austenite and ferrite was designed.

A series of experiments was conducted to test these ideas, including detailed microstructural and microanalytical characterization. The work proved to be exciting with many fundamental results. The most important of these is also a major obstacle to the development of TWIP-assisted steels: it appears that austenite formation during the heating of enriched-cementite and ferrite does not follow intuition that the austenite should first consume the cementite. Instead, the austenite grows almost simultaneously into both the cementite and ferrite, thus inheriting less overall Mn content than might be expected. The ferrite in effect dilutes the austenite that grows.

The manganese in the austenite that forms is heterogeneously distributed, being rich in the region that was previously cementite. On cooling, the latter region is retained as austenite whereas the Mn-poor region of austenite transforms into martensite.

Mechanical property characterization in the form of tensile testing was attempted but there was not enough time to design a proper series of critical experiments. The tensile samples used were too large to conduct rapid heating with the result that the microstructures generated using dilatometry could not

be reproduced in the tensile samples. The measured stress strain curves from these non-representative samples were therefore disappointing.

Future work of this kind could be done instead on a sheet metal simulator where greater control is in principle possible.

References

ALLAIN, S., CHATEAU, J. P. & BOUAZIZ, O. 2004. A physical model of the twinning-induced plasticity effect in a high manganese austenitic steel. *Materials Science and Engineering A,* 387-389**,** 143-147.

ANDREWS, K. W. 1956. *Journal of the Iron and Steel Institute,* 184**,** 414-421.

BHADESHIA, H. K. D. H. 1989. Theoretical analysis of changes in cementite composition during tempering of bainite *Material Science and Technology,* 5**,** 131-137.

BJ RKLUND, S., DONAGHEY, L. F. & HILLERT, M. 1972. The effect of alloying elements on the rate of ostwald ripening of cementite in steel. *Acta Metallurgica,* 20**,** 867-874.

CAHN, J. W. & HAGEL, W. G. 1963. Divergent pearlite in a manganese eutectoid steel. *Acta Metallurgica,* 11**,** 561-574.

DAVIES, R. H., DINSDALE, A. T., GISBY, J. A., ROBINSON, J. A. J. & MARTIN, S. M. 2002. MTDATA - thermodynamic and phase equilibrium software from the national physical laboratory. *Calphad,* 26**,** 229-271.

DING, H., TANG, Z.-Y., LI, W., WANG, M. & SONG, D. 2006. Microstructures and Mechanical Properties of Fe-Mn-(Al, Si) TRIP/TWIP Steels. *Journal of Iron and Steel Research, International,* 13**,** 66-70.

DYSON, D. J. & HOLMS, B. 1970. Effect of alloying additions on the lattice parameter of austenite. *Journal of Iron and Steel Institute,* 208**,** 469-474.

ENGL, B., SENK, D., SCHMITZ, W. & OFFERGELD, A. 2007. *Method for producing a hot strip from a steel which has a high manganese content*. United States patent application 11/796,245. Aug. 30, 2007.

FLEWITT, P. E. J. & WILD, R. K. 1994. Physical methods for materials characterisation. London: Institute of Physics Publishing.

FROMMEYER, G., BRUX, U. & NEUMANN, P. 2003. Supra-ductile and high-strength manganese-TRIP/TWIP steels for high energy absorption purposes. *ISIJ International,* 43**,** 438-446.

GRASSEL, O., KRUGER, L., FROMMEYER, G. & MEYER, L. W. 2000. High strength Fe-Mn-(Al, Si) TRIP/TWIP steels development - properties - application. *International Journal of Plasticity,* 16**,** 1391-1409.

GRUJICIC, M. 1990. Stabilization of precipitated austenite in tempered Fe-Mn-C steels. *Materials Science and Engineering: A,* 127**,** 79-84.

GRUJICIC, M., BUONANNO, M., ALLEN, S. M., OLSON, G. B. & COHEN, M. 1987. *Heterogeneous precipitation of austenite for stabilization. In:* 34th Sagamore Army Materials Research Conference on Innovations of Ultrahigh-Strength Steel Technology, 1987 Lake George, NY. 527-547.

HA, M., KIM, W.-S., MOON, H.-K., LEE, B.-J. & LEE, S. 2008. Analysis and Prevention of Dent Defects Formed during Strip Casting of Twin-Induced Plasticity Steels. *Metallurgical and Materials Transactions A,* 39**,** 1087-1098.

HAIDEMENOPOULOS, G. N. 1996. Austenite stabilization from direct cementite conversion in low-alloy steels. *Steel research,* 67**,** 93-99.

HAMADA, A. S., KARJALAINEN, L. P. & PUUSTINEN, J. 2009. Fatigue behavior of high-Mn TWIP steels. *Materials Science and Engineering: A,* 517**,** 68-77.

HUTCHINSON, C. R., HACKENBERG, R. E. & SHIFLET, G. J. 2004. The growth of partitioned pearlite in Fe-C-Mn steels. *Acta Materialia,* 52**,** 3565-3585.

IMLAU, K. P. & HELLER, T. 2007. New steel solutions for the worldwide car industry. *Steel Research International,* 78**,** 180-184.

JANG, J. H., KIM, I. G. & BHADESHIA, H. K. D. H. 2009. Substitutional solution of silicon in cementite: A first-principles study. *Computational Materials Science,* 44**,** 1319-1326.

JIANG, H., WU, H., TANG, D. & LIU, Q. 2008. Influence of isothermal bainitic processing on the mechanical properties and microstructure characterization of TRIP steel. *Journal of University of Science and Technology Beijing, Mineral, Metallurgy, Material,* 15**,** 574-579.

KIM, T. W. & KIM, Y. G. 1993. Properties of austenitic Fe-25Mn-1Al-0.3C alloy for automotive structural applications. *Materials Science and Engineering: A,* 160**,** 13-15.

KIM, Y., KANG, N., PARK, Y., CHOI, I., KIM, G., KIM, S. & CHO, K. 2008. Effects of the Strain Induced Martensite Transformation on the Delayed Fracture for Al-added TWIP Steel. *Journal of the Korean Institute of Metals and Materials,* 46**,** 780-787.

KLIBER, J., DROZD, K. & MAMUZIC, I. 2009. *Stress-strain behaviour and softening in manganese TWIP steel tested in thermal-mechanical simulator. In:* Metal 2009, 19-21, May 2009 Czech Republic. 117, 1-8.

KRAMER, J. J., POUND, G. M. & MEHL, R. F. 1958. The free energy of formation and the interfacial enthalpy in pearlite. *Acta Metallurgica,* 6**,** 763-771.

LIU, Z. Y., LIN, Z. S., WANG, S. H., QIU, Y. Q., LIU, X. H. & WANG, G. D. 2007. Microstructure characterization of austenitic Fe-25Mn-22Cr-2Si-0.7N alloy processed by twin roll strip casting. *Materials Characterization,* 58**,** 974-979.

MIYAMOTO, G., OH, J. C., HONO, K., FURUHARA, T. & MAKI, T. 2007. Effect of partitioning of Mn and Si on the growth kinetics of cementite in tempered Fe-0.6 mass% C martensite. *Acta Materialia,* 55**,** 5027-5038.

MOVAHED, P., KOLAHGAR, S., MARASHI, S. P. H., POURANVARI, M. & PARVIN, N. 2009. The effect of intercritical heat treatment temperature on the tensile properties and work hardening behavior of ferrite-martensite dual phase steel sheets. *Materials Science and Engineering: A,* 518**,** 1-6.

OLIVER, S., JONES, T. B. & FOURLARIS, G. 2007. Dual phase versus

TRIP strip steels: Microstructural changes as a consequence of quasi-static and dynamic tensile testing. *Materials Characterization,* 58**,** 390-400.

ONINK, M., BRAKMAN, C. M., TICHELAAR, F. D., MITTEMEIJER, E. J., VAN DER ZWAAG, S., ROOT, J. H. & KONYER, N. B. 1993. The lattice parameters of austenite and ferrite in Fe---C alloys as functions of carbon concentration and temperature. *Scripta Metallurgica et Materialia,* 29**,** 1011-1016.

PARK, S. H., CHUNG, I. S. & KIM, T. W. 1998. Characterization of the High-Temperature Oxidation Behavior in Fe-25Mn-1.5Al-0.5C Alloy. *Oxidation of Metals,* 49**,** 349-371.

RAGHAVAN, K. S., SASTRI, A. S. & MARCINKOWSKI, M. J. 1969. Nature of the Work-Hardening Behavior in Hadfield's Manganese Steel. *Transactions of the Metallurgical Society of AIME,* 245**,** 1569-1575.

RAO, B. V. N. 1985. *Ferrite-austenite dual phase steel*. United States patent application 595,727.

REED-HILL, R. E. & ABBASCHIAN, R. 1992. Dynamic strain aging. *Physical metallurgy principles*. 3 ed. Boston: PWS publishing company.

RODRIGUEZ-CARVAJAL, J. 2001. An introduction to the program FullProf 2000. Laboratoire Leon Brillouin.

SATO, K., ICHINOSE, M., HIROTSU, Y. & INOUE, Y. 1989. Effects of Deformation Induced Phase Transformation and Twinning on the Mechanical Properties of Austenitic Fe-Mn-Al Alloys. *ISIJ International,* 29**,** 868-877.

SPERLE, J. O. 1985. Fatigue strength of high strength dual-phase steel sheet. *International Journal of Fatigue,* 7**,** 79-86.

SPITZER, K. H., RUPPEL, F., VISCOROVA, R., SCHOLZ, R., KROOS, J. & FLAXA, V. 2003. Direct Strip Casting (DSC) - An option for the production of new steel grades. *Steel Research International,* 74**,** 724-

731.

SRIVASTAVA, A. K., JHA, G., GOPE, N. & SINGH, S. B. 2006. Effect of heat treatment on microstructure and mechanical properties of cold rolled C-Mn-Si TRIP-aided steel. *Materials Characterization,* 57**,** 127-135.

TOMOTA, Y., STRUM, M. & MORRIS, J. 1986. Microstructural dependence of Fe-high Mn tensile behavior. *Metallurgical and Materials Transactions A,* 17**,** 537-547.

WADA, T., WADA, H., ELLIOTT, J. & CHIPMAN, J. 1972. Thermodynamics of the fcc Fe-Mn-C and Fe-Si-C alloys. *Metallurgical and Materials Transactions B,* 3**,** 1657-1662.

WEAST, R. C. (ed.) 1976. *CRC handbook,* Boca Raton: CRC Press.

WORLDAUTOSTEEL. *Steel mechanical properties* [Online]. Available: http://www.worldautosteel.org/SteelBasics/Properties/Mechanical.asp x [Accessed 17 August 2009].

XU, H., YANG, W. & SUN, Z. 2008. Mechanical properties of fine-grained dual phase low-carbon steels based on dynamic transformation. *Journal of University of Science and Technology Beijing, Mineral, Metallurgy, Material,* 15**,** 556-560.

YANG, H.-S. & BHADESHIA, H. K. D. H. 2007. Uncertainties in dilatometric determination of martensite start temperature. *Materials Science and Technology,* 23**,** 556-560.